UNIVERSITY OF CALIFORNIA,
IRVINE

Wrinkled Micro-Nanostructured Thin Films for Flexible Wearable Electronics and Continuous Health Monitoring Applications

DISSERTATION

submitted in partial satisfaction of the requirements for the degree of

DOCTOR OF PHILOSOPHY

in Materials Science and Engineering

by

Joshua Kim

Dissertation Committee:
Professor Michelle Khine, Chair
Professor Gregory Washington
Professor James Earthman

2018

DEDICATION

To

My parents Kim Jae Jung and Lee Meekyung

&

My sibling Samuel Kim

TABLE OF CONTENTS

LIST OF FIGURES ..... **v**

LIST OF TABLES ..... **viii**

ACKNOWLEDGEMENTS ..... **ix**

CHAPTER 1: INTRODUCTION **1**

1.1 Overview of Dissertation 2

CHAPTER 2: FLEXIBLE, STRETCHABLE ELECTRONICS AND CHALLENGES **3**

2.1 Mechanical Behavior of Functional Materials 3
2.1.1 Thin Film Materials 3
2.1.2 Nanoparticle Thin Films and Composites 4
2.1.3 Liquid Metals 5
2.1.4 Conclusion 5

2.2 Strategies to Improve Mechanical Stretchability in Functional Materials 6
2.2.1 Importance of Substrate 6
2.2.2 Interfacial Strength to Substrate 6
2.2.3 Geometrical Designs 7
2.2.4 Nano/Microstructures for Strain Relief 8
2.2.5 Shrink Induced Wrinkling with Shape Memory Polymers 9
2.3 Compatibility with the Human Body 9

CHAPTER 3: MECHANICAL SENSOR MODALITIES **12**

3.1 Piezoresistivity 12
3.1.1 Strain sensor 13
3.1.2 Microcracking Strategy 14
3.1.3 Piezoresistive Pressure Sensor 15
3.1.4 Conclusion 16

3.2 Piezocapacitance 16
3.2.1 Dielectric 17
3.2.2 Strain Sensing 17
3.2.3 Pressuring Sensing 18
3.2.4 Conclusion 19

CHAPTER 4: HIGHLY STRETCHABLE WRINKLED GOLD THIN FILM WIRES **20**

4.1 Introduction 20

4.2 Experimental Methods 21

4.3 Results and Discussion 23

4.4 Conclusion 29

CHAPTER 5: HIGHLY STRETCHABLE CARBON NANOTUBE THIN FILMS AND MOTION DETECTION **30**

5.1 Introduction 30

5.2 Experimental Methods 30

5.3 Results and Discussion 33

5.4 Conclusion 38

CHAPTER 6: WRINKLED CARBON NANOTUBE PIEZORESISTIVE PRESSURE SENSORS 39
6.1 Introduction 39
6.2 Experimental Methods 39
6.3 Wrinkled CNT Pressure Sensor Characterization 41
6.4 Different Wrinkle Combinations 44
6.5 Voice and Pulsatile Blood Flow Detection 45
6.6 Conclusion 46
CHAPTER 7: FLEXIBLE PIEZOCAPACITIVE PRESSURE SENSORS FOR NONINVASIVE BLOOD PRESSURE MONITORING 47
7.1 Introduction 47
7.3 Results and Discussion 51
7.4 Radial Pulse Detection and Blood Pressure Estimation 57
7.4.1 Radial Pulse Measurement Methods 57
7.4.2 Blood Pressure Analytical Methods 59
7.4.3 Subject Data Example 60
7.5 Subject Data, Beat-to-Beat Blood Pressure Analysis 63
7.5.1 Subject 1 63
7.5.8 Bland Altman Analysis of All Subjects Combined 71
7.4 Conclusion 73
CHAPTER 8: FUTURE DIRECTIONS 74
8.1 Dielectric Doping 74
8.2 Mapping with Redundant Sensors 74
8.3 Ambulatory NIBP monitoring applications 76
8.4 Blood Pressure Calibration 79
8.7 Other Biometric Signals 79
8.6 Sensor Materials and Form Factor 83
8.7 Final Remarks 84
SUPPLEMENTAL MATERIALS 85
SI.1 Subject 2 85
SI.2 Subject 3 92
SI.3 Subject 4 99
SI.4 Subject 5 105
SI.5 Subject 6 112
SI.6 Subject 7 119
SI.7 Bland-Altman plots of averaged subject tests 126
REFERENCES 127

LIST OF FIGURES

Figure 1. Different methods of MPTMS on Au thin films on elastomeric substrates show differing amounts of interfacial strength.[47] Reprinted with permission. 7
Figure 2. Gutruf et al. demonstrated differing 'serpentine' geometries produce strain relief in Au thin films.[66] Reprinted with Permission. 8
Figure 3. Behavior of silicones with different elastic moduli on the human body.[73] Reprinted with permission. 11
Figure 4. Illustration of conductive electrodes contacting each other. As pressure is applied, the contact surface area between the electrodes increase which reduces the electrical resistance between the electrodes. 15
Figure 5. a) Shadow mask is first mounted onto the substrate. b) Electron beam deposition of Au through the shadow mask. c) PS substrate is subsequently heated passed the glass transition temperature. d) MPTMS chemical linker treatment. e) Silicone elastomer spin coated and cured on substrate. f) Lift-off from thermoplastic using organic solvent bath. g) Final wrinkled Au thin film on Ecoflex. 22
Figure 6. SEM images of Au thin film at various stages of the fabrication process. (a) Au film on PS substrate. (b) After thermally induced shrinking Au film on PS substrate. (c) Transferred wrinkled Au thin film. d) van der Pauw sheet resistance measurements. Left column scale bar and inset are 30μm and 5μm. 23
Figure 7. a) Wrinkled Au thin film wire strained to failure. b) Gauge factor of five sensors measured at 70% strain. c) 100 cycles of 50% strain. d) SEM image of wrinkled Au thin film strained to 70% and e) 150% strain. Left hand column scale bar the insets are 500μm and 50μm respectively. 24
Figure 8. a) Normalized LED green light intensity plot of wrinkled Au thin film vs flat Au thin films strained to failure. b) Wrinkled Au thin film at 0% strain and at c) 80% strain. Circles denote green LED and wrinkled Au stretchable wire. 25
Figure 9. Flat Au thin films strained to failure. Note that flat Au thin films were only able to withstand strains of up to 30%. 27
Figure 10. Transferred flat Au thin film onto Ecoflex. Scale bar on left is 30μm, and the inset on the right is 5 μm. Note that there is some slight wrinkling present even in the Au thin film. This is due to spontaneous thermal expansion and relaxation of metallic thin films on soft elastomeric substrates.[101] 27
Figure 11. Fabrication process flow for wrinkled CNT thin film strain sensor. a) Shadow mask is placed on a PS substrate. b) Aqueous CNT solution is spray coated on heated substrate. c) Substrate is heated passed glass transition temperature to induce biaxial shrinking. d) Silicone elastomer is cured on top of substrate. e) Transfer is completed using an organic solvent transfer process. f) Final wrinkled CNT thin film. 30
Figure 12. a) SEM of deposited CNT thin film on PS substrate. b) Wrinkled CNT thin film on PS. c) Higher SEM magnification image of wrinkled CNT thin film on PS. 33
Figure 13. Electromechanical characterization of flat and wrinkled CNT thin film on Ecoflex. Top plot shows a flat CNT thin film only being able to withstand tensile strain of up to 12%. Bottom plot shows wrinkled CNT thin film is able to withstand strains of up to 700%. 34
Figure 14. SEM images of wrinkled CNT thin film strained at 400% and 600%. 35
Figure 15. Cyclic strain of wrinkled CNT thin film. 36
Figure 16. a) Wrinkled CNT thin film sensor laminated on the elbow, b) knee, and c) finger joint. 37
Figure 17. Fabrication process flow of wrinkled CNT piezoresistive pressure sensor. a) Frisket film mask first is placed on PS substrate. b) CNT dispersed solution is deposited onto a heated PS substrate. c) Thermally induced shrinking process. d) Silicone elastomer cured on the wrinkled CNT thin film. e) Organic solvent transfer bath. f) Final wrinkled CNT thin film on silicone elastomer. 39

Figure 18. a) CNT thin film deposited on PS substrate. b) Biaxially thermally induced shrunk wrinkled CNT thin film and c) transferred onto Ecoflex substrate. d) Uniaxially thermally induced shrunk wrinkled CNT thin film and e) transferred onto Ecoflex. Scale bars are 50 μm. 40
Figure 19. a) Pressure sensitivity for 1D-2D wrinkled CNT thin films compared to flat CNT thin films. b) Pressure sensitivity of six different sensors. 41
Figure 20. a) 500 cycles of 0.5 kPa load b) Inset of 5 cycles during cyclic loading. c) Relative resistance change at a given number of cycles *n*. 42
Figure 21. a) 1D wrinkles and b) 2D wrinkled CNT thin films after 500 cycles of 0.5 kPa. 43
Figure 22. a) Electromechanical response of different wrinkled morphology combinations. b) FEA of normalized contact of different wrinkled morphology combinations. c) FEA illustrating increasing contact per displacement for different wrinkle morphologies. 44
Figure 23. a) Radial pulse detection over several cardiac cycles. b) Inset of one pulse waveform illustrating the detection of the systolic peak 'SYS 1', second systolic peak 'SYS 2', and diastolic 'D'... 45
Figure 24. Voice detection when sensor is attached to the throat. Unique waveforms were detected for different phrases as the throat was moving while speaking different phrases. 45
Figure 25. Fabrication process flow of capacitive pressure sensors. During the patterning step, laser is etched into the PS to create microridge structures. a) Au is sputtered through a shadow mask. b) Sample is heated passed glass transition temperature to induce shrinking of shape memory polymer. c) Silicone elastomer is then bonded to the wrinkled Au thin film and then d) transferred using an organic solvent bath. d) Dielectric elastomer is plasma bonded between two electrode layers. f) Interconnections are added to complete sensor fabrication. 49
Figure 26. Illustration of cross section of capacitive pressure sensor. a) Schematic of pressure sensor prior to load and b) after load. 49
Figure 27. a) PS etch prior to shrinking. b) PS etched profile after shrinking. c) PDMS molded microridge. Height profile was measured with a laser confocal microscope. 53
Figure 28. a) Pressure sensitivity curve of five capacitive pressure sensors. b) Inset of pressure sensitivity curves from 0-10 kPa with respective pressure sensitivity measurements. 54
Figure 29.a) Pressure sensitivity for sensor with no microridges. b) Pressure sensitivity from 0-10 kPa. Note the pressure sensitivity is not linear within this region. 55
Figure 30. a) Electromechanical response of the capacitive pressure upon applying pressure using force gauge. b) Inset of the electromechanical response. Insufficient sampling rate and ability to load makes it difficult to accurately measure response time. 56
Figure 31. a) Quick tapping response of the capacitive pressure sensor. b) Inset of the quick tap response. 56
Figure 32. a) 1000 Cycles of ~24 kPa. b) Last 135 cycles of cyclic load. 57
Figure 33. Blood pressure measurement setup. Handedness denoted by L (left) and R (right). Biostamp is placed on the left dorsal of the hand. CAP is placed on the left radial artery. CS is placed on the right finger index. 58
Figure 34. Subject 1 CAP and CS. a) Whole test measurement. b) Example of pulse wave form. 60
Figure 35. Subject 1. a) Example of 70 beats during deep breathing and b) the next 70 beats during normal breathing. 61
Figure 36. Bland-Altman plot of all subject data combined. 5 consecutive cardiac cycles were averaged prior to creating the model. 71
Figure 37. a) Radial pulse detection using two capacitive sensors simultaneously. Measurements taken on Texas Instruments FDC 2214 EVM. b) Manual pressing of different sensors separated by ~ 2mm apart. 75
Figure 38. Radial tonometry measurement with capacitive pressure sensor for approximately 28 minutes. 76
Figure 39. Accelerometer data and radial pulse data superimposed. 77
Figure 40. Sudden changes in blood pressure are measured. Systolic and diastolic pressure show strong agreement between the CAP and CS devices. *Note: some peaks were not properly detected, however the differences are negligible. 78
Figure 41. Respiration data shown in red and radial pulse data shown in black. Inhalation corresponds to increased electrical resistance and exhalation corresponds to decreased electrical resistance. 80

Figure 42. a) Radial pulse measurement and b) ECG measurement taken simultaneously. Diastolic peaks of the radial pulse and the 'S' wave of the ECG was chosen (R-wave was minimal therefore S-wave was used as a proxy). 81
Figure 43. PTT calculated for the corresponding radial pulse measurement. 81
Figure 44. PTT plotted against the systolic peak from the radial pulse measurement. 82
Figure 45. HRV measurements from radial pulse using capacitive pressure sensor (CAP) and ECG. 83

LIST OF TABLES

Table 1. Linear regression analysis for SBP. 70
Table 2. Linear regression analysis for DBP. 70
Table 3. Linear regression analysis for MAP. 70
Table 4. CAP and CS comparison of SBP, DBP, and MAP. 72
Table 5. Combined CAP and CS comparison. 72

ACKNOWLEDGEMENTS

I would like to express my sincere appreciation to…

My family for the limitless love and support,

My friends for being the perfect balance in life,

My colleagues for the endless inspiring conversations,

My mentor, Michelle Khine, for instilling the most important trait as an engineer – creativity.

CURRICULUM VITAE

Joshua Kim

EDUCATION

2013
Bachelors of Science in Chemistry
University of Illinois, at Urbana – Champaign

2015
Masters of Science in Materials Science and Engineering
University of California, Irvine

2018
Doctorate of Philosophy in Materials Science and Engineering
University of California, Irvine

PUBLICATIONS

1) **J. Kim**, S. J. Park, T. Nguyen, M. Chu, J. D. Pegan, M. Khine, *Appl. Phys. Lett.* 2016, *108*.
2) S. Park, **J. Kim**, M. Chu, M. Khine, *Adv. Mater. Technol.* 2018, *3.*
3) S. Park, **J. Kim**, M. Chu, M. Khine, *Adv. Mater. Technol.* 2016, *1*.
4) J. D. Pegan, J. Zhang, M. Chu, T. Nguyen, S.-J. Park, A. Paul, **J. Kim**, M. Bachman, M. Khine, Nanoscale 2016, 8, 17295.
5) Wearable Sensors: Modalities, Challenges, and Prospects. J. Heikenfeld, A. Jajack, J.Rogers, P. Gutruf, L. Tian, T. Pan, R. Li, M. Khine, **J. Kim,** J. Wang, J. Kim. 2018

PRESENTATIONS

WEAR Conference, San Francisco, CA *June 2017*
The Wearable Biomedical Systems and Sensors

3rd SoCal Micro and NanoSymposium, Irvine, CA *September 2016*
Stretchable, Flexible Pressure Sensors for Health Monitoring

CADMIM IAB Meeting, Irvine, CA *February 2016*
Highly Stretchable, Skin-Like Sensors and Electronic Components

CADMIM IAB Meeting, Irvine, CA *March 2015*
Densification of Carbon Nanotubes via Heat Induced Shrinking

IEEE EMBS MNM in Medicine Conference, Oahu, Hawaii *December 2014*
Densification of Carbon Nanotubes via Uniaxial Shrinking

ABSTRACT OF THE DISSERTATION

Wrinkled Micro-Nanostructured Thin Films for Flexible Wearable Electronics and Continuous Health Monitoring Applications

By Joshua Kim

Doctor of Philosophy in Materials Science and Engineering

University of California, Irvine, 2018

Professor Michelle Khine, Chair

The rapid growth of wearable electronics has generated an influx of research in developing highly flexible, stretchable materials and sensors that can conform to the human body. Developing flexible soft sensors that are capable of withstanding large amounts of mechanical stress can enable novel continuous health monitoring devices. However, existing functional materials are rigid and brittle which are not able to flex and stretch with the human body. Therefore, there is a need to engineer materials that are capable of withstanding mechanical stress to develop conformable wearable electronics for continuous health monitoring applications.

The work presented here introduces a thermally induced shrinking fabrication platform using pre-stressed thermoplastics to create highly wrinkled structured thin films for stretchable electronic sensing applications. Specifically, mechanically flexible and stretchable wrinkled gold (Au) and carbon nanotube (CNT) thin films were fabricated for stretchable conductive wire, strain, and pressure applications. Electrical-mechanical characterization studies have shown that these wrinkled functional thin film materials, in comparison to its flat counterpart, were able to withstand large amounts of tensile stress and mechanical pressure before electrical failure. When supported by elastomeric substrates, these wrinkled thin film materials may be used as stretchable wires and sensors for wearable applications on the human body. Finally, I will report on potential wearable applications demonstrating continuous health monitoring applications including human motion detection and blood pressure estimation.

CHAPTER 1: INTRODUCTION

The Internet of Things (IoT) has become an important topic in the last few decades that which describes the interconnection of people and physical devices ("things") with the internet.[1,2] IoT allows for the connection of people to devices which may enable unique applications including continuous health monitoring which may be impactful for general public health. Therefore, there is a need to develop sensors that are capable of tracking human biometrics to provide relevant information regarding one's health.

Currently, wearable electronics such as the Apple Watch, Fitbit, and Microsoft Band enable users to track their health over a period of time. However, the information these devices can currently provide are limited by the rigid sensors used in these devices. To address these issues, there have been efforts in using materials that are conformal, flexible, and stretchable which can enable detection of physiological signals such as pulsatile blood flow from the radial artery.

Recently, there has been renewed interest in detecting pulsatile blood flow in accessible arteries on the human body using flexible electronics.[3–10] Noninvasive radial arterial applanation tonometry has been used to characterize an individual's pulsatile blood flow waveform where one can extract clinically relevant information that may provide insights regarding a patient's cardiovascular health including arterial blood pressure.[11–15] Currently, radial arterial applanation tonometry is accomplished by placing a handheld pressure sensor over the radial artery while having the patient hold very still. Although a powerful tool, 24-7 continuous radial arterial tonometry monitoring has yet to be achieved. One possible solution to enable continuous radial artery tonometry is to develop flexible and stretchable sensors that are able to conform to the human body.

Soft sensors that are able to conform to the human body can extract large amounts of information that are found on the surface of the skin, unlike rigid sensors which cannot flex and stretch with the skin. The challenge remains in developing these sensors with functional materials that are able to withstand large amounts of mechanical stress without failure. In the next section, strategies to develop soft conformal sensors for wearable applications will be discussed.

1.1 Overview of Dissertation

Dissertation presented here will first explore in chapter 2 the mechanics of a broad category of different materials (metallic/ceramic thin films, nanoparticle thin films, and liquid metals) and its applications in stretchable electronics. The latter half of chapter 2 will discuss engineering strategies to manipulate the intrinsic mechanical limitations of common functional materials used in stretchable electronics and briefly explore mechanical compatibility on the human skin. One of these engineering strategies will include a thermally induced shrinking fabrication process using shape memory polymers to form highly wrinkled structures in functional materials. After outlining materials and methods to fabricate stretchable functional materials, common modalities of mechanical strain and pressure sensors will be introduced in chapter 3. Chapters 4-7 will then report findings, incorporating many of the concepts introduced in the earlier chapters, on wrinkled functional materials and its applications for wearable health monitoring applications. Chapters 4-7 presents a proof of concept of many continuous health monitoring applications including human motion and more importantly blood pressure estimation via radial pulse detection. Chapter 8 will speculate future studies including device and material optimization, signal processing, as well as clinical applications.

CHAPTER 2: FLEXIBLE, STRETCHABLE ELECTRONICS AND CHALLENGES

When designing stretchable/flexible wearable electronics, it is important to understand the mechanics of how micro/nanometer scale thin film materials deform. By understanding the mechanical properties of thin film materials, it is then possible to manipulate those properties and fabricate flexible devices allowing for biometric monitoring such as human motion and pulsatile blood flow detection. First, the mechanical properties of common materials used in flexible electronics will be discussed and then strategies on improving the flexibility and stretchability of brittle thin film materials will be reviewed.

2.1 Mechanical Behavior of Functional Materials

2.1.1 Thin Film Materials

Generally, thin film materials refer to materials that are significantly thinner than the substrate the thin film is bonded to and can range from the nanometer to the micrometer scale. Common thin film materials include, but not limited to, thin films such as gold (Au) and platinum (Pt), as well as ceramics including semiconducting silicon (Si). When dimensions of thin materials approach dimensions of the microstructural grain sizes, the mechanical behavior of thin materials may change in comparison to bulk materials. The dimension reduction of thin films may amplify the effects of internal and external stresses such as dislocations, lattice grain mismatch, and thermal expansion. These stresses are highly dependent on the substrate chemistry, thin film deposition and growth mechanisms (i.e. nucleation, diffusion, and grain growth).[16–21]

In addition, it is well known that thin film materials are inherently more flexible compared to its bulk counterpart as described by the following simplified pure bending equation:

$$\varepsilon = \frac{d}{2r} \quad (1)$$

where ε is the amount of strain in the material, *d* is the thickness of the material, and *r* is the radius of curvature. It is clear from Equation 1 that thinner materials will experience less strain with the same amount of bending, *r*. Gleskova et al. have shown that it is possible to bend amorphous silicon thin film transistors (TFTs) on 25 μm Kapton film of up to 2mm (ε = 0.5%) without any significant degradation in electrical performance.[22] Park et al. have also shown a comprehensive study of the bending mechanics of thin film materials on plastic substrates.[23] They have shown that thicker films experience various fracture modes at smaller strains such as delamination and slipping. In addition, they have also shown that by adding an encapsulation layer, the thin film material is moved into a neutral mechanical plane thereby allowing the thin film to withstand substantially larger bending strains. In this study, silicon ribbons (290 nm) were fabricated on epoxy:PET substrates (1 μm : 175 μm). At nominal strains of ~2.54%, the silicon ribbons experienced a slipping failure mode. However, by adding an encapsulation layer of epoxy:PET (1 μm : 175 μm) over the silicon ribbon, the diode was able to operate at even higher nominal strains of ~2.71%. Any additional nominal strain led to failure due to slipping induced fracture.

2.1.2 Nanoparticle Thin Films and Composites

High aspect ratio nanomaterials such as carbon nanotubes (CNTs), gold (Au) nanowires, silver (Ag) nanowires, Si nanowires have received considerable attention for developing stretchable wearable electronics.[24–31] Unlike metallic/ceramic thin films, high aspect ratio nanomaterials can form percolating network thin films which are able to withstand relatively large amounts of strain.[27] Zhang et al. were able to form highly aligned CNT ribbons by drawing from CNT forests. In this study, they have demonstrated that after a tensile strain conditioning phase of the CNT ribbons, the conductivity did not change up to 100% strain.[26] Park et al. have shown that it is also possible to incorporate wrinkled buckled structures in CNT thin films which further

improve the elasticity of the thin film allowing strains of up to 700%.[32] Failure modes are similar to that of metallic/ceramic thin films where at high mechanical strains, necking and cracking occurs in localized regions possibly due to localized weak adhesion sites between thin film and substrate.

Nanoparticles can also be embedded in polymers to create stretchable conductive composite materials. Unlike thin films, nanoparticles create a percolating network within the polymer matrix.[29–31,33–36] High aspect ratio nanoparticles are commonly used as fillers to create conductive elastomeric composites for stretchable applications. Research has shown that the percolation threshold highly depends on the high aspect ratio properties and concentration of the nanoparticles in order for a composite material to have conductive properties.[37–40] For example, Catenacci et al. incorporated Cu-Ag core-shell nanowire materials in silicone elastomer substrates demonstrating stretchability of up to 300% with conductivities of up to 1000 S cm^{-1}.[33]

2.1.3 Liquid Metals

Liquid metals such as eutectic gallium indium (EGaIn) have also been used in stretchable electronic applications. EGaIn (75% Ga 25% In) is a eutectic liquid metal with electrical conductive properties at room temperature.[41–43] The liquid nature of EGaIn allows the material to withstand large amounts of strain where failure is typically dependent on the encapsulating substrate.[44] For example, Mineart et al. demonstrated electrical conductivity of up to 600% strain citing premature failure due to fracturing of polymeric substrate.[43]

2.1.4 Conclusion

In summary, metallic and ceramic thin films are limited in withstanding tensile and bending strains. Nanoparticle materials form percolating networks that are able to withstand larger strains relative to metallic and ceramic thin films. Liquid metals have also been used to avoid mechanical

strain that are present in solid thin films. In the next section, additional strategies to improve stretchability in thin films will be introduced.

2.2 Strategies to Improve Mechanical Stretchability in Functional Materials

2.2.1 Importance of Substrate

The challenge in fabricating robust wearable electronics is designing functional materials to stretch. We have seen that thinner materials are able to withstand larger bending strains, but these materials cannot stretch fracturing at tensile strains of greater than ~1%.[22,23] As previously discussed, research has shown that thinner materials are able to withstand larger bending strains, but fail when flexed any further primarily due to fracturing, slipping, or delamination of the thin film.[45–50] These failure modes occur due to the weak adhesion between the thin film and substrate. By improving the adhesion of the thin film to the substrate has been found to significantly improve the mechanical robustness of thin films due to strain delocalization.[50,51]

Common substrates that have been used to develop stretchable conductors include silicone elastomers such as PDMS and Ecoflex. Research has shown that when thin film conductors are supported by an elastomer, brittle materials are able to withstand relatively larger tensile strains due to strain delocalization.[45,50,52–54] Li et al. reported theoretical calculations demonstrating the interfacial strength between the thin film and substrate is critical in strain delocalization.[51] Their calculations have shown that the interfacial strength help metallic thin films deform uniformly over large tensile strains, whereas weaker interfacial strengths lead to necking at areas of metal debonding or slipping from the substrate.[23,51,55,56]

2.2.2 Interfacial Strength to Substrate

The performance of many devices rely on the interfacial strength between the thin film and substrate.[49,57] As previously shown, weak adhesions lead to debonding and strain localization within the film. One method to address this issue is to use a chemical interfacial layer to provide additional interfacial adhesion strength between the thin film and substrate. For example, Cr is a

popular interfacial layer to improve the interfacial strength between Au and the underlying polymer substrate. However, Cr is known to be brittle causing premature fracturing and electrical failure when mechanically strained.[47,58–61] An alternative method includes using molecular adhesives (i.e (3-mercaptopropyl)trimethoxysilane, MPTMS) to chemically link Au thin films to a silicone polymeric substrate.[47] Byun et al. have shown that introducing a molecular adhesive such as MPTMS helps the adhesion of Au to polydimethylsiloxane (PDMS) and was validated using the "Scotch tape test".

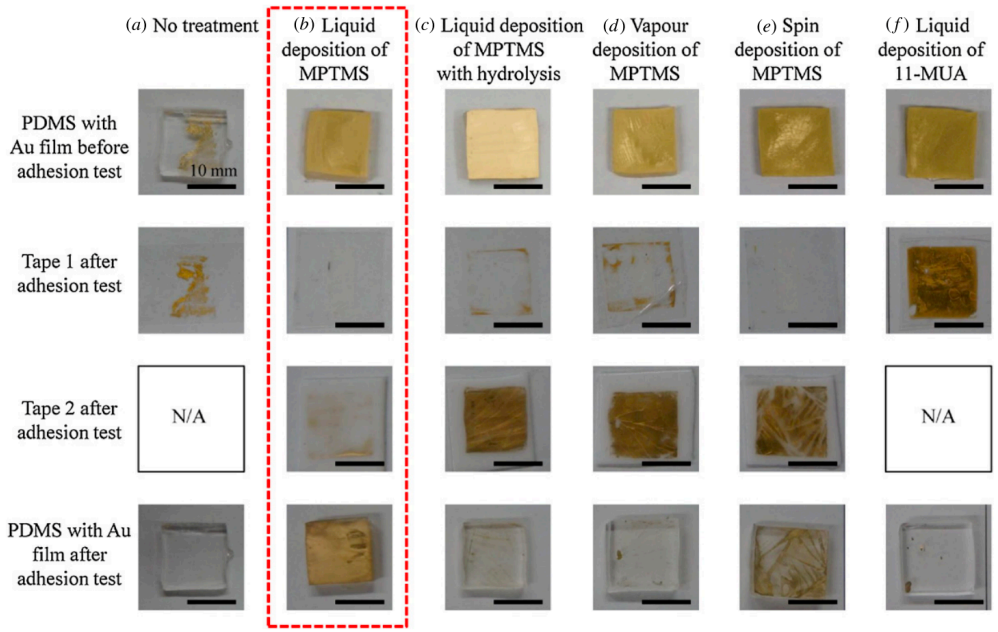

Figure 1. Different methods of MPTMS on Au thin films on elastomeric substrates show differing amounts of interfacial strength.[47] Reprinted with permission.

2.2.3 Geometrical Designs

In addition to chemical strategies, geometrical designs can be used to help provide additional strain relief.[48,62–65] Gutruf et al. have shown that by modulating the curve of the conductive thin film trace, larger strains can be achieved before electrical failure.[66] Xu et al. have also demonstrated that by designing the conductor into 'self-similar' serpentine designs that can rotate in and out of plane, interconnects can reversibly stretch up to 200% without significant

performance degradation.[62] The serpentine designs allowed for thin film rotation in and out of the plane when stretched minimizing strain within the thin film itself.

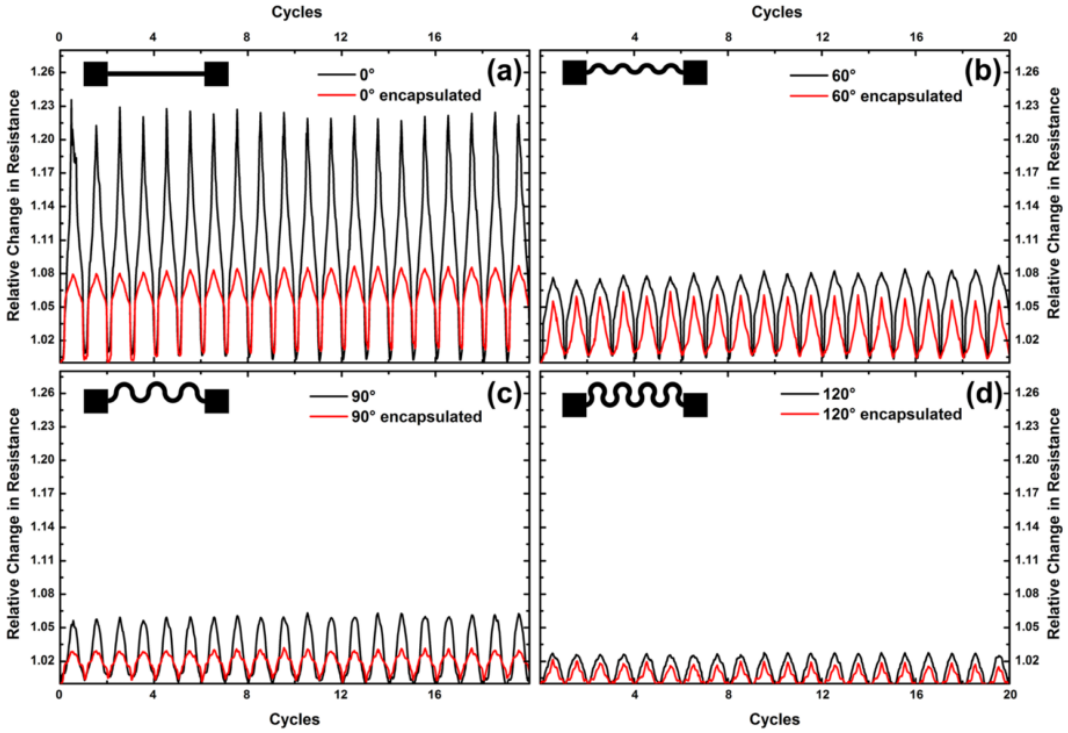

Figure 2. Gutruf et al. demonstrated differing 'serpentine' geometries produce strain relief in Au thin films.[66] Reprinted with Permission.

2.2.4 Nano/Microstructures for Strain Relief

Another strategy to improve the stretchability of thin film materials include introducing geometrical designs such as out of plane buckling for added strain relief.[45,67–69] Lacour et al. produced 'wavy' buckled Au conductors by depositing on top of prestrained polydimethylsiloxane (PDMS) susbstrates.[45] Upon releasing the prestrain in PDMS, the contracting force caused the Au to form periodic buckled structures. They have shown that these buckled structures allow Au thin films to withstand strains of up 100%.

Xu et al. has also introduced wavy ribbon CNT thin films on PDMS substrates.[67] Here they improved conductivity by depositing Au/Pd thin films on the CNT ribbons. These films were then transferred onto a pre-strained elastomeric substrate similar to the methods demonstrated by

Lacour et al. Wavy CNT ribbons were able to withstand strains of up to 100% with minimal increase in electrical resistance.

2.2.5 Shrink Induced Wrinkling with Shape Memory Polymers

Another approach to fabricating micro-nanostructures in functional materials is to use a thermally induced shrinking fabrication process with shape memory polymers. Shape memory polymers are 'smart' polymeric materials that are able to deform back to an equilibrium state with an external stimulus such as heat. Examples of shape memory polymers include materials such as polystyrene (PS) and are commonly used as shrink wrap film in the packing industry. These materials are manufactured by heating the polymer above the glass transition temperature (Tg), stretching to a designated shape, and rapidly cooling while in the strained state. This process 'programs' the material to hold its shape until the material is again heated passed the Tg where it will then return to its equilibrium state.

We have seen that it is possible to form buckled structures by depositing materials onto a pre-strained elastomeric substrate and releasing the strain. Similarly, the shrinking process in shape memory polymers introduces large amounts of compressive stress on thin films leading to the 'wrinkling' of thin films. The results of this shrinking fabrication process will be discussed in the later chapters of this dissertation.

2.3 Compatibility with the Human Body

As mentioned in the previous section, substrates are a critical component to developing stretchable functional materials due to strain delocalization. However, one also has to consider the mechanical properties of which the device will be attached to (i.e. the human body) and ensure the materials are compatible with each other. When stiffness mismatch exists between the device and the human body, delamination occurs during movement resulting in unreliable data acquisition.[70–73] In addition to stiffness mismatch, the human skin consists of wrinkles, pores, hair, and dead skin

cells that may hinder interfacial adhesion of the device to the human body. Therefore, it is critical to design soft wearable electronics to conform the body allowing for reliable data acquisition.

The human skin consists of three main layers including the epidermis, dermis, and the hypodermis. Each of these layers has its own unique mechanical characteristics that are influenced by many factors including age, temperature, hydration, and location.[70,74–82] The outermost layer, epidermis, exists to protect the underlying tissue from the environment, but the dermis and the hypodermis is known to be responsible for protecting the skin from mechanical stress.[74] These layers consist of an intricate network of collagen and elastic fibers that are which aligned with any tension present in the skin, also known as Langer lines.[75] These fibers are immersed in a biological medium such as water, macromolecules, and glycosaminoglycans which are all responsible for the elastic and viscoelastic properties of the human skin.[75,77,78] Although there is some controversy in being able to accurately measure the elastic modulus of the skin, reported results varied anywhere from ~5 kPa-2 MPa on the forearm.[83–87] This is not surprising due to the physiological variation of test subjects, as well as the variation in experimental methods used. Skin also has a non-linear stress-strain curve which also further complicates elastic modulus measurements.[74,81,82]

With a better understanding of the mechanical behavior of skin, it is then possible to choose appropriate substrate materials for soft sensors so that the sensors are mechanical compatible with the human body. Silicone elastomers, for example, are common materials used for fabricating soft sensors due to its favorable mechanical properties and processibility. Typically these materials are platinum-catalyzed materials and cured in the presence of heat.[88]

Depending on the curing conditions and chemistry that is used, the mechanical properties of silicone elastomers will vary.[89] To best match the modulus of the skin, silicone elastomers such as PDMS are commonly used. PDMS is a common silicone elastomer that has a Young's modulus ~1.3-3 MPa (Sylgard 184 10:1 A:B, Down Corning)[89]. Evidently, the mechanical properties of

PDMS closely matches that of the mechanical properties of the human skin. Softer silicone elastomers, such as Ecoflex 0030 (*E*: ~60kPa, Smooth-On) have also been used to more closely match the elastic modulus of the human skin allowing for more conformal contact.

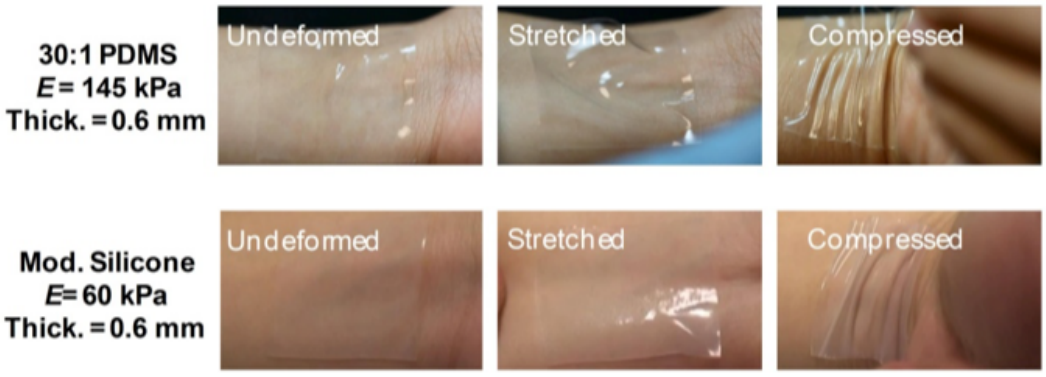

Figure 3. Behavior of silicones with different elastic moduli on the human body.[73] Reprinted with permission.

CHAPTER 3: MECHANICAL SENSOR MODALITIES

Strategies to improve the flexibility and stretchability of thin film materials have been reviewed. Thin film materials are inherently more flexible than its bulk counterpart as explained by a simplified pure bending mechanics. To improve the stretchability of brittle materials, numerous designs can be implemented including using elastomeric substrates, buckled structures, high aspect ratio nanomaterials, and liquid metals. In the next section, different types of mechanical sensors incorporating these strategic designs for fabrication of flexible and stretchable wearable electronics will be discussed. Focus will be placed on piezoresistive and piezocapacitive strain and pressure sensors. It is worth noting piezoelectric sensors have also been reported but will not be discussed in this work.

3.1 Piezoresistivity

When conductive materials are subjected to mechanical deformation, its electrical properties change. This electromechanical response is known as the piezoresistive effect. Due to the poisson ratio, v, materials that are elongated also contract in the transverse direction of elongation. Consequently, the resistance of a conductive material will change as shown by the following equation:

$$R = p\frac{L}{A} \tag{2}$$

where ρ is electrical resistivity, L is the length, and A is the cross-sectional area of the conductor. In semiconducting materials, the piezoresistive effect is dominated primarily by bandgap changes due to strain. Therefore, the resistivity of the material changes in response to mechanical strain. In addition to geometrical effects on resistance, micro-cracking has often been utilized to fabricate sensitive strain sensors.

The piezoresistive effect has been widely used in wearable electronics for the detection of human physiological movement due to its strain sensitivities characteristics, and simple device designs.[66] The challenge in designing wearable strain and pressure sensors must meet a certain criteria including: high stretchability and flexibility, repeatability, low hysteresis, and high sensitivity. The device must be able to stretch and flex when mounted on the body allowing for long term use. A reliable wearable strain sensor will also not exhibit extensive plastic deformation when subjected to repeated strain. Wearable electronics are commonly fabricated using viscoelastic silicone elastomers which suffer from hysteresis; therefore, it is critical to minimize the hysteretic effects. Most importantly, conformal sensors must exhibit high sensitivity to strain to improve signal acquisition and detections of dynamic strain. Strain sensitivity is typically characterized by the gauge factor:

$$GF = \frac{\frac{(R - R_o)}{R_o}}{\varepsilon} \tag{3}$$

where R is the final resistance, R_o is the initial resistance, and ε is strain. Similarly, pressure sensitivity can also be defined by:

$$S = \frac{\frac{(R - R_o)}{R_o}}{P} \tag{4}$$

where S is pressure sensitivity, R is the final resistance, R_o is the initial resistance, and P is pressure.

3.1.1 Strain sensor

The simplest wearable strain sensor, that have flexible and stretchable attributes, consist of a thin film conductor on a silicone elastomer (i.e PDMS). When these conductors are stretched, the geometrical change, and micro-cracking induces a change in electrical resistance. Therefore,

it is possible to mount these strain sensors on the human body to detect and quantify motion, such as the bending of a finger, elbow, or knee.

As previously mentioned, Gutruf et al. demonstrated the electromechanical response of Au thin films on polyimide.[66] In the most ideal case, the change in resistance of a straight Au conductor can be estimated by:

$$R = R_o \frac{(1 + \varepsilon)}{(1 - v\varepsilon)^2} \quad (5)$$

where R is resistance, v is the Poisson's ratio, and ε is strain. When the Poisson's ratio of gold is 0.44 and strain is 3%, the estimated change in resistance is 5.8% corresponding to a GF of 1.93. However, Gutruf's experimental value shows that there was a 22% change in resistance when strained out to 3%, corresponding to a GF of 7.33. The primary reason for this large discrepancy was attributed to micro-cracking within the Au conductor.

3.1.2 Microcracking Strategy

This may seem destructive to the thin film, but the micro-cracking strategy has been widely adopted to fabricate sensitive strain sensors.[90,91] For example, Kang et al. reported nanoscale crack junctions in Pt thin films inspired by the crack-shaped slit sensory organs of spiders.[90] These nanoscale crack junctions were achieved by bending Pt thin films over a set curvature. Using this controlled cracking strain sensor, GF of 2000 over a range of 0-2% was achieved allowing detections of sound vibrations. In comparison with to the no crack sensor, there was a 450 fold increase in strain sensitivity at 0.5% strain with the cracked sensor. However, the durability and stretchability was limited showing signal degradation at about 500 cycles at 2% strain.

As previously discussed, high aspect ratio nanomaterials, such as carbon nanotubes (CNTs), can be used to fabricate highly stretchable devices. Due to the high aspect ratio of these nanoparticles, each individual particle remain in contact with each other during high strains.

Amjadi et al. used a spray gun deposition method to deposit thin films of CNT onto a silicone elastomer and was able to achieve 500% strain with a measured GF of 1.75.[92] Silver nanowires (AgNWs) have also been shown to withstand strains of up to 70% with a range of GF's from 2-14.[32] It is also possible to incorporate buckled structures using the shrinking fabrication process within CNT thin films to greatly improve stretchability of up to 750% strain, with a GF of 0.65.[93] The wrinkled structures in CNT thin films will be discussed in a later chapter.

3.1.3 Piezoresistive Pressure Sensor

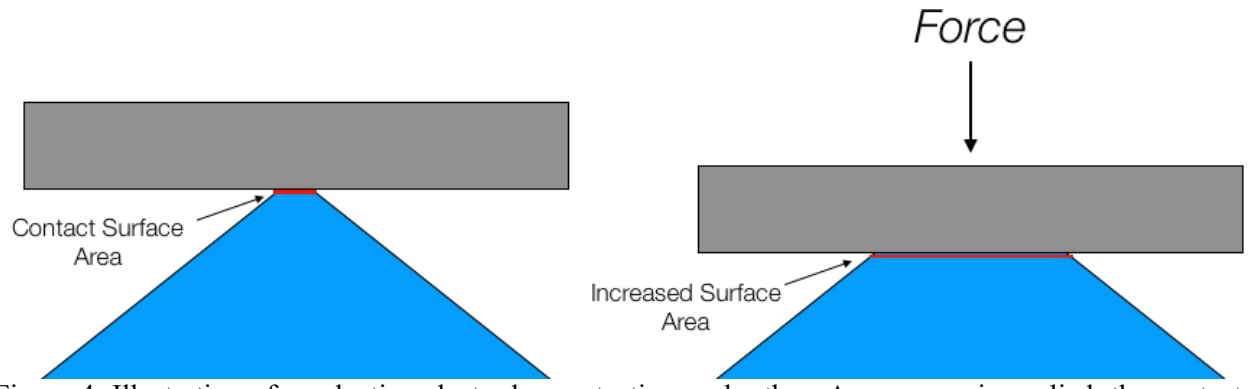

Figure 4. Illustration of conductive electrodes contacting each other. As pressure is applied, the contact surface area between the electrodes increase which reduces the electrical resistance between the electrodes.

Piezoresistivity can also be leveraged to fabricate highly sensitive pressure sensors. Piezoresistive pressure sensors are fabricated by adjoining two electrodes that will have some electrical contact resistance. When these electrodes are deformable, more electrical contact points can be made with added pressure which will reduce the electrical contact resistance between the two electrodes. Further improving pressure sensitivities can be accomplished by creating topographical features in the electrodes that can deform with increasing pressure. Choong et al. were able to achieve pressure sensitivities of up to 10.3 kPa^{-1} when stretched up to 40% for pressures less than 10 kPa by incorporating micropyramid PDMS arrays.[94] An illustration demonstrating the mechanics can be seen in figure 4. They have found that as the micropyramid

structures deform under pressure, there is an increased surface area contact with the counter electrode which reduced the overall electrical resistance of the sensor.

3.1.4 Conclusion

Evidently, in order to fabricate highly sensitive strain sensors, stretchability must be compromised. Conversely, highly stretchable strain sensors are characterized with low GF's, or strain sensitivities. In addition, stretchable strain sensors suffer from hysteresis due to the viscoelastic properties of silicone elastomeric substrates. Piezoresistive pressure sensors are characterized with very simple device designs. By integrating microstructures in the electrodes, it is possible to improve pressure sensitivities and be able to detect small pressures.

3.2 Piezocapacitance

Capacitors have also been used for mechanical pressure sensors. A typical capacitor consists of two parallel plates separated by some dielectric material. When a potential is applied, the total capacitance of a parallel plate capacitor is equal to:

$$C = \varepsilon_o \varepsilon_r \frac{A}{d} \tag{6}$$

where C is capacitance, ε_o is the permittivity of space, ε_r is the relative permittivity of the dielectric material, A is the surface area overlap of the electrodes, and d is the distance separating the electrodes. As shown by Equation 6, when the distance between the parallel plates decrease capacitance will increase. Therefore, pressure sensors can be constructed as capacitors where pressure compresses the parallel plates closer together to increase capacitance. Capacitive sensors are typically characterized with low power consumption, and quick response times.

3.2.1 Dielectric

Dielectric materials are insulating materials that can be polarized in the presence of an electric field. The degree of polarization in the presence of voltage reflects the amount of total electrical energy that can be stored which describes the total capacitance of the system. When designing flexible capacitive pressure sensors, it is important to determine a suitable dielectric material. Such materials include soft polymers that have relatively small Young moduli, such as PDMS. Silicone elastomers have dielectric permittivity of approximately 3.

Creating topographical features in dielectric materials may improve pressure sensitivities by reducing the total elastic resistance from pressure. For example, Mannsfeld et al. created micropyramidal structures PDMS dielectric. They have found that these structures reduce the overall elastic resistance in the presence of pressure.[95] In addition, they have speculated that the overall permittivity of the dielectric material is dynamic in response to pressure. This is due to the presence of air gaps in the dielectric material which reduces the effective dielectric permittivity of the dielectric. As the dielectric material is compressed, the dielectric permittivity reaches closer to that of bulk PDMS as the air gap volume is reduced.

3.2.2 Strain Sensing

Piezocapacitive sensors can act as strain sensors. This is due to the fact that capacitive sensors can compress in the transverse direction of tensile strain due to the Poisson effect. The compression of the dielectric material reduces the thickness thereby increasing nominal capacitance. The electromechanical response of tensile strains are shown in equation 5:[96,97]

$$C = \varepsilon_o \varepsilon_r \frac{(1+\varepsilon) l_o (1 - v_{electrode}) w_o}{(1 - v_{dielectric}) d_o}$$

$$= \varepsilon_o \varepsilon_r \frac{(1+\varepsilon) l_o w_o}{d_o} \quad (5)$$

$$C = (1 + \varepsilon)C_o$$

where ε is the tensile strain, $v_{electrode}$ is the Poisson's ratio of the electrode, and $v_{dielectric}$ is the Poisson's ratio of the dielectric. It is possible to assume the Poisson's ratio of the electrode is characteristic of the Poisson's ratio of the underlying substrate. Therefore, assuming the underlying substrate and the dielectric material has equal or similar Poisson's ratio, the electromechanical response to strain will be linear as seen in Equation 5. This scenario assumes that the material is isotropic and the Poisson's ratio does not change respect to increasing strain. One advantage of capacitive strain sensors over piezoresistive sensors is that the electromechanical response does not depend on the resistive properties of the electrodes, which typically are affected greatly by hysteresis.

3.2.3 Pressuring Sensing

In addition to strain sensing, pressure sensing is possible with capacitive sensors. As previously stated, capacitive sensors are comprised of two parallel electrodes. Mechanical pressure will reduce the distance between the electrodes thereby increasing nominal capacitance. The pressure sensitivity of capacitive pressure sensors highly depends on electrical and mechanical properties of the dielectric material. Softer materials as well as incorporating microstructures can improve pressure sensitivities. However, capacitive pressure sensors are typically characterized with lower pressure sensitivities due to relatively small deformations of the dielectric material.

One method that have been proposed to improve the pressure sensitivities of capacitive pressure sensors is to not only change the elastic resistance of the dielectric layer, but also to engineer a dielectric layer that has a dynamic permittivity constant.[28,95] This can be shown by the following equation:[28]

$$\frac{\Delta C}{C_o} = \frac{\varepsilon_o \varepsilon_r \, (A/d)}{\varepsilon_o \varepsilon_{ro} \, (A/d_o)} - 1 = \frac{\varepsilon_r d_o}{\varepsilon_{ro} d} - 1 \qquad (6)$$

As seen in equation 6, the normalized change in capacitance is not only dependent on the distance between the electrodes. It is also possible to improve the normalized change in capacitance by engineering a dielectric material to have an increased dielectric permittivity. This can be accomplished by adding conductive fillers to the dielectric material. When compressed, the conductive filler spacing will get closer leading to an increased dielectric permittivity.[28] Other variables can also be modified such as an increase surface area overlap of the electrodes, but this is much more difficult to achieve.

3.2.4 Conclusion

The drawback of capacitive sensors is that they are typically characterized with low pressure sensitivities. However, the linear response, quick response times, and low power consumption makes capacitive sensors highly desirable. Many strategies have been proposed in developing sensitive pressure sensors including modifying the topographical features of the dielectric material. Improving pressure sensitivities have allowed for detections of subtle physiological signals including voice detection on the throat and pulsatile blood flow on the radial artery.

CHAPTER 4: HIGHLY STRETCHABLE WRINKLED GOLD THIN FILM WIRES

The next chapters will report work using a thermally induced shrinking fabrication process to form highly wrinkled structures in functional thin film materials. The work presented here has been built on many of the concepts previously mentioned to improve flexibility and stretchability in brittle thin film materials for wearable sensing applications.

4.1 Introduction

The rapid growth in flexible and stretchable electronic development for wearable electronics has spurred the need for stable and robust electrical interconnection. Unlike traditional rigid electronics, the electrical components of soft sensors must conform to curvilinear surfaces, stretch with the body, and remain electromechanically robust. In this work, the piezoresistive response of shrink induced wrinkled metal thin films under strain demonstrates electrical conductivity withstanding strains of up to 200%. Up to 100%, these stretchable wrinkled metallic thin films showed relatively low changes in electrical resistance. In addition, these electrical stretchable wires showed robustness from cyclic strain. These wrinkled metallic thin films were manufactured using low cost and rapid prototyping methods and can be quickly translated to roll-to-roll manufacturing techniques.

As mentioned in the previous chapters, there has been a number of efforts in developing soft sensors that are able to stretch and flex. These efforts have focused on strain delocalization on substrates, improving interfacial strengths between the functional material and the substrate, using high aspect ratio nanoparticles that form percolating networks, and also forming strain relieving ‘buckled’ features in functional materials. Research has shown that these buckling features provide large amounts of strain relief. For example Jiang et al. have shown that silicon thin films with

buckled structures were able to withstand strains 20 times more than the intrinsic tensile strengths of silicon.[98]

Here I report self-similar wrinkled micro-nanostructures in Au thin films for stretchable wire applications. Previous work has shown that highly wrinkled structures can form in a thermally induced shrinking fabrication process.[99,100] Buckling forms in Au thin films due to the large amount of compressive stress on the Au thin film during the shrinking process. I will demonstrate a fabrication process that achieved successful transferring of wrinkled Au thin film from a hard, thermoplastic material onto a soft elastomeric substrate enabling stretchable applications.

4.2 Experimental Methods

Polystyrene (PS, Grafix Arts) was thoroughly cleaned with 70% ethanol and deionized water. Electrode pattern was designed using CAD software (Autodesk, Inc., CA). The pattern was then cut on a shadow mask (Frisket film, Grafix) using a CO_2 laser (VLS2.30, Universal Laser Systems, AZ) and placed on the cleaned PS substrate. 25nm Au thin film was deposited on the PS using electron beam evaporation (E-BEAM, CHA MARK 50, CA). The PS substrate was then heated up to 150^{o}C to induce biaxial shrinking. The wrinkled Au film was then treated with 5mM (3-mercaptopropyl) trimethoxysilane (95% MPTMS, Sigma-Aldrich, MO) (MPTMS) to promote adhesion to the silicone elastomer. Ecoflex 0030 (Smooth-On, PA) was then cured and bonded to the wrinkled Au thin film. The wrinkled Au thin film was then transferred onto Ecoflex by placing the sample in an acetone bath followed by a washing step with toluene. Sheet resistance was measured using a four-point probe station with a rapid source measuring unit (2612B SourceMeter, Keithley, OH). Electromechanical measurements were accomplished by mountint the wrinkled Au thin film wires in a custom-made tensile stretcher. The resistance of the wire was measured using a multimeter (MS8240D, Mastech, CA) at various strains. Wrinkled topographical structures were imaged using scanning electron microscope (Magellan XHR 400L FE-SEM, FEI,

OR). DSLR camera (Canon 5D MkIII, Canon, Japan) was used to take images of the green LED

Matlab was used to analyze the RGB values of the LED at various strains.

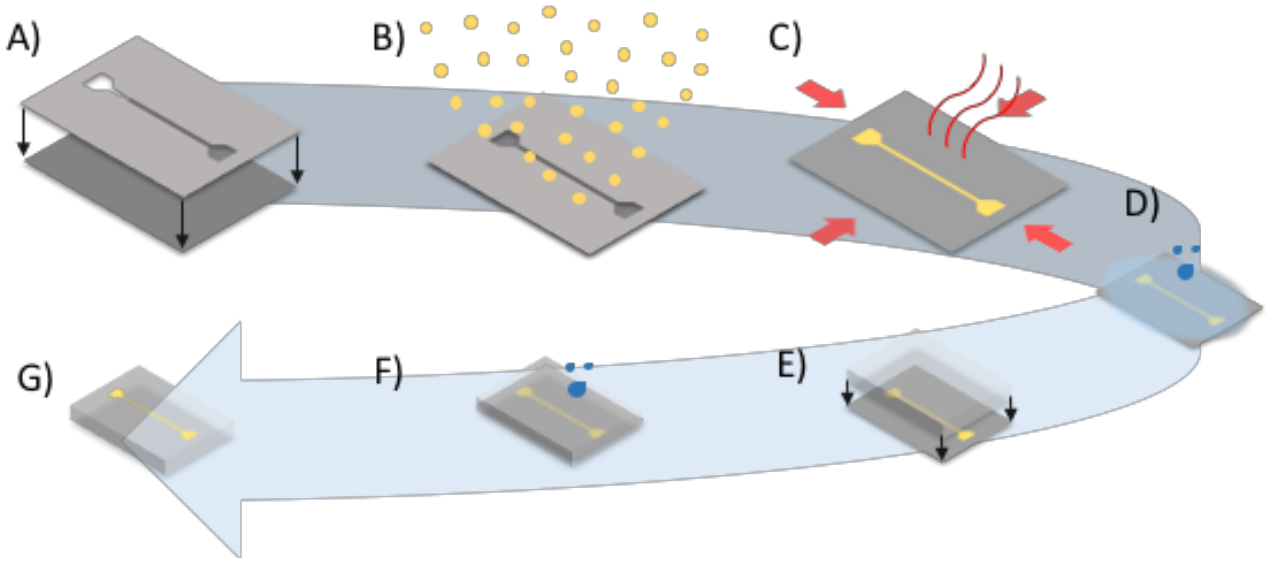

Figure 5. a) Shadow mask is first mounted onto the substrate. b) Electron beam deposition of Au through the shadow mask. c) PS substrate is subsequently heated passed the glass transition temperature. d) MPTMS chemical linker treatment. e) Silicone elastomer spin coated and cured on substrate. f) Lift-off from thermoplastic using organic solvent bath. g) Final wrinkled Au thin film on Ecoflex.

4.3 Results and Discussion

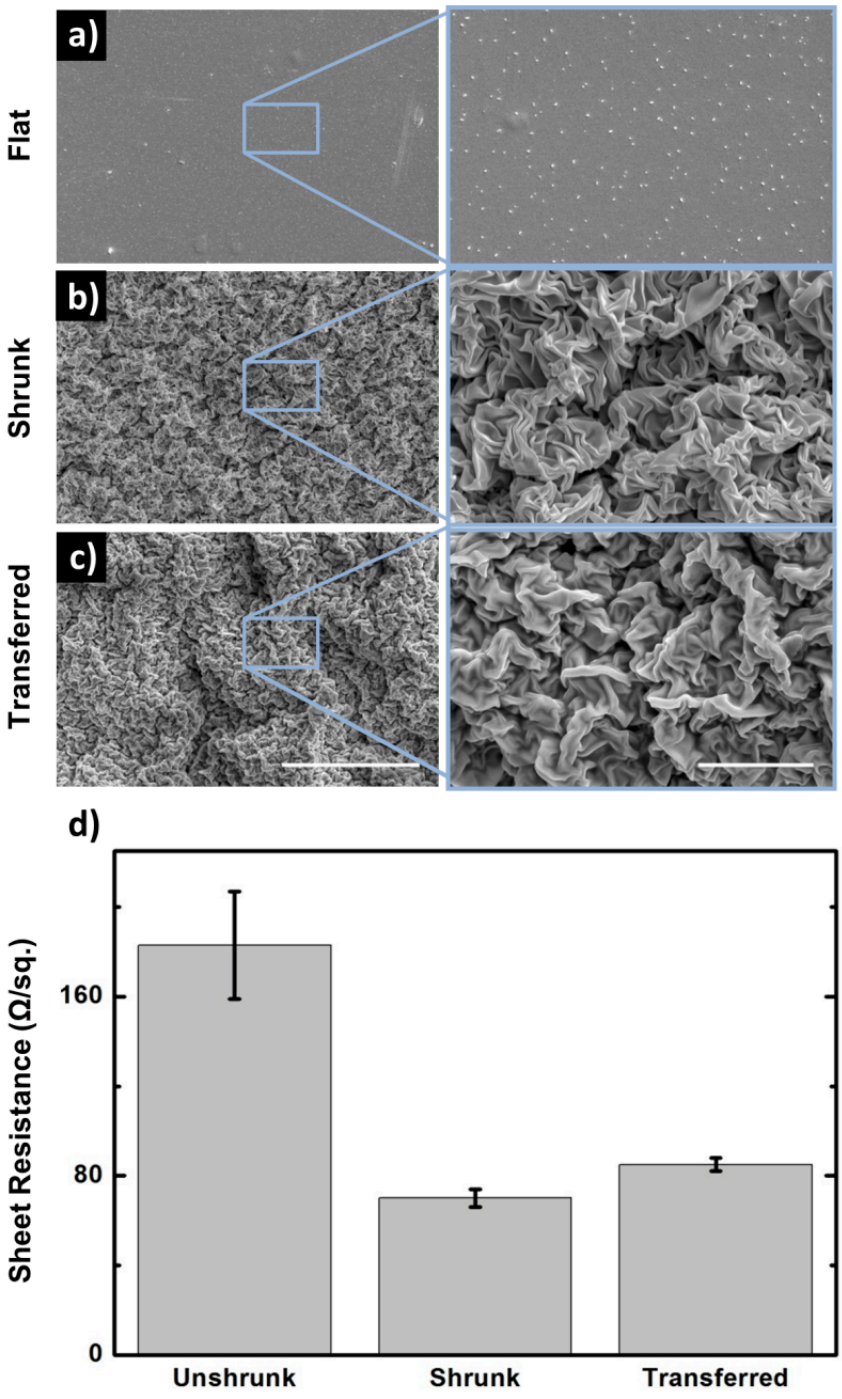

Figure 6. SEM images of Au thin film at various stages of the fabrication process. (a) Au film on PS substrate. (b) After thermally induced shrinking Au film on PS substrate. (c) Transferred wrinkled Au thin film. d) van der Pauw sheet resistance measurements. Left column scale bar and inset are 30μm and 5μm.

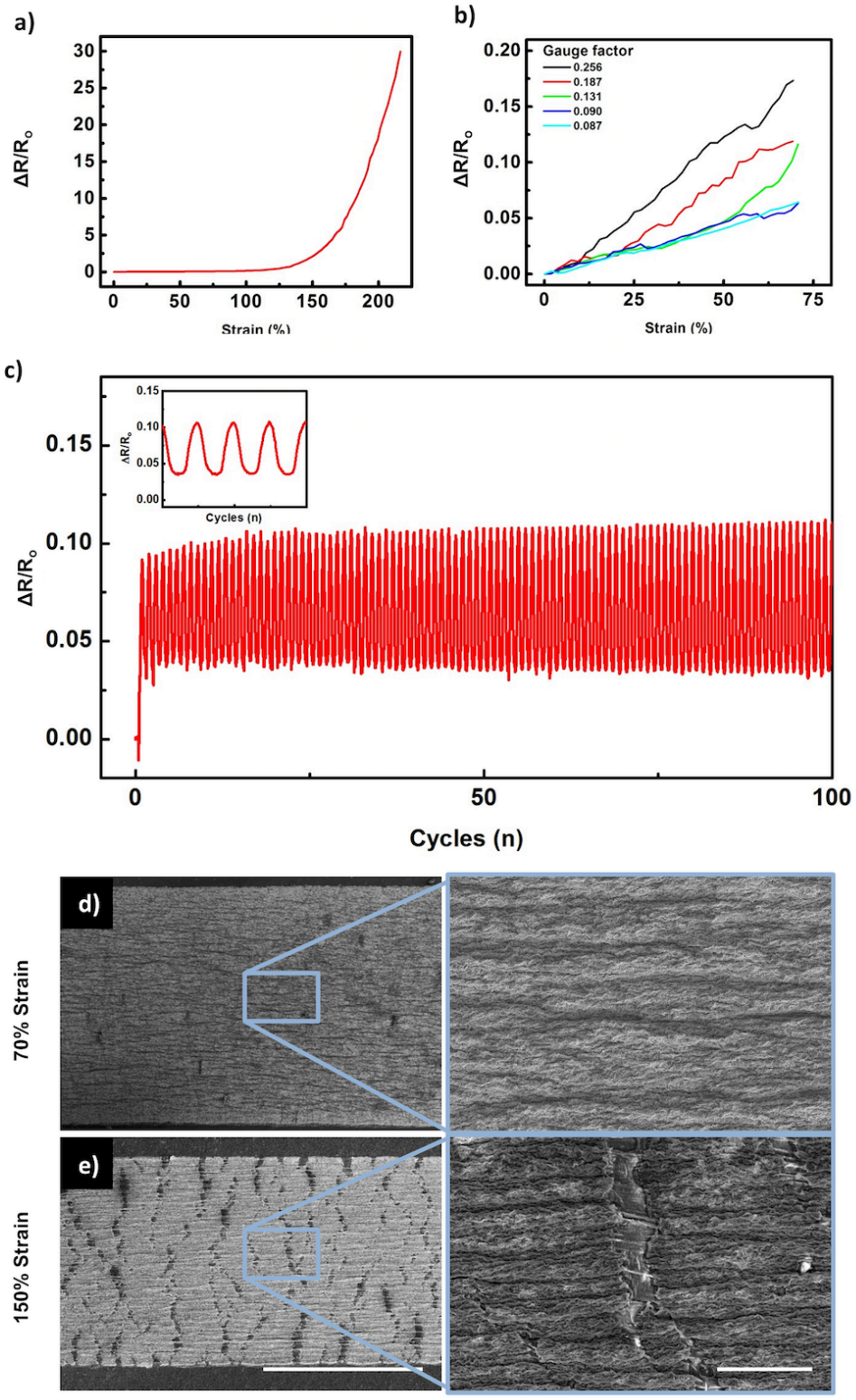

Figure 7. a) Wrinkled Au thin film wire strained to failure. b) Gauge factor of five sensors measured at 70% strain. c) 100 cycles of 50% strain. d) SEM image of wrinkled Au thin film strained to 70% and e) 150% strain. Left hand column scale bar the insets are 500μm and 50μm respectively.

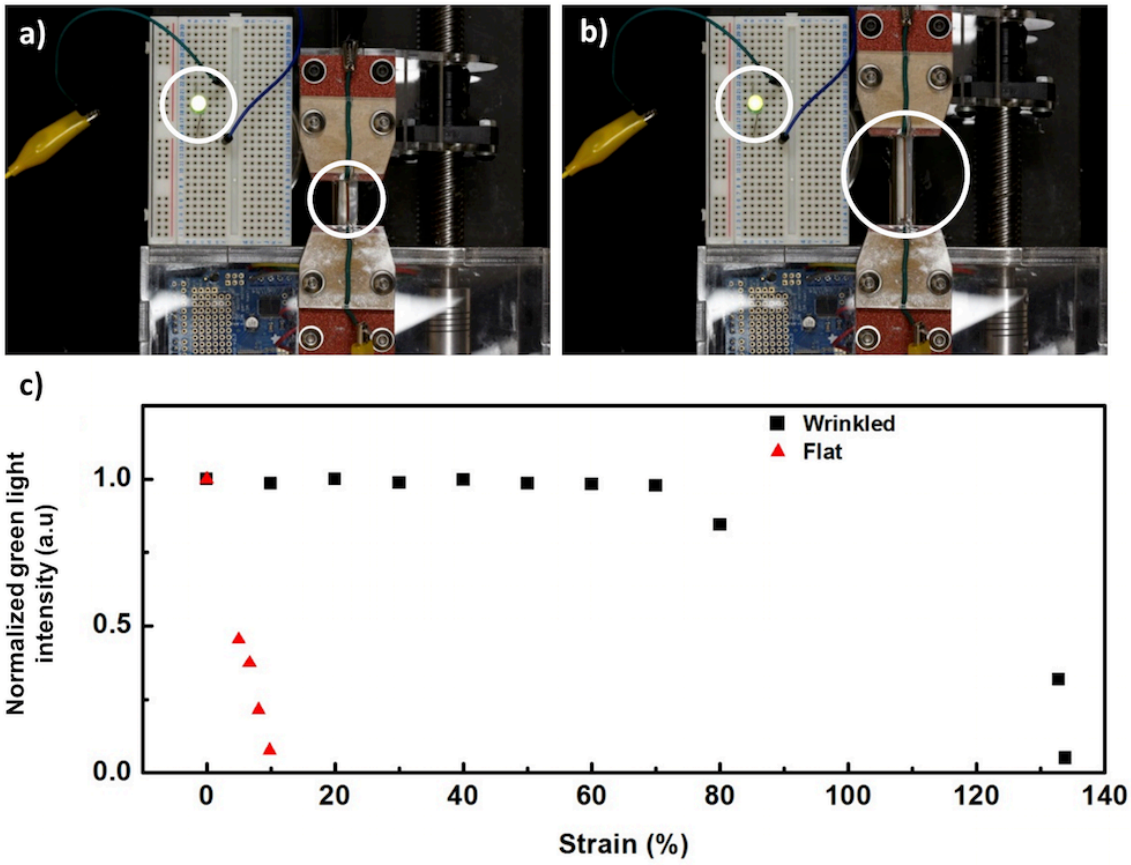

Figure 8. a) Normalized LED green light intensity plot of wrinkled Au thin film vs flat Au thin films strained to failure. b) Wrinkled Au thin film at 0% strain and at c) 80% strain. Circles denote green LED and wrinkled Au stretchable wire.

Figure 5 illustrates the fabrication process flow for wrinkled Au thin films on Ecoflex. The initial patterned electrode geometry was 2.5 mm wide and 45 mm long. After heat induced biaxial shrinking, the final dimension of the electrodes was approximately 1 mm wide and 15.5 mm long. These wrinkled Au thin film wires were then transferred onto Ecoflex with a final thickness of 1 mm.

Figure 6. illustrates the Au thin film throughout the fabrication process. First, the Au thin film is deposited onto the PS substrate. Small Au nanoparticles that have nucleated can be seen on the surface. After thermally induced shrinking, the wrinkled Au thin film structures can be seen.

After transferring onto the Ecoflex, the morphology of the wrinkled structures slightly changed. Much of this can be explained by the thermal mismatch between the Au thin film and the Ecoflex material.[101] In addition, soft polymers such as Ecoflex are susceptible to organic solvents which cause them to swell. After drying, the Ecoflex material itself has shrunk slightly which may have created lower frequency wrinkled structures seen in the SEM images.

The van der Pauw method was used to characterize the intrinsic electrical properties of the Au thin films as seen in figure 6.[102] Flat 25nm Au thin films on PS substrates had sheet resistances of 183 Ω/square ± 24. Upon shrinking, the metallic Au thin films displayed a decrease in sheet resistance by a factor of 2.6 at 70 Ω/square ± 4. After transferring, the sheet resistance of transferred wrinkled Au thin film wires increased slightly to 85 Ω/square ± 3. This could have been attributed to increased mechanical strain introducing microcracks in the Au thin film. The reduction in sheet resistance is believed to be due to the reduction in conductive path length due to the folding wrinkled structures contacting each other such that the overall thickness of the material is virtually thicker than what was initially deposited. Further investigation is required to validate these claims.

The electrical response of the wrinkled Au thin film wires was then measured in response to mechanical strain. The electromechanical tests were conducted using a custom-made tensile stretcher. Samples were mounted onto the tensile stretcher and subsequently strained to electrical failure**.** Figure 7 illustrates the electromechanical response of the wrinkled Au thin film wires when strained to electrical failure. As seen in the electromechanical response plot, the wrinkled Au thin film wires were able to withstand tensile strains of up to 200% showing relatively low changes in electrical resistance of up to 100% strain. In comparison, the flat Au thin films transferred onto Ecoflex were only able to withstand strains of up to 30% before electrical failure. This indicates

that wrinkled Au thin films provide significant amount of strain relief allowing functional materials to strain beyond the instrinsic mechanical properties of Au.

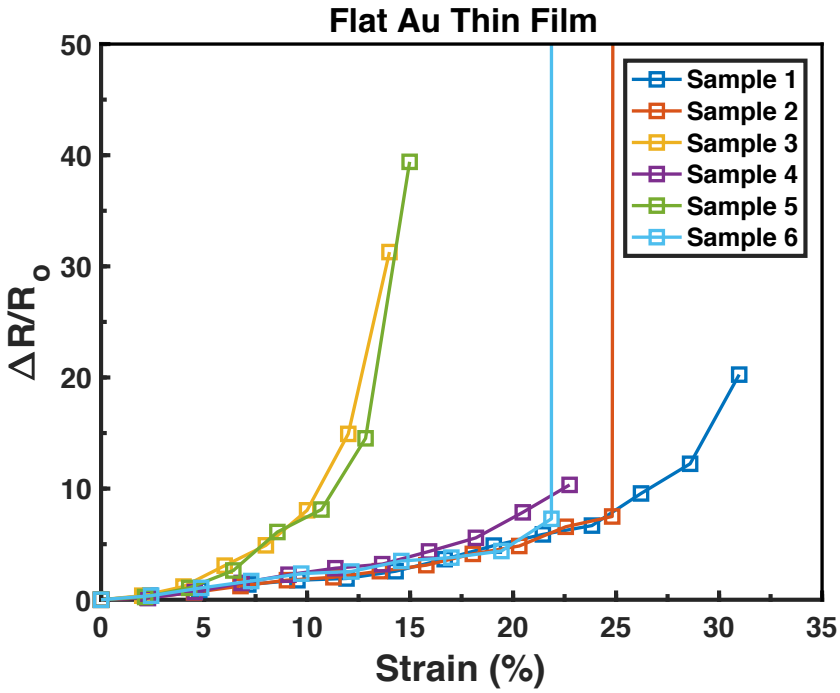

Figure 9. Flat Au thin films strained to failure. Note that flat Au thin films were only able to withstand strains of up to 30%.

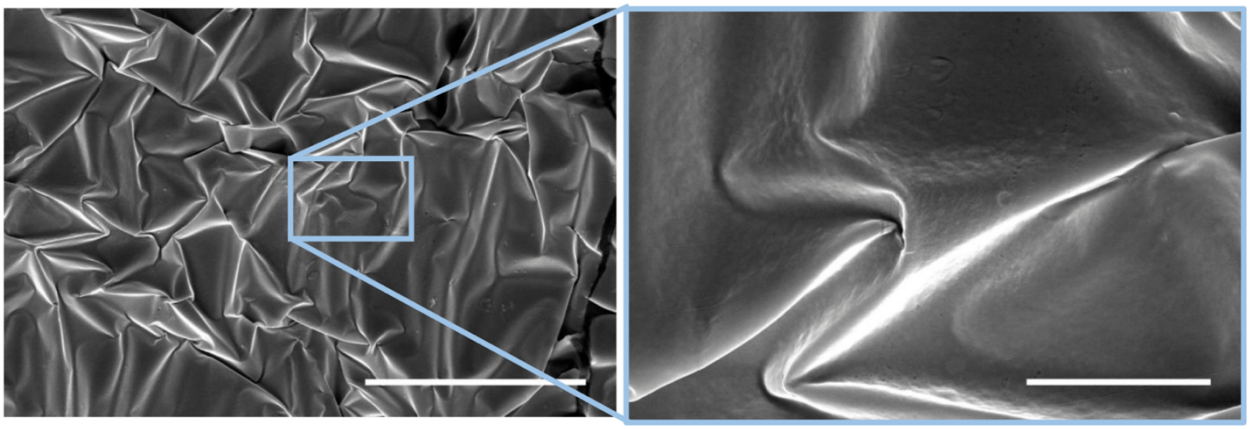

Figure 10. Transferred flat Au thin film onto Ecoflex. Scale bar on left is 30μm, and the inset on the right is 5 μm. Note that there is some slight wrinkling present even in the Au thin film. This is due to spontaneous thermal expansion and relaxation of metallic thin films on soft elastomeric substrates.[101]

As stated before, gauge factor (GF) is a figure of merit that describes the electrical sensitivity of a material in response to strain. As shown in Figure 7b, the wrinkled Au thin film wires exhibit GF's as low as 0.083 of up to 70% strain. The GF of the wrinkled Au thin film wires increased sharply after 100% strain. This increase is attributed due to the aforementioned failure mechanisms of thin films on substrates including delamination and crack propagation. This can be apparent in the SEM images of wrinkled Au thin films strained to 70% and 150%.

Robustness of the wrinkled Au thin films were tested by inducing cyclic mechanical strain. As seen in Figure 7c., the wrinkled Au thin film was strained for 100 cycles at 50% strain. There is a large initial increase in electrical resistance. This is possibly due to crack propagation and delamination of the wrinkled thin film. This stage can be considered the conditioning phase which is apparent in many elastic conductors.[66] After several cycles, the electromechanical response of the wrinkled Au thin film stabilized. This suggests that the defects in the wrinkled Au thin films are reversible illustrating strain delocalization. 7% normalized change in electrical resistance was measured at 100 cycles of 50% strain corresponding well with the strain to failure plot shown in Figure 7a. which reports 6% change in normalized change in electrical resistance at 50% strain.

The wrinkled Au thin films were than attached to LED to demonstrate stretchable wire applications. The LED was powered with a power supply setting the limits at 2.85V and 0.020A. Digital Single Lens Reflex (DSLR) camera was used to image the LED light intensity. The LED light intensity was approximated by measuring the Red Green Blue (RGB) components of the LED light source. For simplicity, only the green component of the RGB spectrum was analyzed. The green pixel intensity was then measured and normalized at various strains. The green light pixel intensity did not diminish of up to 70% strain. After 80% strain, the green light intensity dropped. In comparison, the green light intensity of flat Au thin films dropped dramatically of up to 15% strain.

4.4 Conclusion

In conclusion, I have introduced a thermally induced shrinking fabrication process for developing wrinkled Au thin film stretchable wires using thermoplastics. The increased surface area and the additional interfacial strength from the MPTMS chemical linker improved strain delocalization in the metallic thin film. These engineering strategies improved the stretchability of wrinkled Au thin film wires by up to 6-7 fold allowing strains of up to 200% and also showing relatively small changes in electrical resistance of up to 100% strain. Future studies to improve robustness may include strategies mentioned in the previous chapters such as encapsulation and optimized geometrical patterns.

CHAPTER 5: HIGHLY STRETCHABLE CARBON NANOTUBE THIN FILMS AND MOTION DETECTION

5.1 Introduction

In the previous chapter, highly stretchable Au thin film wires were introduced using a thermally induced shrinking fabrication process platform. As reported earlier, wrinkled structures formed during the shrinking process due to the large amount of compressive stress on the Au thin film. Similarly, wrinkled structures in CNT thin films may also form. Here, I report fabrication of wrinkled CNT thin films using the same thermally induced shrinking fabrication process platform. In addition, human motion detection applications will be shown using wrinkled CNT thin films.

5.2 Experimental Methods

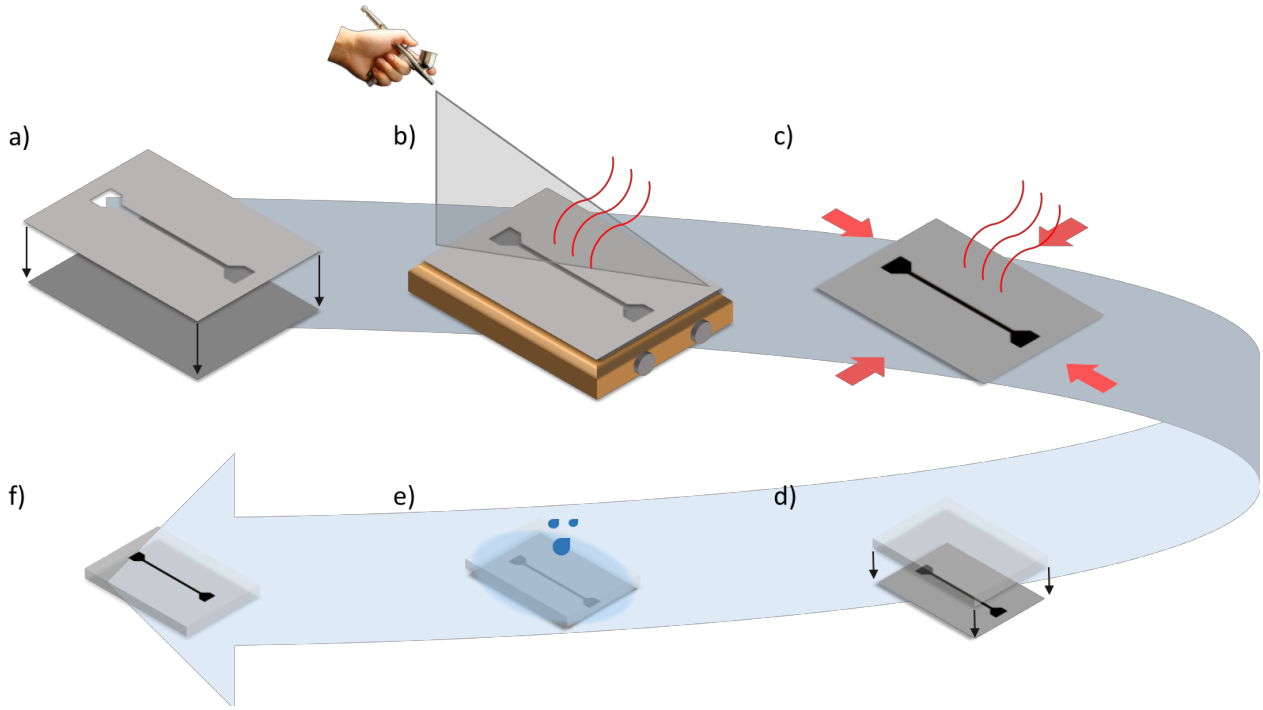

Figure 11. Fabrication process flow for wrinkled CNT thin film strain sensor. a) Shadow mask is placed on a PS substrate. b) Aqueous CNT solution is spray coated on heated substrate. c) Substrate is heated passed glass transition temperature to induce biaxial shrinking. d) Silicone elastomer is cured on top of substrate. e) Transfer is completed using an organic solvent transfer process. f) Final wrinkled CNT thin film.

Fabrication process of wrinkled CNT thin films are similar to that of wrinkled Au thin films. A shadow mask (Frisket Film, Grafix Arts) was first designed in a dog shape pattern using CAD software (AutoCad) and placed on a PS substrate (Grafix Arts). CNT dispersion was first made by sonicating sodium dodecyl sulfate (SDS) (10mg mL^{-1}; Bio-Rad Laboratories), deionized water, and SWCNTs (80 wt%, 1 mg mL^{-1}; Cheap Tubes) for 3 hours. The resulting solution was then centrifuged (12000 RPM, 70 minutes) and decanted (90% supernatant). The decanted CNT solution was then deposited using an air atomizing spray gun onto a heated (60^{o} C) PS substrate. The atomization spraying process provides more confluent and homogenous CNT thin films.[103,104] The substrate heating process also allowed for the atomized CNT solution to evaporate leaving only the CNT thin film on the PS substrate. After CNT deposition, the PS was removed from the shadow mask and then heated passed the glass transition temperature to induce shrinking of the substrate. This shrinking process subsequently formed wrinkled CNT thin films. The wrinkled CNT thin films were then transferred onto a soft silicone elastomer, Ecoflex. Figure 12 shows SEM images of flat CNT thin films deposited onto PS substrate and wrinkled CNT thin films after the thermally induced shrinking process.

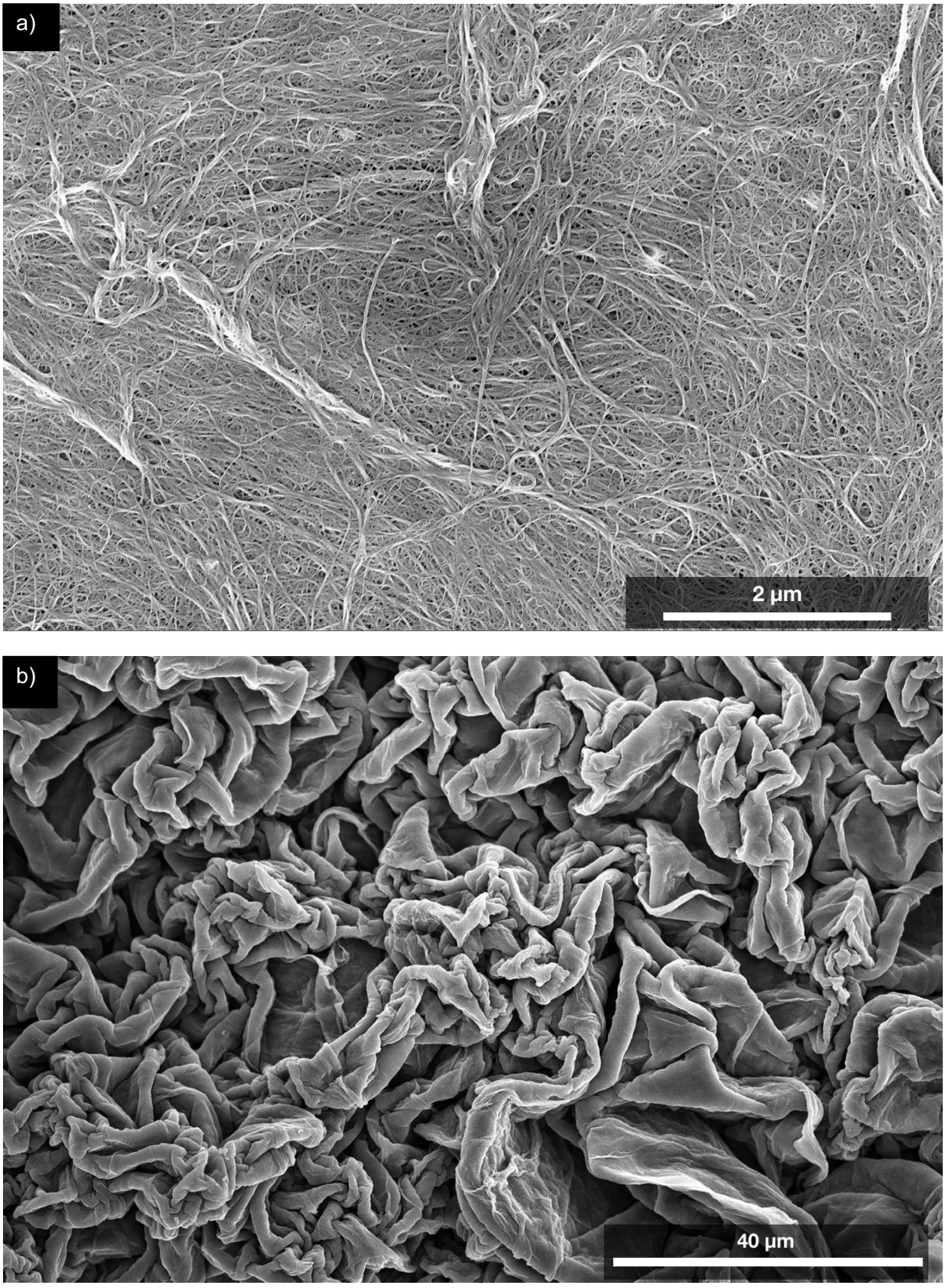
a)
2 µm
b)
40 µm

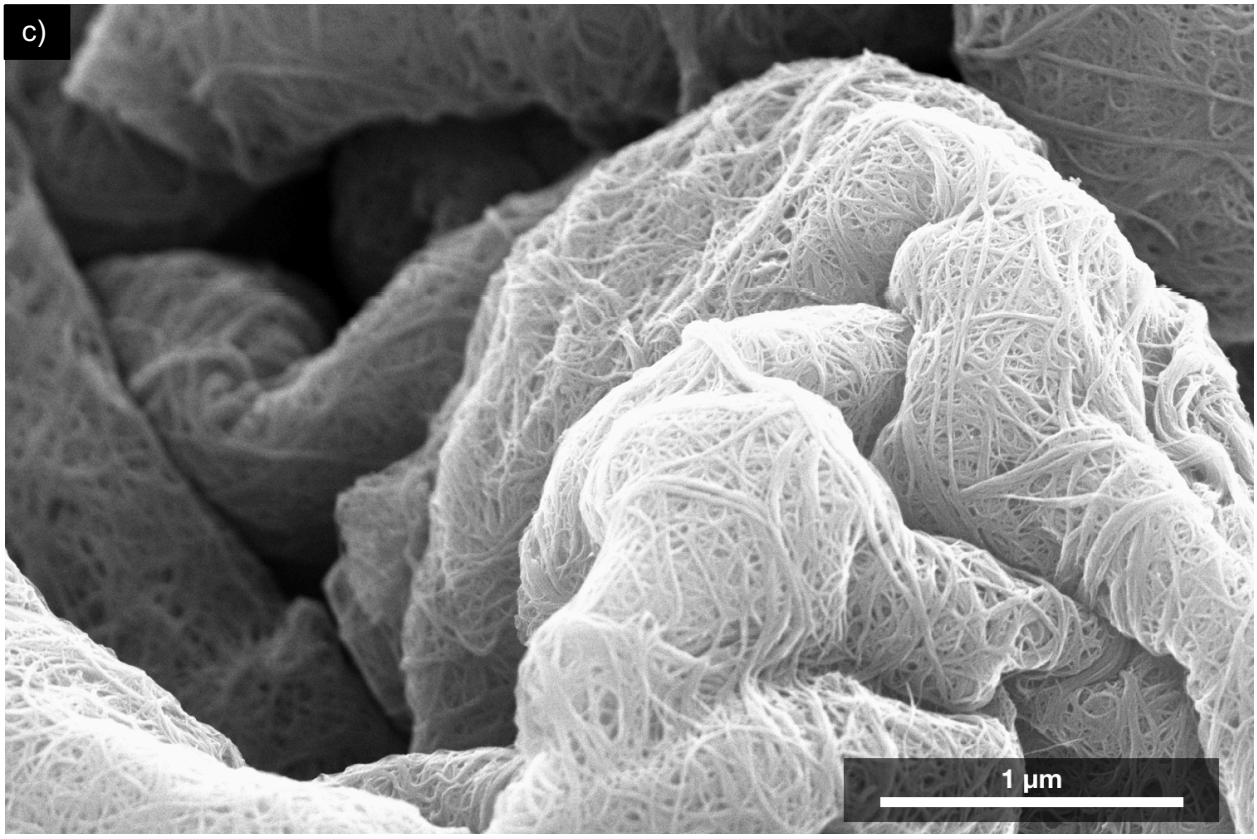

Figure 12. a) SEM of deposited CNT thin film on PS substrate. b) Wrinkled CNT thin film on PS. c) Higher SEM magnification image of wrinkled CNT thin film on PS.

5.3 Results and Discussion

The wrinkled CNT thin film was then characterized by measuring the change in electrical resistance in response to mechanical strain. As shown in Figure 13, it is apparent the wrinkled CNT thin film structures provided large amounts of strain relief relative to the flat CNT thin films (> 60 fold). It is important to note the two distinct regions present in the electromechanical characterization plots of the wrinkled CNT thin film. From 0-400% strain, the normalized change in electrical resistance was 2.5 with a GF of 0.65. From 400-700% strain, the relative change in resistance increased by a factor of 162 with a GF of 48. The increased strain sensitivity in the 400-700% strain region was hypothesized to be due to the cracking and delamination of the wrinkled CNT thin film. Cracking of the wrinkled CNT thin film can be seen in Figure 14.

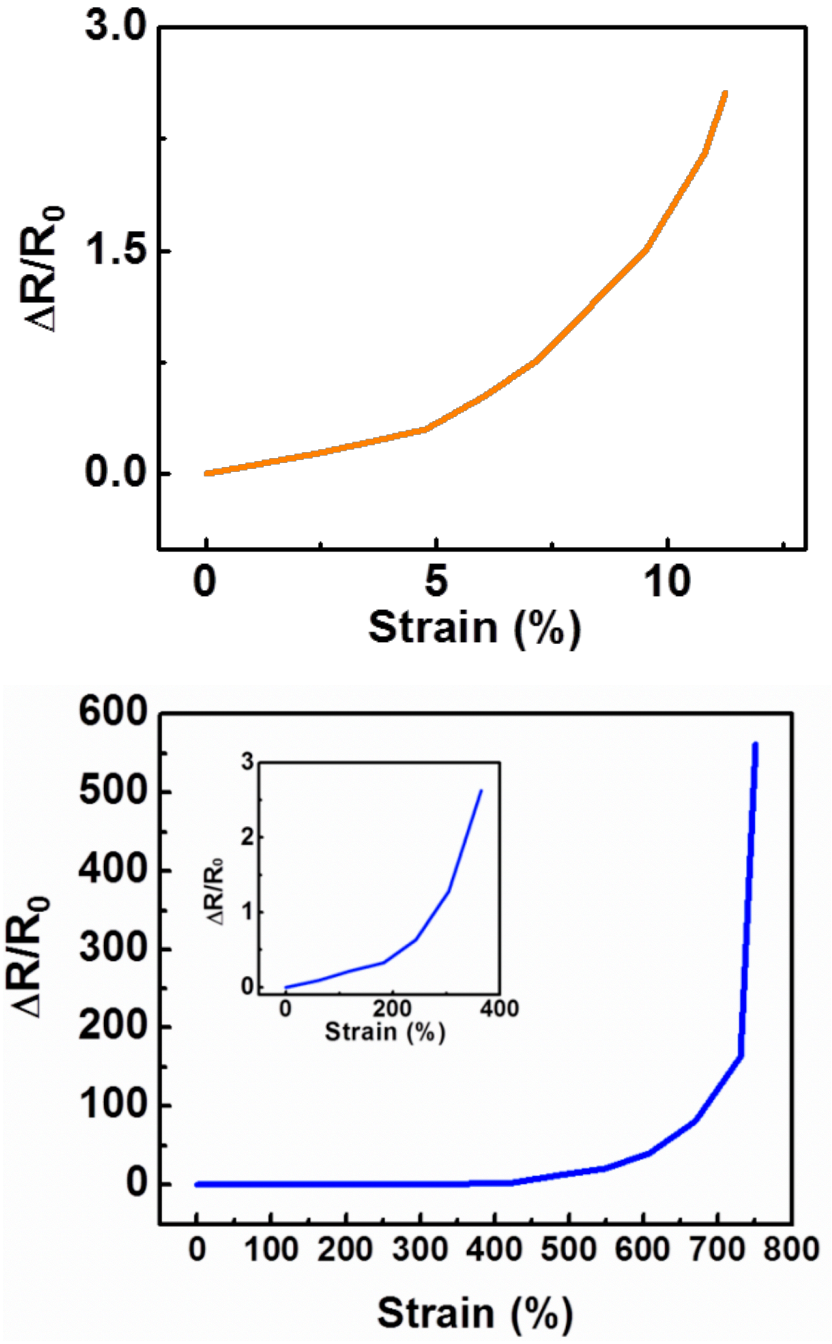

Figure 13. Electromechanical characterization of flat and wrinkled CNT thin film on Ecoflex. Top plot shows a flat CNT thin film only being able to withstand tensile strain of up to 12%. Bottom plot shows wrinkled CNT thin film is able to withstand strains of up to 700%.

In comparison to wrinkled Au thin film, it is very apparent that wrinkled CNT thin films were able to withstand significantly large amounts of tensile strain before electrical failure. As suggested before, the percolating network nature of the CNT thin films provides additional strain relief. Another possibility that wrinkled CNT thin films were able to withstand large amounts of mechanical strain might also be due to the high surface area of the wrinkled CNT thin films. The van der Waal forces may be amplified from the wrinkled structures as well as the surface area of each individual CNT particle which may have improved the interfacial strength between the thin film and substrate.

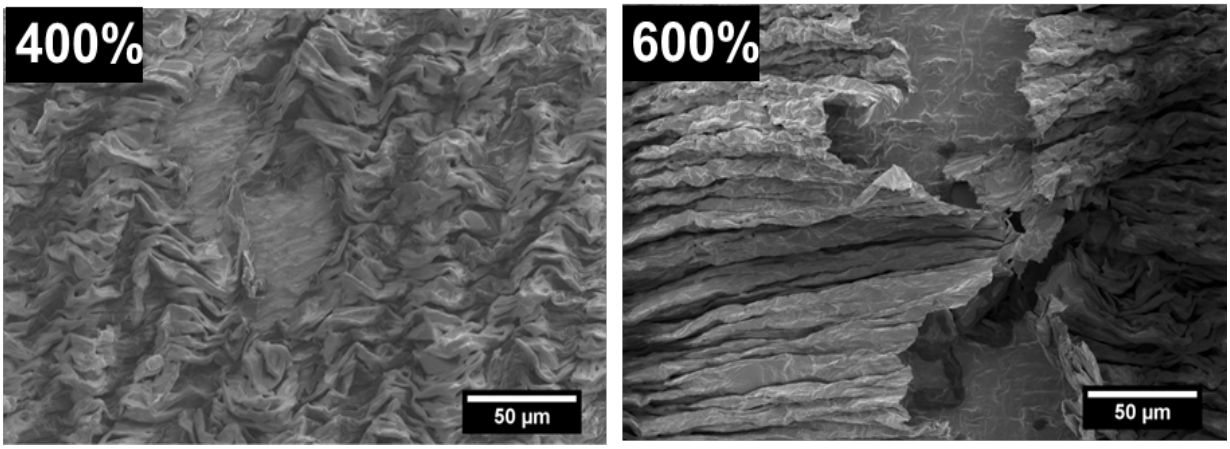

Figure 14. SEM images of wrinkled CNT thin film strained at 400% and 600%.

To test robustness, the wrinkled CNT thin film was then subjected to cyclic strain of up to 300% for 1000 cycles. As seen in the Figure 15, the normalized changed in electrical resistance was approximately 175% which corresponds well with the strain to failure electromechanical plot. As shown in the cyclic strain plot, there was not a significant increase in normalized change in electrical resistance after 1000 cycles of 300% strain.

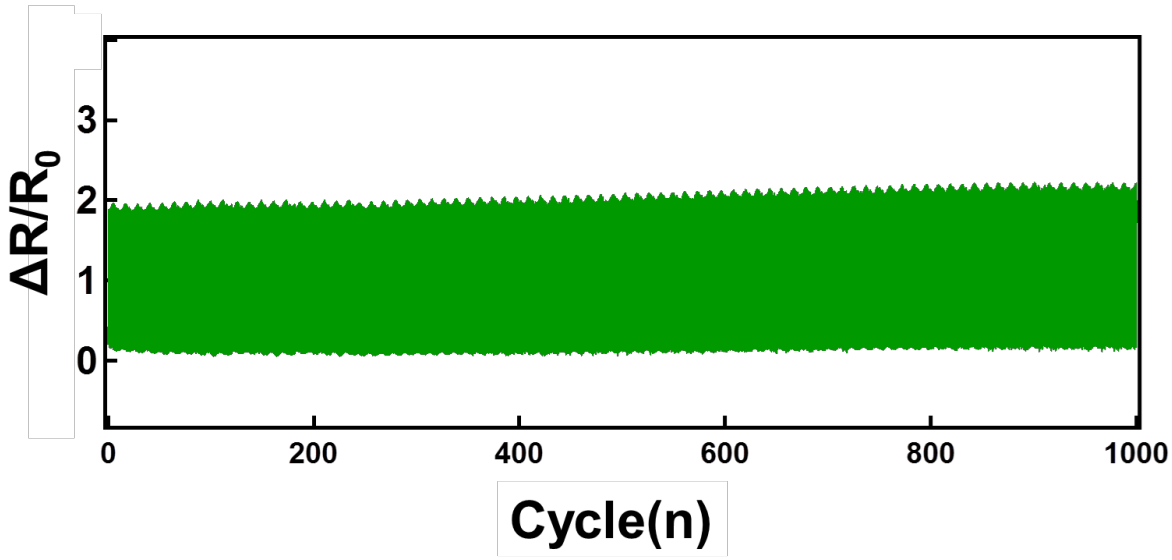

Figure 15. Cyclic strain of wrinkled CNT thin film.

After electromechanical characterization, the wrinkled CNT thin film was used as strain sensors for detecting human motion. The wrinkled CNT thin films were laminated to the body and supported with a stretchable athletic adhesive tape (KT Tape). The sensors were laminated onto the elbow, the knee, and the finger demonstrating human motion detection applications. The joints were bent to various degrees to demonstrate that it is possible to quantify certain degrees of bending in joints. The results of these human motion detection applications are shown in the following figures.

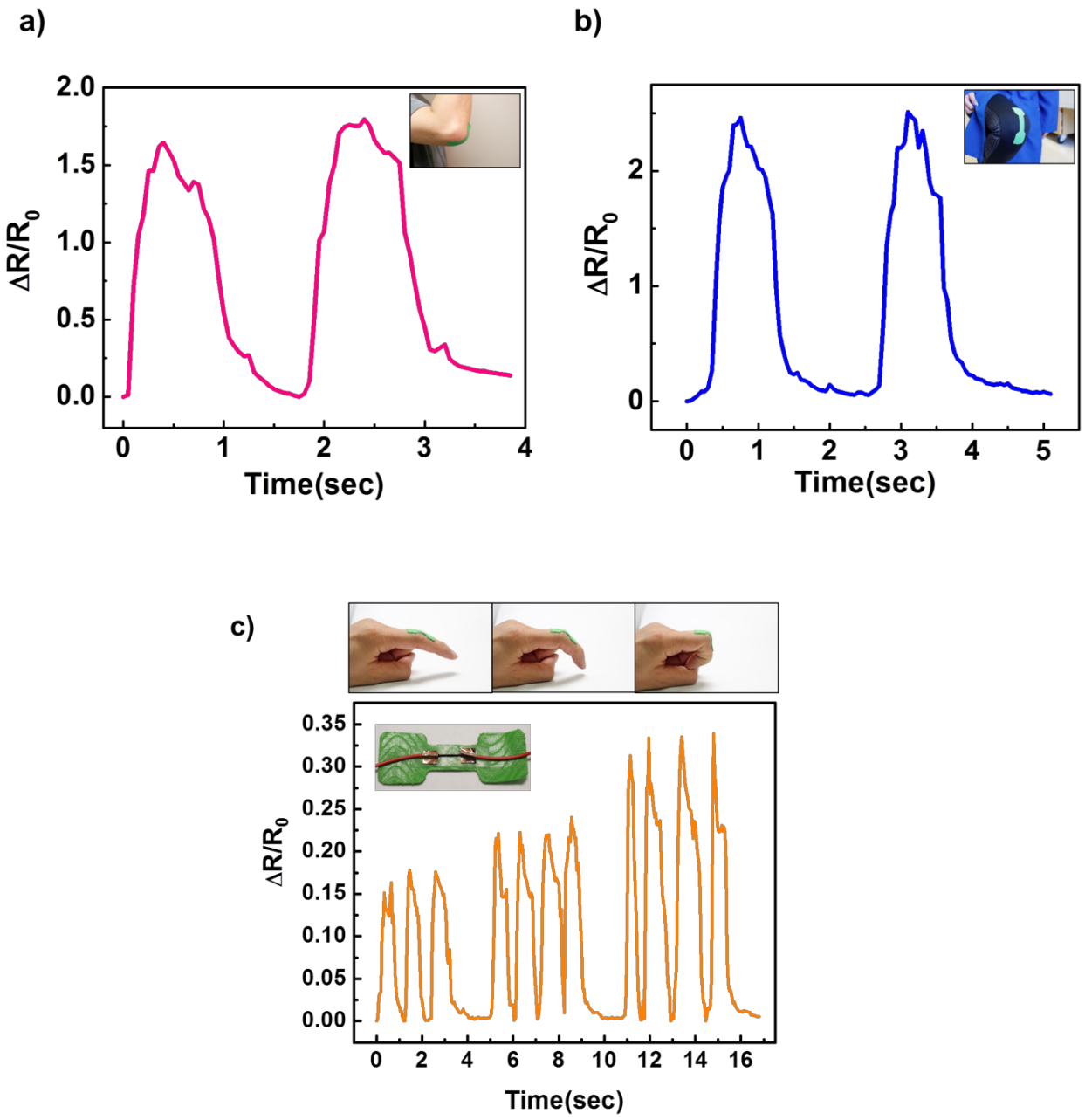

Figure 16. a) Wrinkled CNT thin film sensor laminated on the elbow, b) knee, and c) finger joint.

5.4 Conclusion

In conclusion, the work presented here shows that CNT thin films are compatible with the shrinking fabrication process platform. As a result, it was possible to fabricate highly wrinkled CNT thin films. When these materials were transferred onto a soft silicone elastomer, the wrinkled CNT thin films demonstrated stretchability of up to 700% strain before electrical failure. The hypothesis is that the percolating network present in the CNT thin films provide large amounts of elasticity allowing the wrinkled thin films to withstand strains of up to 700%. Also, the high surface area of each of the CNT nanoparticles may have contributed to an increase in van der Waals interfacial strength between the substrate and the thin film which provides larger amounts of strain delocalization. Finally, these wrinkled CNT thin films were used as strain sensors to detect human motion at various joints including the elbow, knee, and finger.

CHAPTER 6: WRINKLED CARBON NANOTUBE PIEZORESISTIVE PRESSURE SENSORS

6.1 Introduction

In this chapter, I will discuss fabricating piezoresistive pressure sensor with wrinkled CNT thin films. As shown previously, wrinkled CNT thin films displayed elastic properties capable of withstanding large amounts of strain. In piezoresistive sensors, these wrinkled CNT thin films can be placed against each other to create an electrically conductive pathway between the electrodes. As these electrodes are compressed against each other, more electrical contact points are made reducing the electrical resistance between the electrodes. By placing electrodes with different wrinkled morphologies (1D and 2D wrinkled structures) pressure sensitivities increased up to 12800-fold with quick response times of 20ms were achieved. Here I demonstrate wearable applications using these wrinkled CNT thin films for piezoresistive sensors including radial pulse and voice characterization.

6.2 Experimental Methods

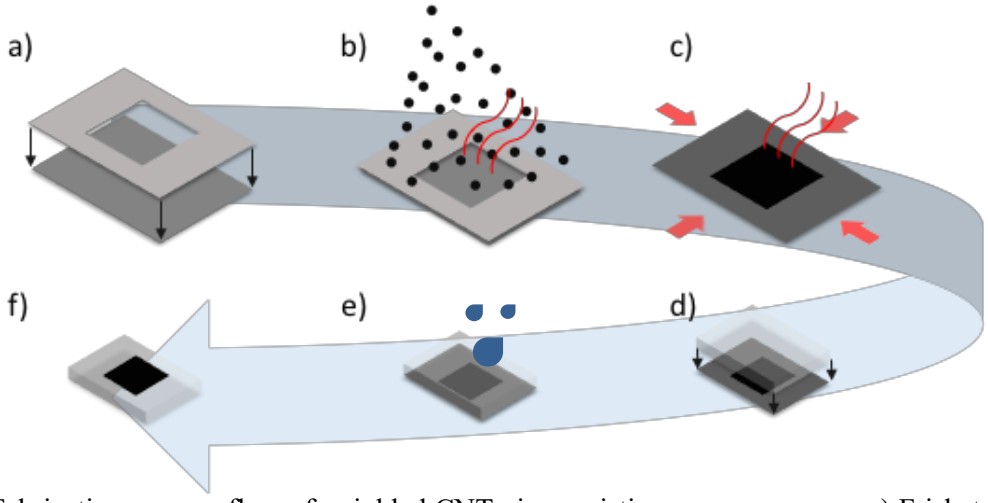

Figure 17. Fabrication process flow of wrinkled CNT piezoresistive pressure sensor. a) Frisket film mask first is placed on PS substrate. b) CNT dispersed solution is deposited onto a heated PS substrate. c) Thermally induced shrinking process. d) Silicone elastomer cured on the wrinkled CNT thin film. e) Organic solvent transfer bath. f) Final wrinkled CNT thin film on silicone elastomer.

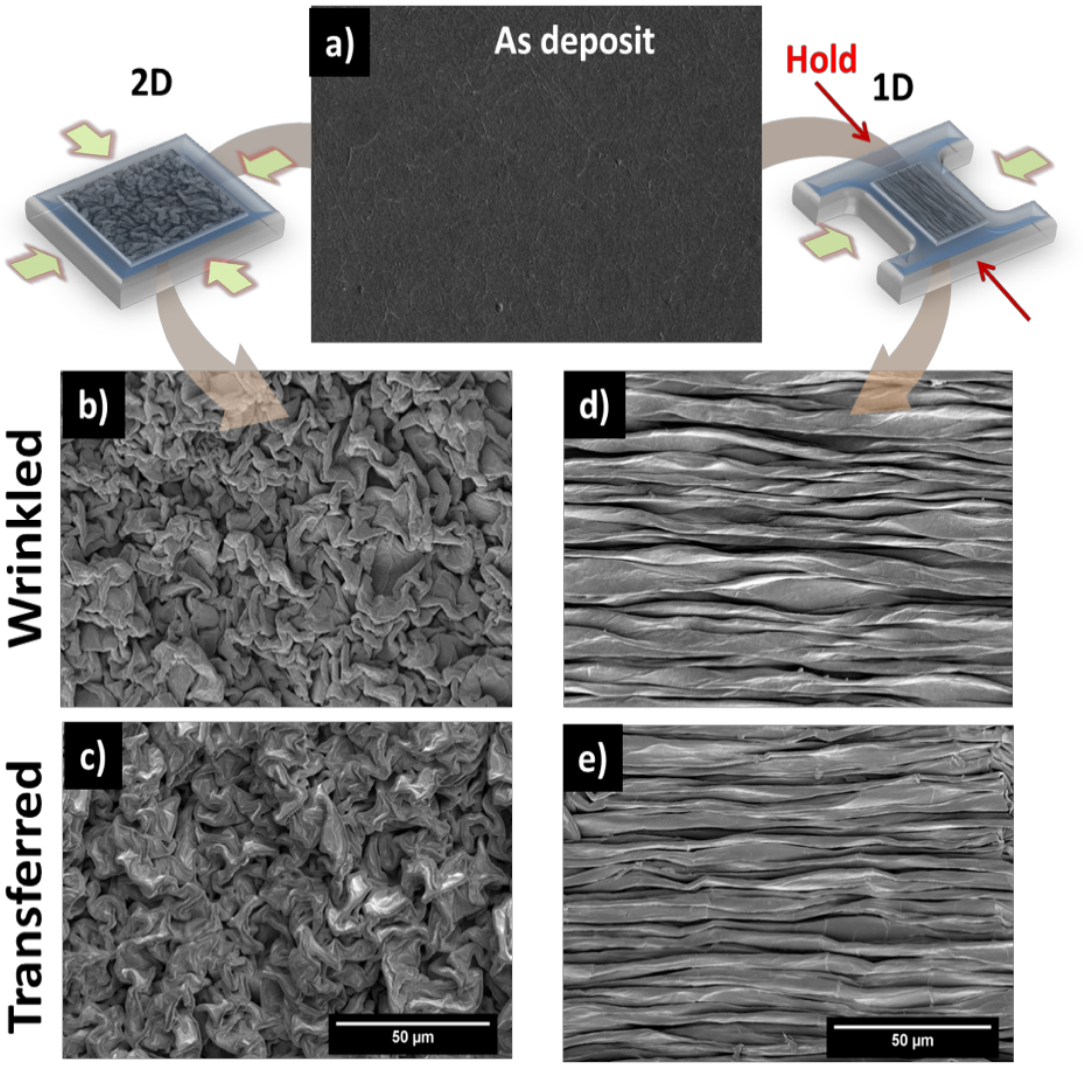

Figure 18. a) CNT thin film deposited on PS substrate. b) Biaxially thermally induced shrunk wrinkled CNT thin film and c) transferred onto Ecoflex substrate. d) Uniaxially thermally induced shrunk wrinkled CNT thin film and e) transferred onto Ecoflex. Scale bars are 50 µm.

The fabrication process flow was adopted from the previous chapter with some differences. In this case, two transferred electrodes were coupled face to face to create an electrically conductive pathway between the two electrodes. In addition, different wrinkle morphologies were obtained by restricting shrinking of different axes. This was achieved by clamping down two ends during the thermally induced shrinking process.

Scanning electron microscope (SEM) was used to image the wrinkled CNT morphologies as seen in Figure 18. Figure 18bc illustrates CNT thin films shrunk biaxially (2D). Figure 18de

illustrates CNT thin films when shrunk uniaxially. As seen in figure 18de, the wrinkled structures were orthogonally aligned to the direction of shrinking (1D). This was accomplished by clamping two ends during the thermally induced shrinking process.

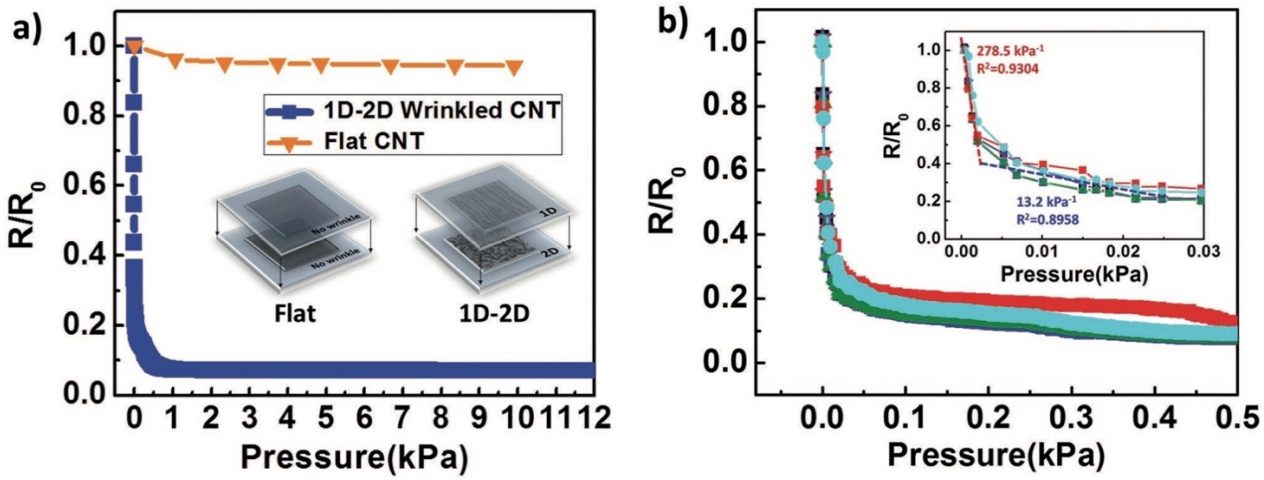

Figure 19. a) Pressure sensitivity for 1D-2D wrinkled CNT thin films compared to flat CNT thin films. b) Pressure sensitivity of six different sensors.

6.3 Wrinkled CNT Pressure Sensor Characterization

Piezoresistive pressure sensitivity is defined as the change in electrical resistance per applied pressure. When pressure is applied to the piezoresistive sensor, the electrical resistance between the electrodes decrease due to the increased contact points. Therefore, pressure sensitivities are related to increasing electrical contact points due to applied pressure. This is shown by Equation 2 rewritten here:

$$S = \frac{R/R_O}{\Delta P} \tag{2}$$

where R is the resistance, R_o is the initial resistance, and P is pressure. The electromechanical response of the 1D-2D piezoresistive sensor can be seen in Figure 19. Pressure sensitivities for 1D-2D were measured to be around 278.5 kPa^{-1} from 0-2 Pa. However, from 2-25 Pa, the pressure sensitivity dropped to 13.2 kPa^{-1}. The decrease in pressure sensitivity was due to the initial compression of a majority of the wrinkled structures. Having wrinkled CNT structures

incorporated into the electrodes improved pressure sensitivities of upwards of 12,800 times, where the flat CNT thin film electrodes exhibited pressure sensitivities of approximately 0.022 kPa^{-1}.

Previously I have shown that these wrinkled CNT thin films can deform to large amounts of strain. Similarly, these wrinkled CNT thin film electrodes can elastically deform when normal pressures are applied. The compression of these wrinkled electrodes led to rapid increase in the number of electrical contact points contributing to higher pressure sensitivities. However, after these structures were completely compressed, the pressure sensitivity decreased behaving similarly to flat CNT electrodes.

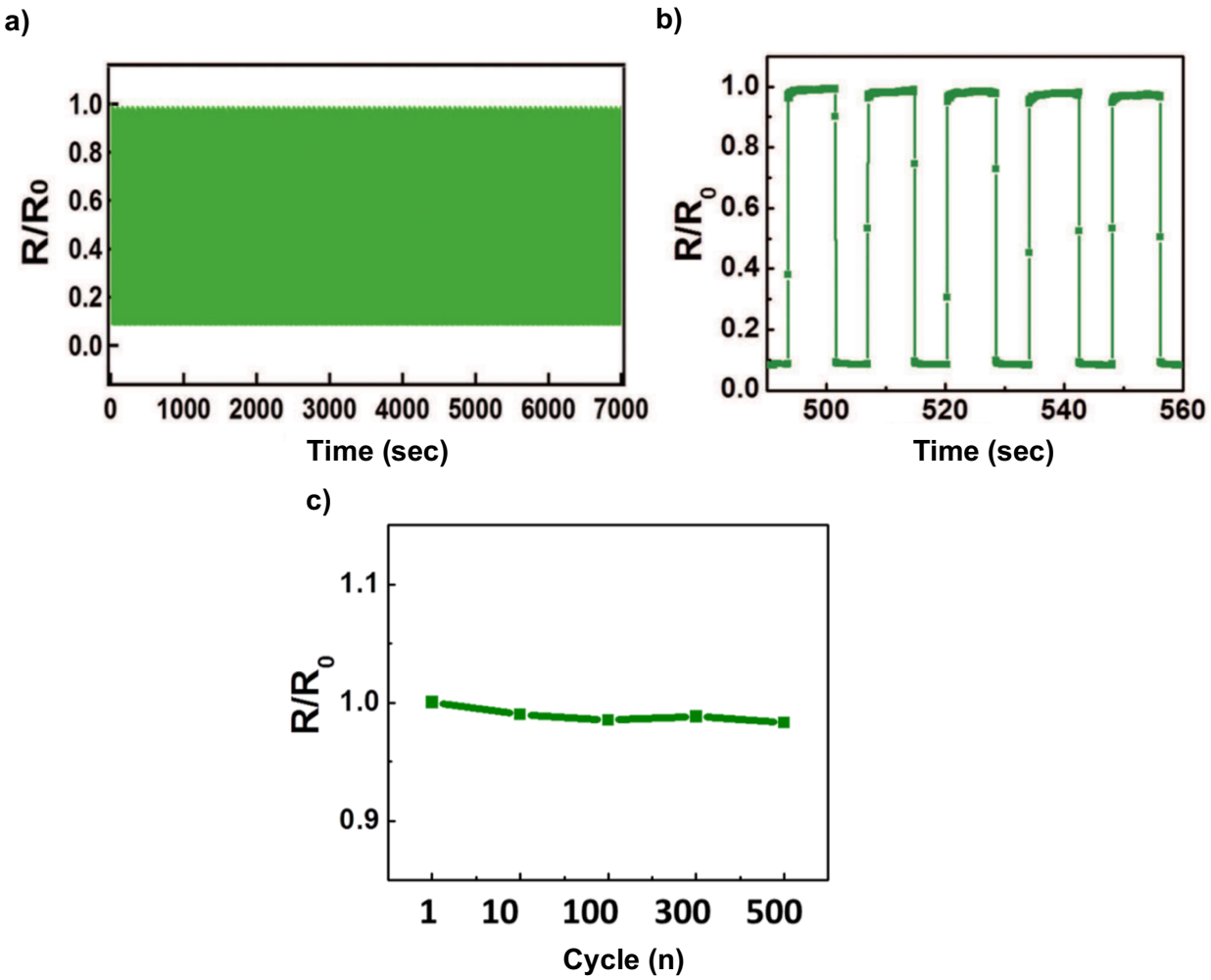

Figure 20. a) 500 cycles of 0.5 kPa load b) Inset of 5 cycles during cyclic loading. c) Relative resistance change at a given number of cycles *n*.

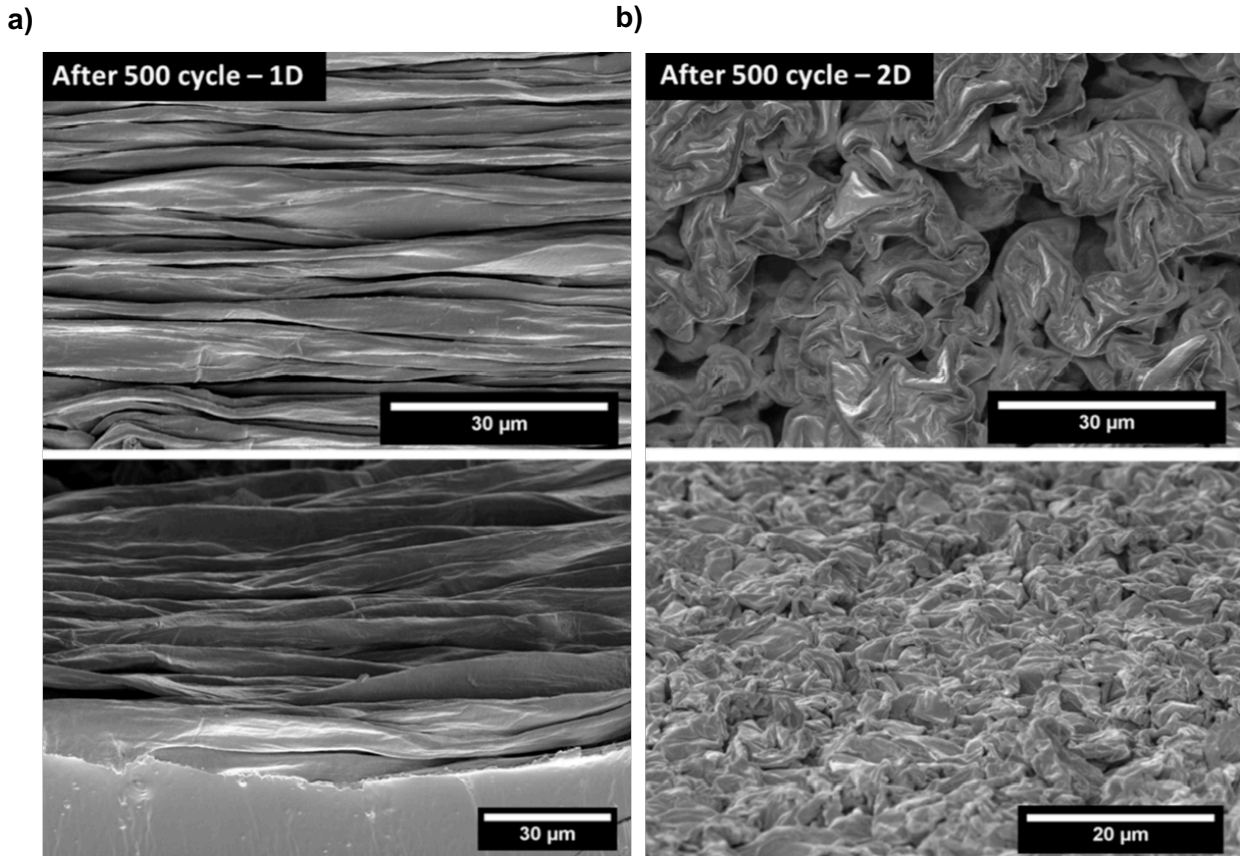

Figure 21. a) 1D wrinkles and b) 2D wrinkled CNT thin films after 500 cycles of 0.5 kPa.

Sensor robustness was measured by applying a cyclic load at 0.5 kPa. Figure 20 illustrates the sensors electromechanical response to 500 cycles of 0.5 kPa. The relative change in resistance was minimal after 500 cycles as shown by Figure 20c which illustrates the relative change in resistance after n cycles. The standard deviation of the relative change in resistance was approximately 0.012 suggesting robustness to cyclic loads. Furthermore, Figure 21 illustrates that the wrinkled CNT thin films maintained their wrinkle morphologies after cyclic loading.

6.4 Different Wrinkle Combinations

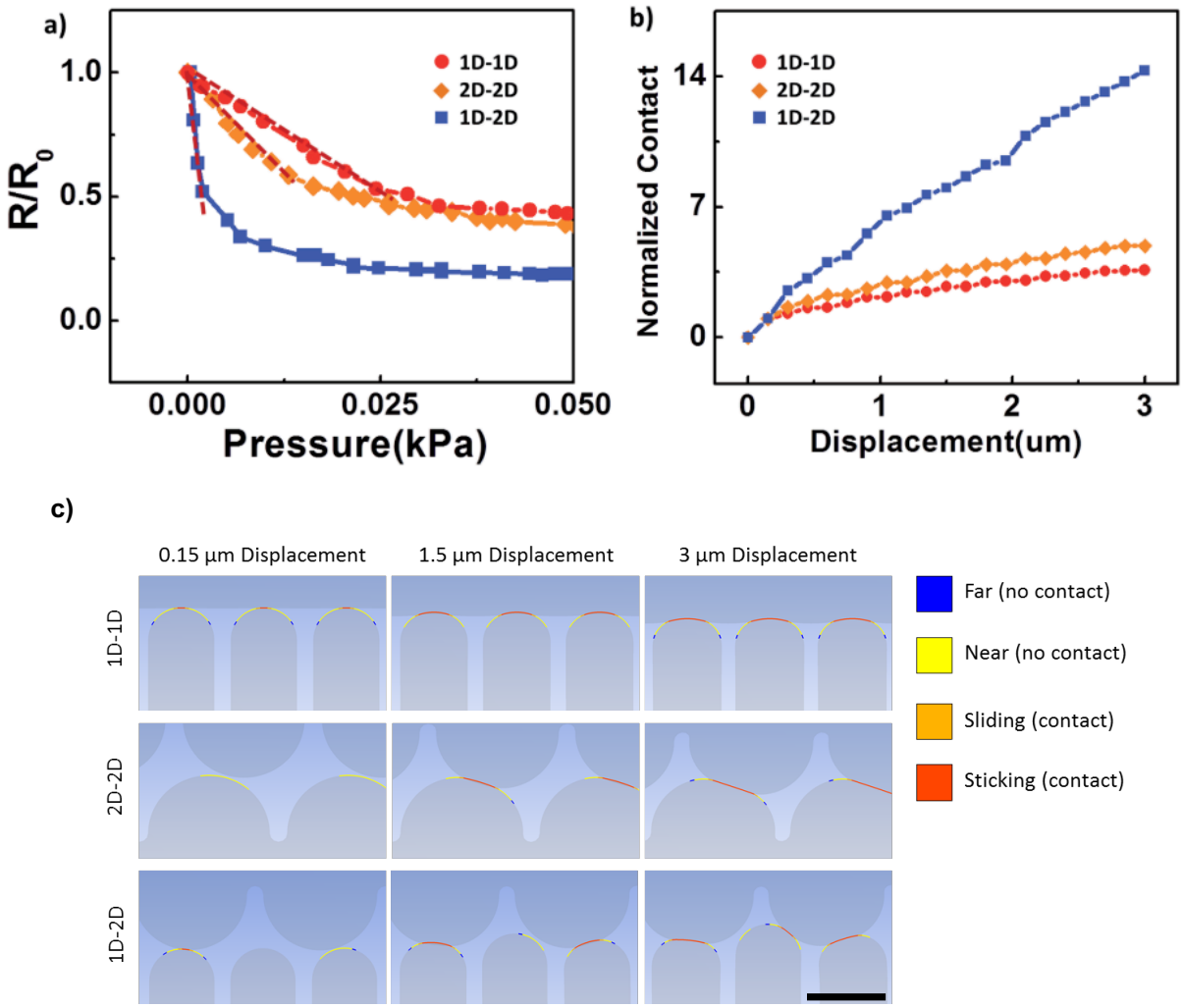

Figure 22. a) Electromechanical response of different wrinkled morphology combinations. b) FEA of normalized contact of different wrinkled morphology combinations. c) FEA illustrating increasing contact per displacement for different wrinkle morphologies.

The electromechanical response of different wrinkled combinations were explored: 1D-1D, 2D-2D, and 1D-2D. The results from Figure 22a suggest that the mismatched wrinkled morphologies contributed to higher pressure sensitivities. Finite element analysis (FEA) was used to further investigate how having mismatched wrinkle morphologies contributed to higher pressure sensitivities. As seen in Figure 22b, the FEA results indicate that the 1D-2D combination provides a higher dynamic range of normalized contact between the electrodes. Figure 22c, further illustrates the varying contacts between different wrinkle morphologies. Therefore, it is possible to incorporate mismatched morphologies in piezoresistive sensors to improve pressure sensitivities.

6.5 Voice and Pulsatile Blood Flow Detection

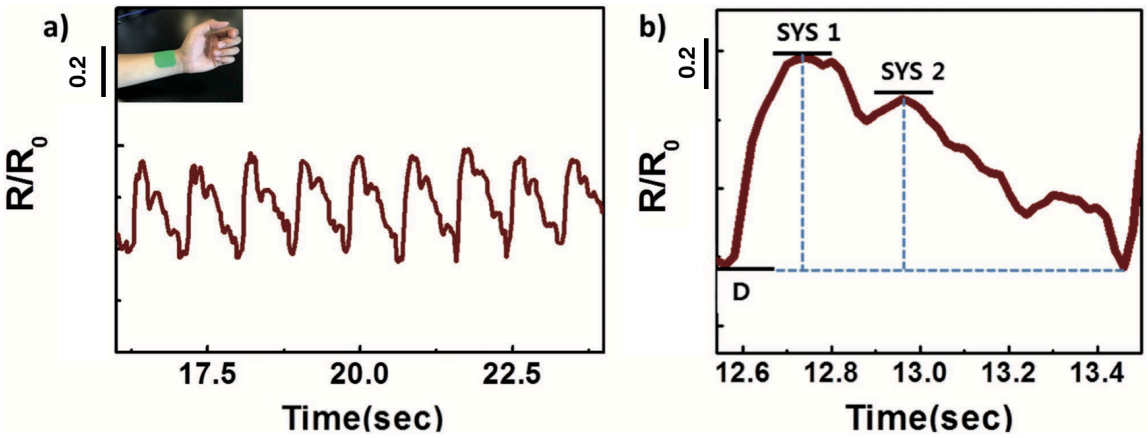

Figure 23. a) Radial pulse detection over several cardiac cycles. b) Inset of one pulse waveform illustrating the detection of the systolic peak 'SYS 1', second systolic peak 'SYS 2', and diastolic 'D'.

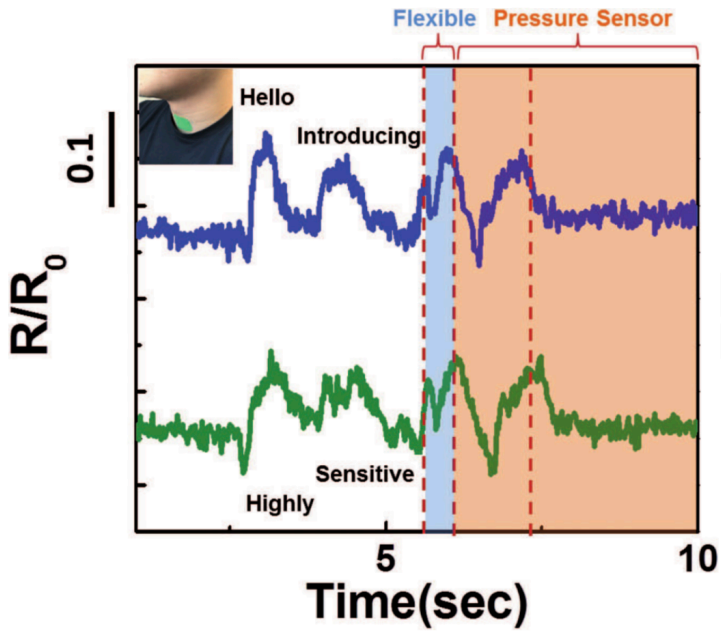

Figure 24. Voice detection when sensor is attached to the throat. Unique waveforms were detected for different phrases as the throat was moving while speaking different phrases.

Demonstrations of radial pulse and voice detections are shown in Figure 23 and 24. For the radial pulse application, the flexible sensor was placed on the radial artery and secured with tape. The radial pulse was then measured for a few cardiac cycles. Figure 23 shows that the piezoresistive sensor is able to detect the unique features of a pulse waveform including the

diastolic, systolic, and the second systolic peak. The signal fidelity appears noisy which can possibly be attributed to the unstable contact between the electrodes.

The sensor was also placed on the throat to demonstrate voice detection applications. Note that the signal was acquired due to the movement of the throat as opposed to the vibrations of the throat. Figure 24 illustrates two unique phrases spoken with the pressure sensor taped to the throat of the subject. The unique waveforms for different phrases suggest the possibility to detect words when a pressure sensor is placed on the neck, which may be practical in communication applications.

6.6 Conclusion

In conclusion, piezoresistive pressure sensors were fabricated using wrinkled CNT thin films. By placing these electrodes face to face an electrical conductive pathway was made between the electrodes. High pressure sensitivities were achieved by incorporating different wrinkled morphologies (1D and 2D) in comparison to low pressure sensitivities for flat electrodes. These pressure sensors exhibited robustness of 500 cycles showing little changes in wrinkle morphologies. Preliminary, FEA shows that having mismatched wrinkle morphologies contribute to larger changes in the normalized contact between the electrodes. Finally, radial pulse and voice applications were shown using the piezoresistive pressure sensors.

CHAPTER 7: FLEXIBLE PIEZOCAPACITIVE PRESSURE SENSORS FOR NONINVASIVE BLOOD PRESSURE MONITORING

7.1 Introduction

Stretchable wearable electronics have received considerable attention due to a wide variety of applications including continuous monitoring of human physiological signals.[9,28,32,73,105–109] This includes continuous measurements of radial pulsatile blood flow located on the wrist.[4,7,10,58,110–112] In order to detect this radial artery waveform accurately, pressure sensors that are conformal, highly sensitive, reproducible, and have quick response times are needed.

Arterial blood flow propagates throughout the body and can be palpated at many regions of the body such as at the radial artery. Pulsatile blood flow at these regions have unique waveforms that contain important indices regarding a person's cardiovascular health such as systolic, diastolic, pulse pressures, and augmentation index.[112–116] Therefore, there are opportunities to be able to continuously monitor a person's cardiovascular health. One such way to detect and characterize pulsatile blood flow is to use mechanical pressure sensors to measure the amount of pressure being exerted by these arteries.

Capacitive pressure sensors have been characterized with quick response times, and linear electromechanical responses.[24,63,95,117] Typically, soft capacitive pressure sensors are comprised of two parallel electrodes separated by an elastomeric dielectric layer. As pressure is applied, the dielectric layer becomes compressed leading to an increase in capacitance. In comparison to piezoresistive sensors, capacitive pressures are characterized with low pressure sensitivities due to the small deformation of the dielectric layer. Therefore, there is a need to improve the pressure sensitivities of capacitive pressure sensors to leverage the desirable characteristics of capacitive sensors for sensing human biometric signals.

Pressure sensitivity in capacitive pressure sensors are defined by:

$$S = \frac{\Delta C / C_o}{P} \tag{7}$$

where P is pressure, C is capacitance, and C_o is the initial capacitance. To improve pressure sensitivities, microstructured dielectric layers have been implemented. For example, Mannsfeld et al. molded micropyramidal structures into PDMS dielectric layers which improved pressure sensitivities by five times in pressure regions <2kPa. Microstructured dielectric layers are advantageous because they reduce overall mechanical stiffness and also creates a dynamic dielectric permittivity as discussed earlier.[28,95,118,119]

In this work, wrinkled Au thin films (wAu) were used to fabricate flexible capacitive pressure sensors. In previous studies, I have demonstrated that thermoplastics (i.e. polystyrene) can be used to create highly wrinkled micro/nanoscaled structures in thin films via a heat induced shrinking process. These wrinkled structures have shown to provide strain relief allowing metallic thin films to withstand strains of up to 200%.[61] In addition, microstructures are molded to create airgaps to reduce the elastic resistance of the dielectric layer and also to create a dynamic dielectric permittivity. Herein I introduce preliminary studies that indicate wearable capacitive pressure sensors can capture absolute blood pressure over a period of time by correlating with an FDA approved finger cuff hemodynamic device that continuously measures blood pressure.

7.2 Experimental Methods

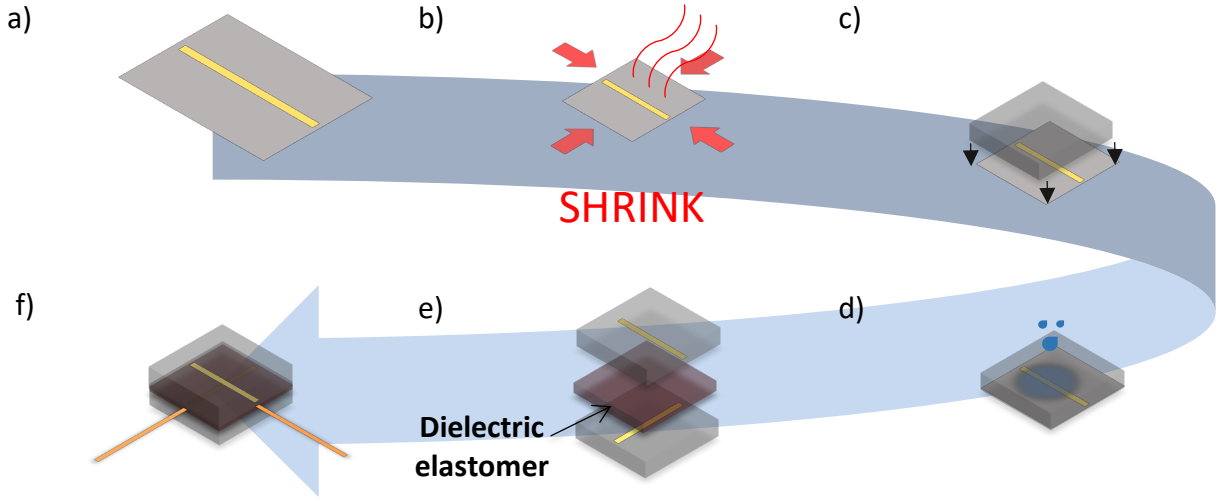

Figure 25. Fabrication process flow of capacitive pressure sensors. During the patterning step, laser is etched into the PS to create microridge structures. a) Au is sputtered through a shadow mask. b) Sample is heated passed glass transition temperature to induce shrinking of shape memory polymer. c) Silicone elastomer is then bonded to the wrinkled Au thin film and then d) transferred using an organic solvent bath. d) Dielectric elastomer is plasma bonded between two electrode layers. f) Interconnections are added to complete sensor fabrication.

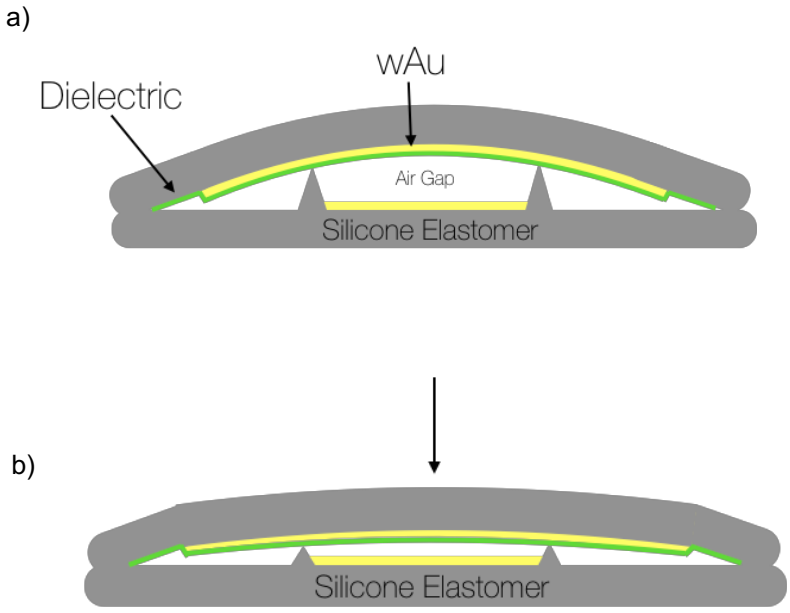

Figure 26. Illustration of cross section of capacitive pressure sensor. a) Schematic of pressure sensor prior to load and b) after load.

Capacitive pressure sensors are fabricated using the heat induced shrinking fabrication process outlined in this dissertation. Shadow mask (Frisket film, Grafix Arts) was first placed on a PS substrate. Laser cutter (VLS 2.30, Versa Laser) was used to pattern the geometry of the electrode. In addition, laser cutting was used to etch microstructures into the PS substrate. The depth of the etch can be modified by adjusting the power and speed settings of the laser cutter. Afterwards, Au thin film was sputtered through a shadow mask onto a PS substrate. The sample was subsequently heated passed the PS glass transition temperature to induce biaxial shrinking consequently forming highly wrinkled structures in the Au thin film. These wrinkled Au thin films were then treated with MPTMS and spun coat with pre-cured PDMS. As discussed earlier, the MPTMS treatment allows for a chemical bond between the elastomer and Au thin film. During the spin coating process, PDMS also molded the etched features which would create microstructured ridges. When The wrinkled Au thin film was then transferred onto PDMS by dissolving away the PS substrate in an acetone bath followed by a toluene rinse step. Interconnection wires were then added to the transferred wrinkled Au electrodes. On one layer, Ecoflex was plasma bonded to the electrode substrate with no microstructures. Ecoflex cannot plasma bond directly to another siloxane material. In order to achieve Ecoflex bonding to PDMS, Ecoflex was first cured on a separate PDMS layer. Afterwards, the electrode substrate and the Ecoflex layer was plasma treated and subsequently bonded. The PDMS layer the Ecoflex was cured on was then removed. The chemistry that allows the Ecoflex to plasma bond to PDMS is unclear and requires separate investigation. Afterwards, the Ecoflex surface and the surface of the counter wrinkled Au electrode were treated with air plasma (Plasma Etch, 50 Watts, 200 mTorr, 40 seconds) and bonded together.

Pressure sensor characterization: Force gauge (Series 5 Mark-10) was used to measure the amount of pressure applied to the sensor. Capacitance measurements were taken with an LCR meter (Keysight E4890A, 300 kHz, 1 V). Fiber glass force probe tip with a 6mm diameter was

used for electromechanical tests. Fiber glass force probe tip was used to reduce as much capacitance fringe interference as possible.

Radial Pulse Detection and Signal Processing: Sensor was placed directly over the radial artery located on the wrist. A stiff substrate was added on top of the pressure sensor to provide mechanical support. Subjects were told to stay still during these measurements. Continuous blood pressure measurements were taken with a finger cuff hemodynamic device (Clearsight, Edwards Lifesciences) simultaneously. Accelerometer and gyroscope (BioStamp RC, MC10) data was also gathered simultaneously to measure any possible movements during the measurements. Matlab was used to process the time series signal from the pressure sensor, finger cuff hemodynamic device, accelerometer, and gyroscope devices. Afterwards, systolic and diastolic peaks of the pressure sensor signal and the hemodynamic device signal were measured.

7.3 Results and Discussion

The pressure sensitivities of the capacitive pressure sensors were characterized using a force gauge while simultaneously measuring capacitance. Figure 28 displays the electromechanical response of five capacitive pressure sensors with a surface area overlap of $2x2mm^2$. As shown in the figure, there seems to be some variation in pressure sensitivities. The variation could be attributed to manual handling of the sensors during fabrication, thickness variations of the substrates during the spin coating process, as well as the variation of the microstructured ridge sizes due to the inconsistency of the laser cutter etch. By carefully controlling each fabrication step, it may be possible to reduce the variations of pressure sensitivities from sensor to sensor. As seen in the pressure sensitivity curves, regions from. 0-10 kPa show relative reproducibility in pressure sensitivities across five different capacitive pressure sensors ($0.1448 \pm 0.0314\ kPa^{-1}$). Reproducibility can further be improved by carefully controlling the fabrication processes (i.e. ridge molding process and spin coating thickness

tolerance). Nevertheless, pressure sensitivity is sufficiently high in the physiological range from 0-10 kPa for detecting radial pulse.

The height profile of the laser etch in the PS can be seen in Figure 27. The initial height of the etch was approximately 30 μm deep and 30 μm wide. As seen in Figure 27a, the heat from the laser re-casted the PS material along the edge of the laser cut which. After shrinking the depth of the etch increased to approximately 85-90 μm deep and shrunk to approximately 10 μm wide. This deepening and thinning of the etch has been reported, but the phenomenon is still not well understood.[120] Figure 27b shows the final molded microridge structure with a height of approximately 85 μm and approximately 20 μm wide. The microridge was responsible for the air gaps between the dielectric layer and the electrode. This reduced the elastic resistance in the dielectric. The airgaps also provided a dynamic dielectric permittivity which contributed to higher pressure sensitivities as seen in the following pressure sensitivity plots in Figure 28.

In comparison to electrodes with micro-ridges, a capacitive sensor with no micro-ridges displayed approximately three times less pressure sensitivity as seen in Figure 29. From 0-10 kPa, the 0.042 kPa^{-1} was measured for one sensor as shown in Figure 29b. It is worth noting that the pressure sensitivity is not linear from 0-10 kPa. This is due to the compression of the dielectric material (Ecoflex 0030) and the elastomeric substrate (PDMS), which are nonlinear elastic materials. In contrast to sensors with airgaps, the deformation of the sample with no microridges occurred primarily in the substrate material. Whereas in the sensors with microridges, the deformation occurs in the air gap. Therefore, there is evidence that the microridges contribute to higher pressure sensitivities and can be implemented as a strategy for improving pressure sensitivities in capacitive pressure sensors. Clever designs can further be implemented to find the optimal pressure sensitivities for pressure sensitivities. Ridged structures can also be implemented

to modify the linearity of the electromechanical response to be more similar to that of human skin response to touch.

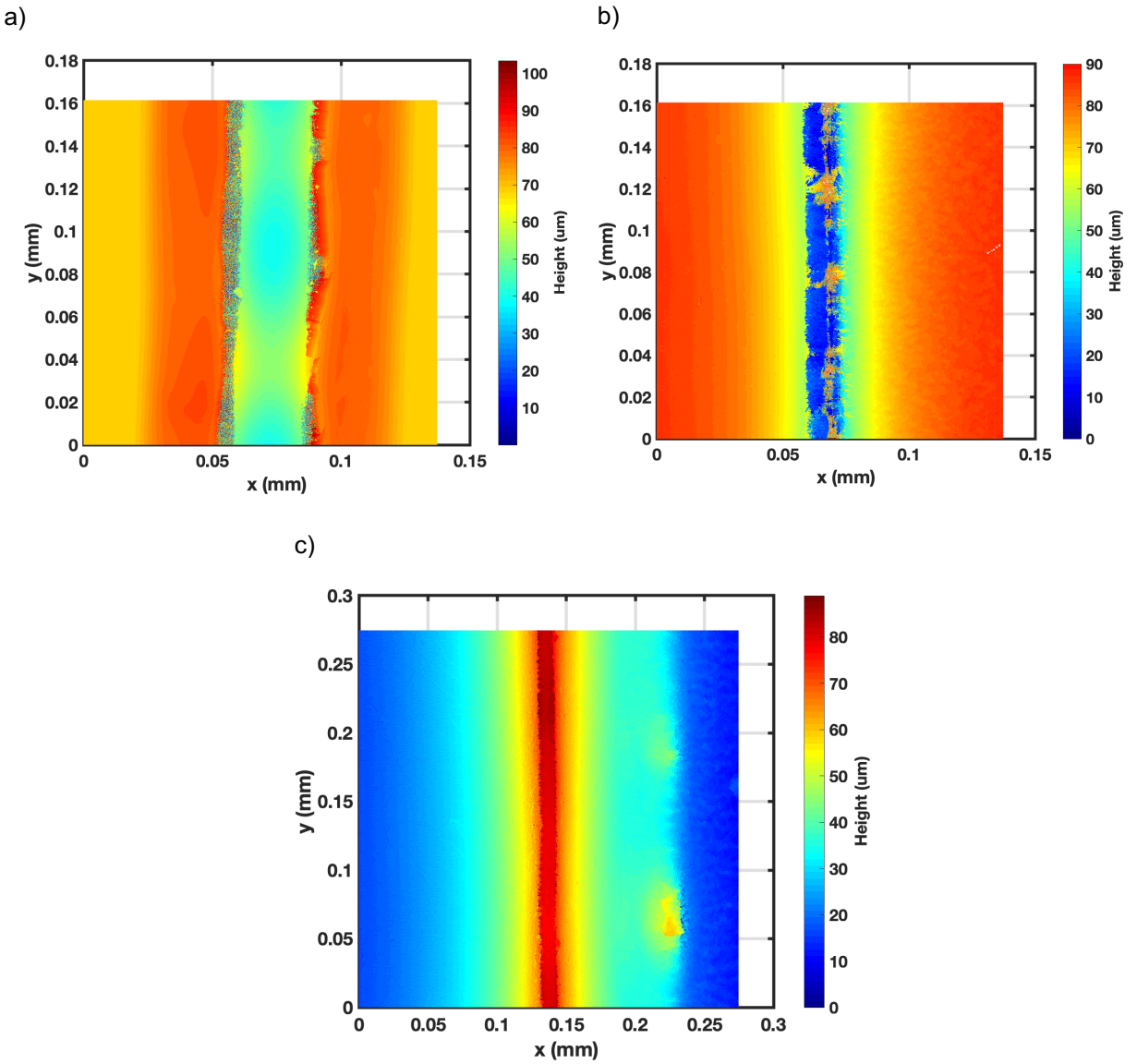

Figure 27. a) PS etch prior to shrinking. b) PS etched profile after shrinking. c) PDMS molded microridge. Height profile was measured with a laser confocal microscope.

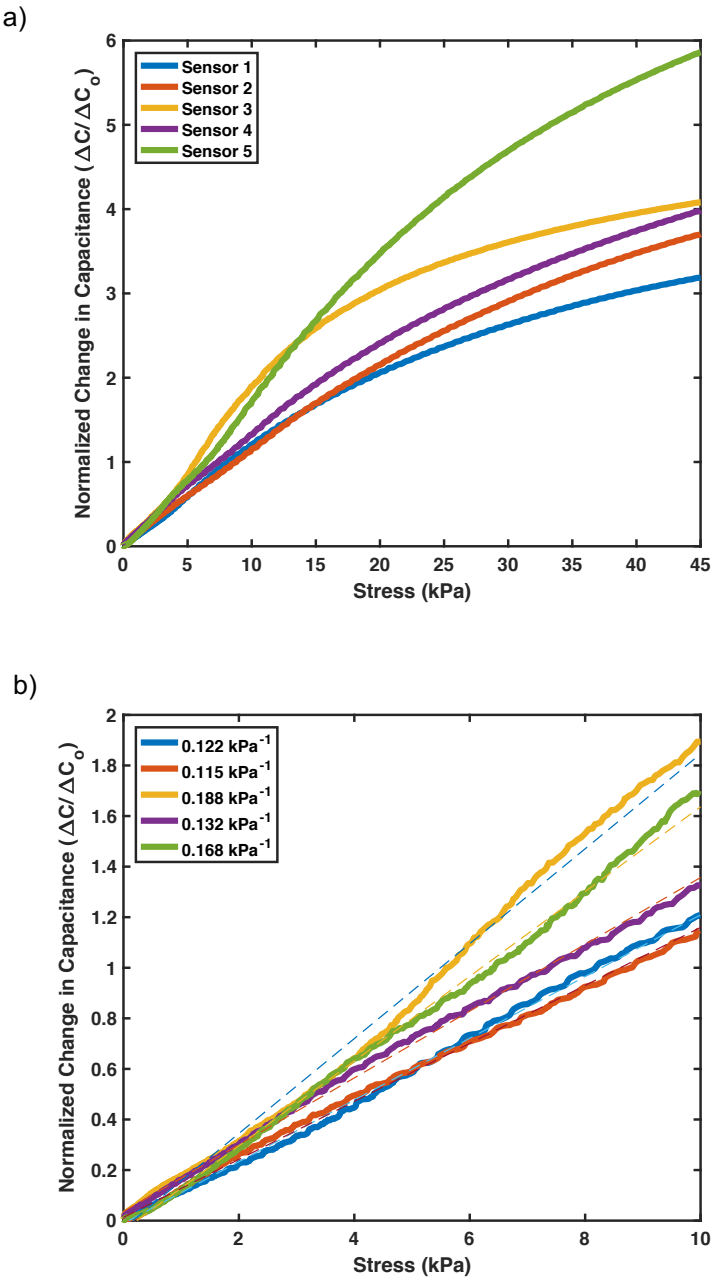

Figure 28. a) Pressure sensitivity curve of five capacitive pressure sensors. b) Inset of pressure sensitivity curves from 0-10 kPa with respective pressure sensitivity measurements.

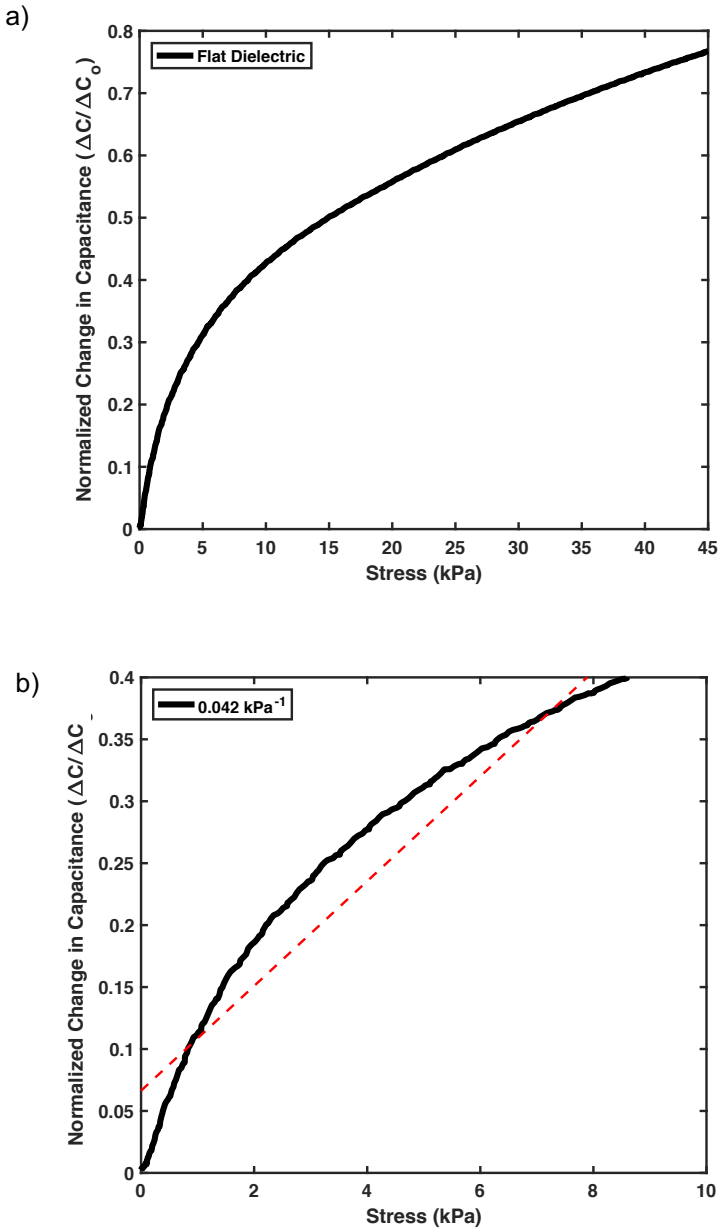

Figure 29.a) Pressure sensitivity for sensor with no microridges. b) Pressure sensitivity from 0-10 kPa. Note the pressure sensitivity is not linear within this region.

Response time was measured by applying a force and releasing. Approximately 1.5 N was applied (~53 kPa) to the sensor. As seen in Figure 30, the response time of the sensor could not be properly measured due to the insufficient sampling rate frequency (50 Hz sampling rate) as well as the ability to appy loads quickly. To study the response time, the sensor was quickly tapped once. This response can be seen in Figure 31.

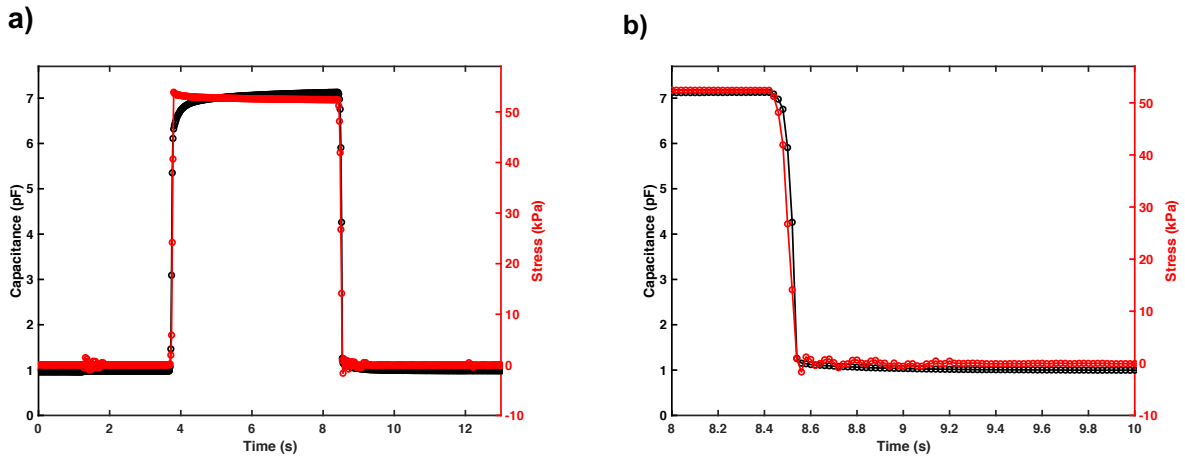

Figure 30. a) Electromechanical response of the capacitive pressure upon applying pressure using force gauge. b) Inset of the electromechanical response. Insufficient sampling rate and ability to load makes it difficult to accurately measure response time.

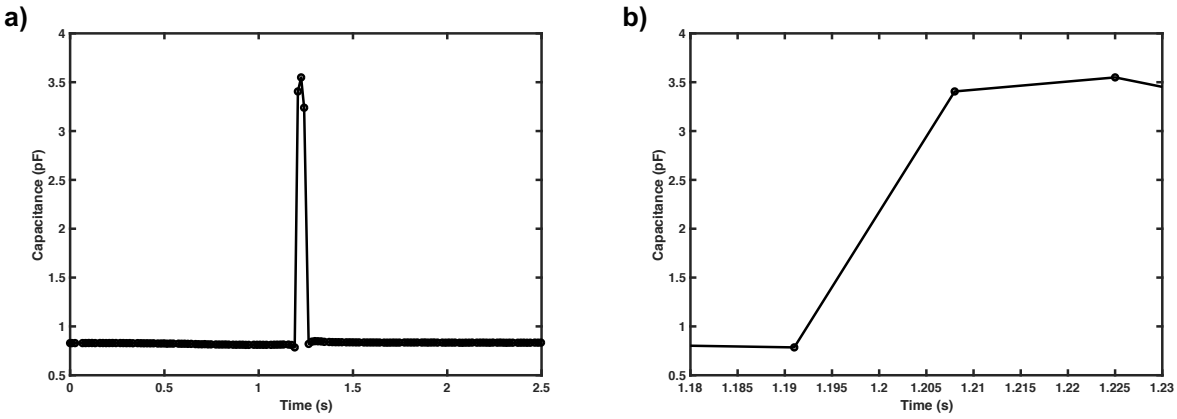

Figure 31. a) Quick tapping response of the capacitive pressure sensor. b) Inset of the quick tap response.

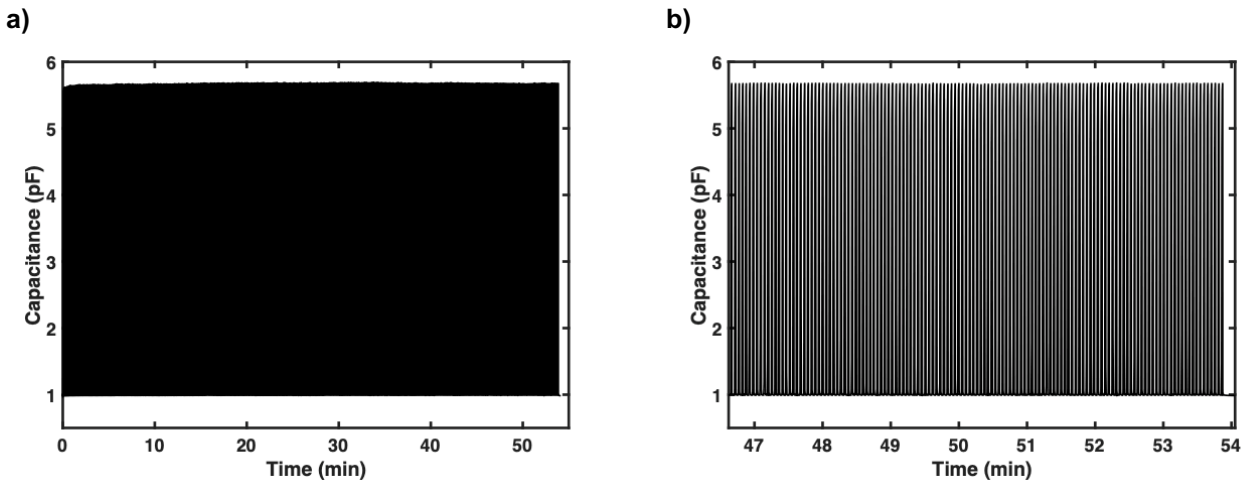

Figure 32. a) 1000 Cycles of ~24 kPa. b) Last 135 cycles of cyclic load.

Finally, cyclic load was applied to the capacitive pressure sensor over 1000 cycles as seen in Figure 32a. The last 135 cyclic load of 24 kPa is seen in Figure 32b. No permanent changes in pressure sensor was detected. This suggests the capacitive pressure sensor is robust to large cyclic loads.

7.4 Radial Pulse Detection and Blood Pressure Estimation

After electromechanical characterization of the capacitive pressure sensors, continuous health monitoring applications were explored. As suggested in previous chapters, radial applanation tonometry have become an increasingly popular method to evaluate cardiovascular health. In this work, capacitive pressure sensors were used to detect the radial pulse and correlated with beat-to-beat blood pressure. This was accomplished by measuring simultaneously with a finger volume clamp device that measures beat-to-beat blood pressure (Clearsight, Edwards Lifesciences).

7.4.1 Radial Pulse Measurement Methods

The protocol for subject testing was as follows. Written consent from subjects were first received according to IRB guidelines approved by the University of California, Irvine. Capacitive

pressure sensor (CAP) was placed on the left radial artery of the subject and secured with a velcro strap. The CAP data was linearly interpolated to match a 200 Hz sampling rate (from ~50-55 Hz sampling rate) and then smoothed (moving average of 5 data points). The Clearsight (CS) finger cuff was attached to the right index finger of the subject. The subjects were sitting upright with the CAP sensor at approximate heart level. Lights were dimmed with soothing music playing in the background during the measurements. Accelerometry and gyroscopic data were simultaneously collected using a research grade adhesive patch (BioStamp RC, MC10). Illustration of test setup can be seen in Figure 33.

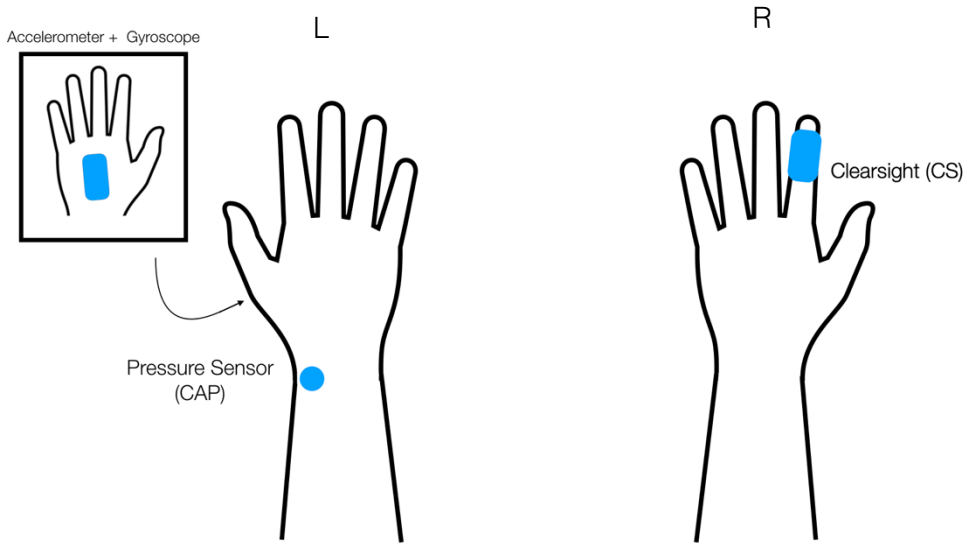

Figure 33. Blood pressure measurement setup. Handedness denoted by L (left) and R (right). Biostamp is placed on the left dorsal of the hand. CAP is placed on the left radial artery. CS is placed on the right finger index.

BioStamp was adhered to the left dorsal hand to measure movements. Movements may suggest inaccurate readings from the CAP sensor.

Subjects were asked to take deep breaths for the first 70 cardiac cycles, and then asked to breathe normally for the next 70 cardiac cycles. This protocol was done twice for a total of approximately 280 cardiac cycles (or 4 test segments). 70 cardiac cycles were chosen due to the

calibration accuracy of the CS. A total of seven subjects (5 females and 2 males; Age: 20-30; healthy) were evaluated.

7.4.2 Blood Pressure Analytical Methods

In each segment, the systolic peaks (SBP), diastolic peaks (DBP), and the mean arterial pressure (MAP) were measured simultaneously between the pressure sensor (CAP) and the Clearsight (CS). MAP, which is the average pressure throughout one cardiac cycle, was calculated with Equation 8:

$$MBP = DBP + \frac{1}{3}(SBP - DBP) \tag{8}$$

The SBP, DBP, and MAP were then plotted against each other using the CS as the reference. Linear regression analysis was then used determine correlation between the CAP and CS devices. The radial pulse signal measured with the CAP was then calibrated using the CS as the reference. 75% of the CAP data was used as a model and 25% of the CAP data was then used as a test set. Data set was randomized to remove any temporal bias. Bland-Altman analysis was then used to assess the agreement between the CAP test data set to the CS device.[121] The blood pressure measurements were averaged over 1, 3, 5, 7, and 10 consecutive cardiac cycles and plotted separately in Bland-Altman plots. The next figures display the results from these measurements.

7.4.3 Subject Data Example

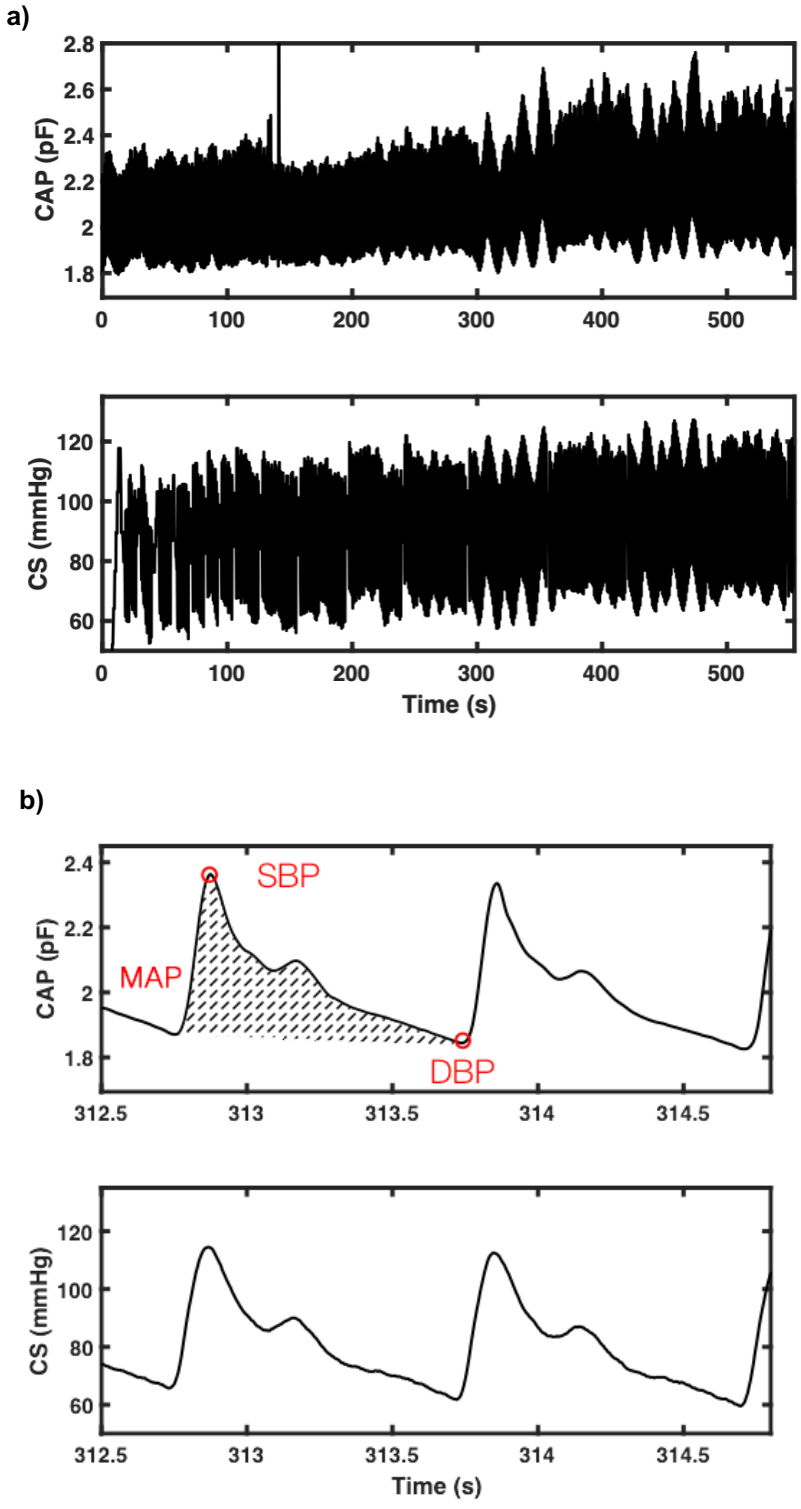

Figure 34. Subject 1 CAP and CS. a) Whole test measurement. b) Example of pulse wave form.

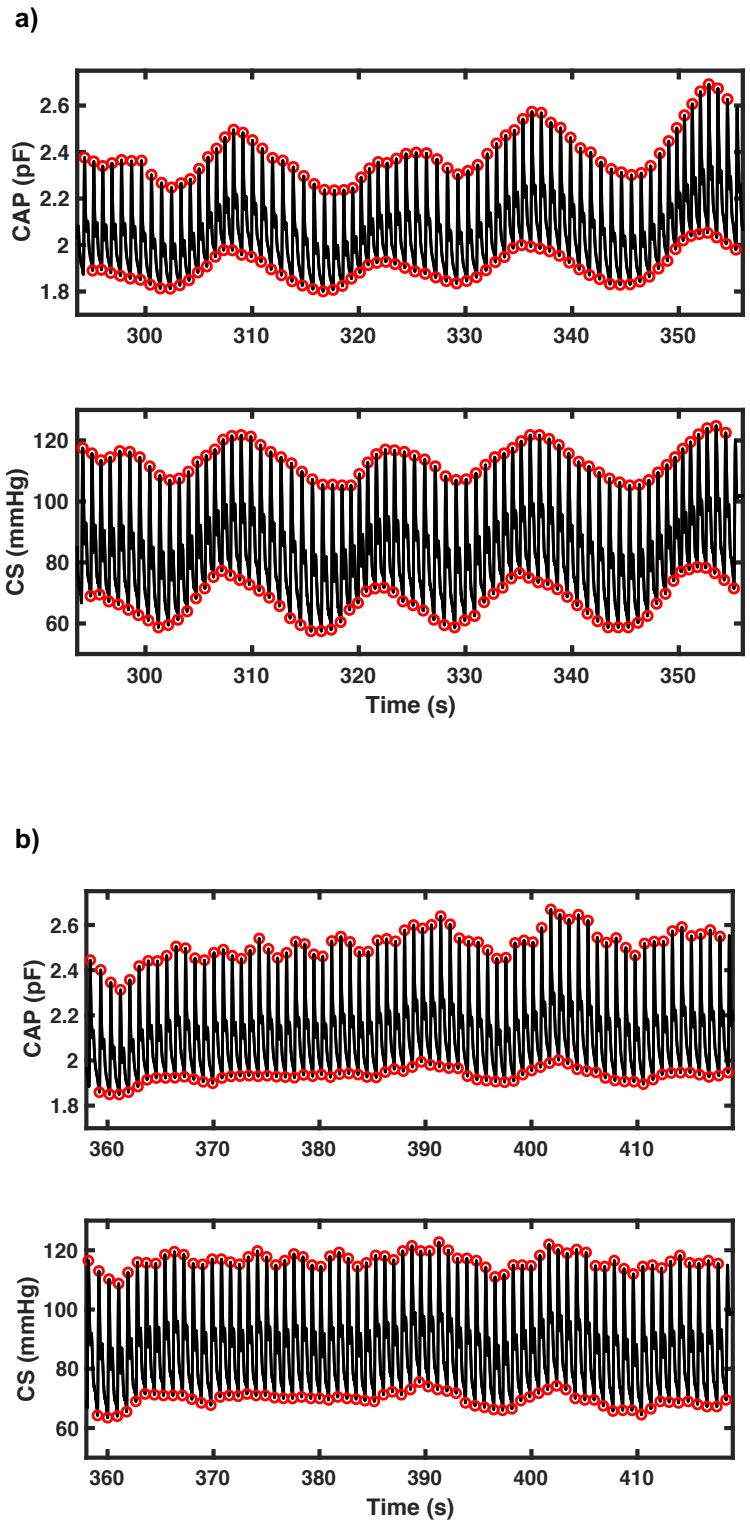

Figure 35. Subject 1. a) Example of 70 beats during deep breathing and b) the next 70 beats during normal breathing.

As seen in Figure 35a, the deep breathing maneuver induces higher blood pressure variability in both CAP and CS sensors. By breathing normally, the blood pressure variability is dampened. Therefore, deep breathing maneuver was done to simulate quick changing blood pressures and to evaluate sensor performance to track those blood pressure changes.

Following figures illustrate the linear regression analysis for SBP, DBP, and MAP for Subject 1. Deep breathing section will be denoted by 'Deep (*n*)' where *n* describes the first or second section. Likewise with normal breathing – 'Normal (*n*)'. Figures will be displayed in chronological order [e.g. Deep (1), Normal (1), Deep (2), Normal (2)].

Linear regression analysis figures will be followed by calibration studies where 75% of the randomized CAP dataset is used as a model for 25% of the CAP data. In the following figures, the model data set is shown as black circles, where the test set is shown as red triangles. After converting CAP data set into mmHg, the mean bias and standard deviation between the CS and CAP were measured. As mentioned earlier, consecutive beats were also averaged to determine how mean bias and standard deviation would change. The number of beats averaged were 1, 3, 5, 7, and 10. These plots will follow the initial linear regression analysis for each subject. Summary of the linear regression analysis for all subjects can be found in Tables 1-3.

7.5 Subject Data, Beat-to-Beat Blood Pressure Analysis

7.5.1 Subject 1

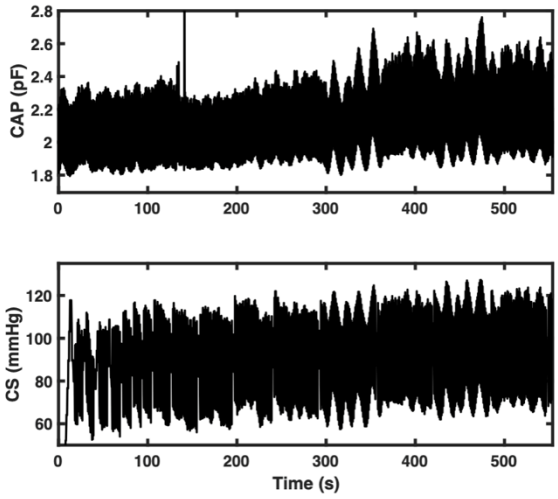

Deep (1)

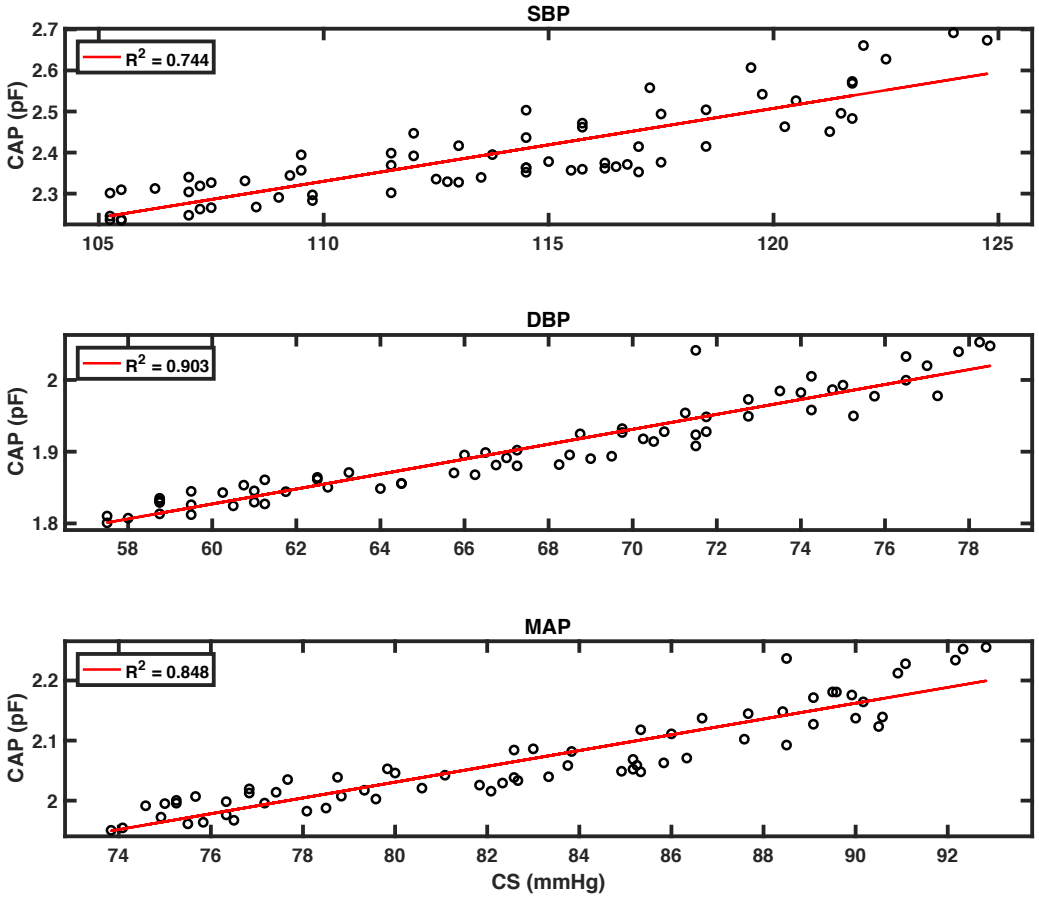

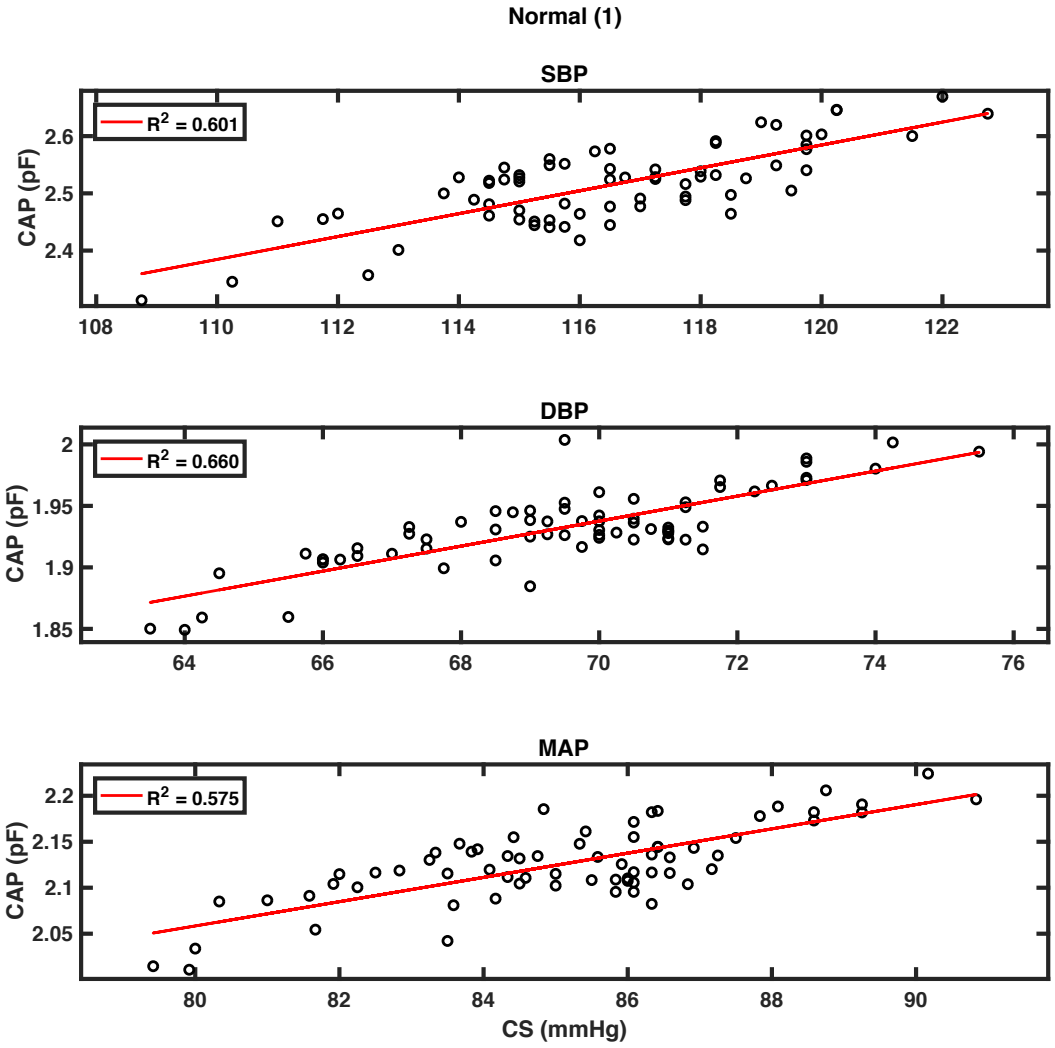
Normal (1)
SBP
R2 = 0.601
CAP (pF)
2.6
2.5
2.4
108
110
112
114
116
118
120
122
DBP
R2 = 0.660
CAP (pF)
2
1.95
1.9
1.85
64
66
68
70
72
74
76
MAP
R2 = 0.575
CAP (pF)
2.2
2.15
2.1
2.05
80
82
84
86
88
90
CS (mmHg)

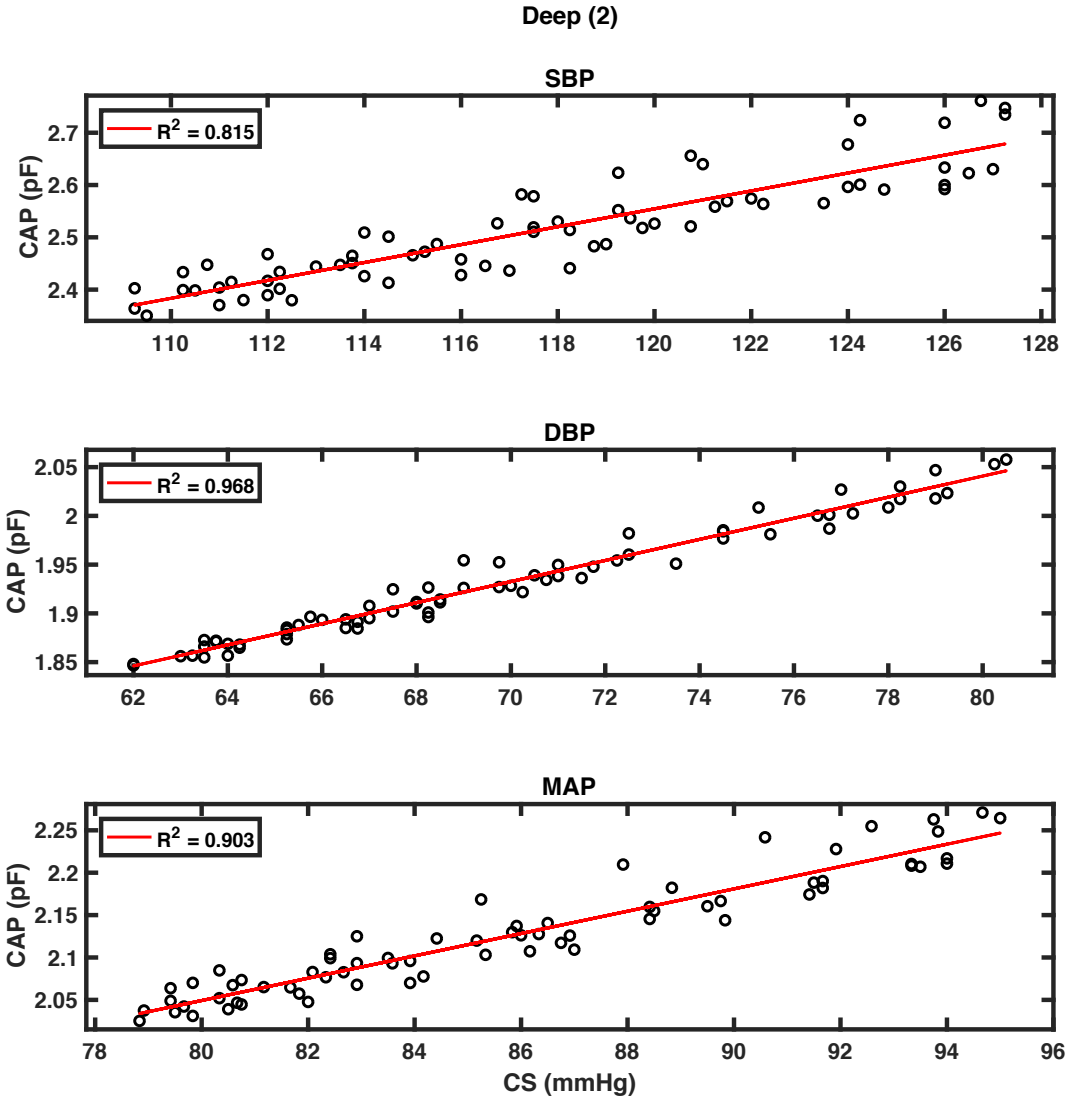
Deep (2)
SBP
R2 = 0.815
CAP (pF)
2.7
2.6
2.5
2.4
110
112
114
116
118
120
122
124
126
128
DBP
R2 = 0.968
CAP (pF)
2.05
2
1.95
1.9
1.85
62
64
66
68
70
72
74
76
78
80
MAP
R2 = 0.903
CAP (pF)
2.25
2.2
2.15
2.1
2.05
78
80
82
84
86
88
90
92
94
96
CS (mmHg)

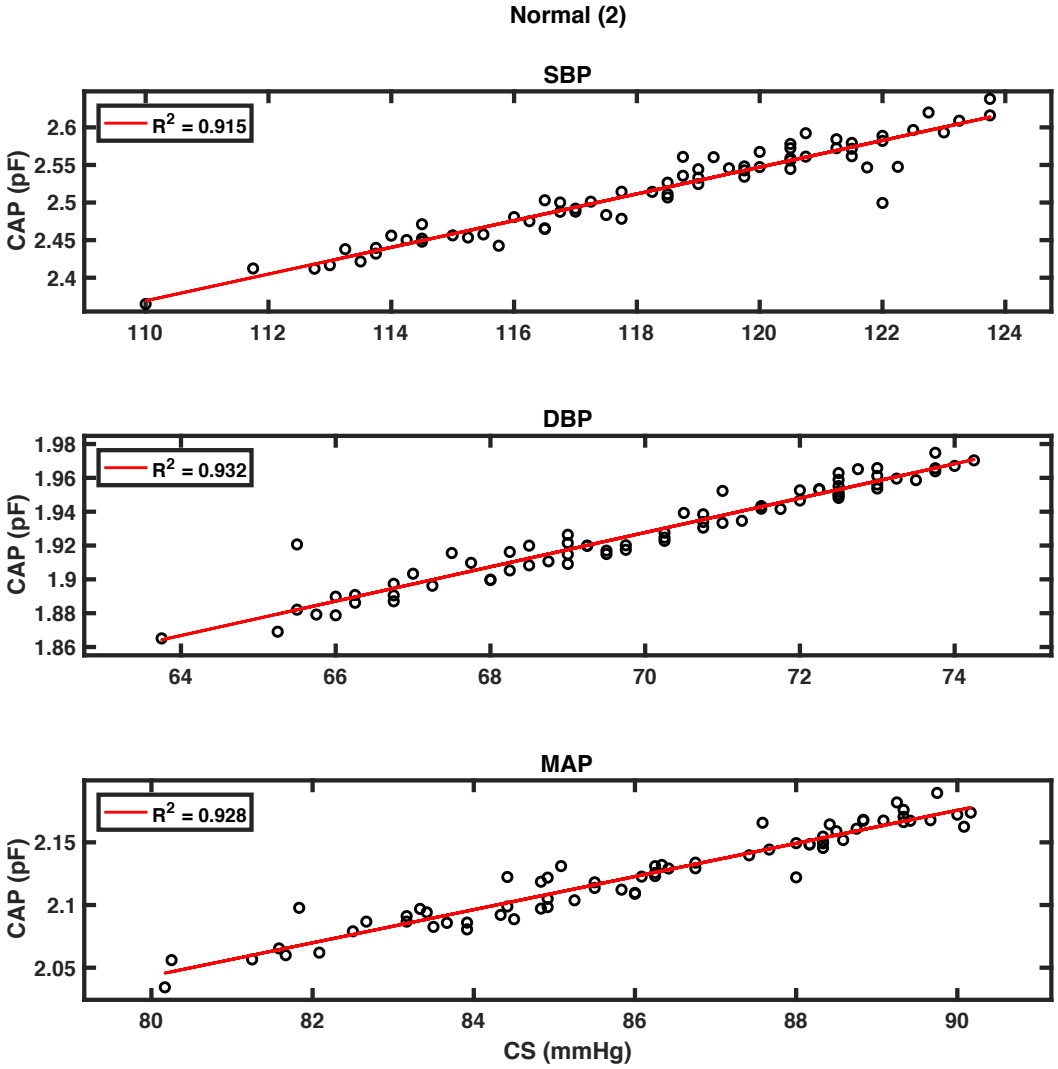
Normal (2)
SBP
R2 = 0.915
CAP (pF)
2.6
2.55
2.5
2.45
2.4
110
112
114
116
118
120
122
124
DBP
R2 = 0.932
CAP (pF)
1.98
1.96
1.94
1.92
1.9
1.88
1.86
64
66
68
70
72
74
MAP
R2 = 0.928
CAP (pF)
2.15
2.1
2.05
80
82
84
86
88
90
CS (mmHg)

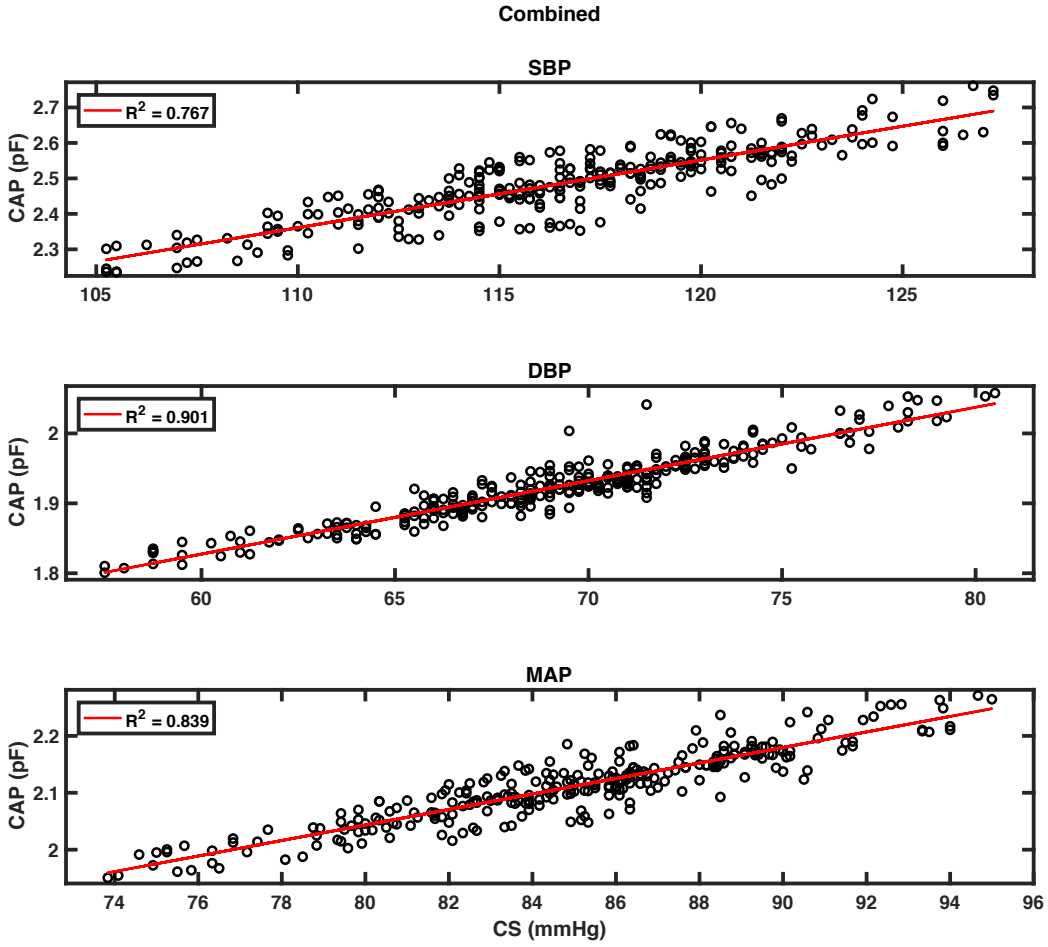
Combined
SBP
R2 = 0.767
CAP (pF)
2.7
2.6
2.5
2.4
2.3
105
110
115
120
125
DBP
R2 = 0.901
CAP (pF)
2
1.9
1.8
60
65
70
75
80
MAP
R2 = 0.839
CAP (pF)
2.2
2.1
2
74
76
78
80
82
84
86
88
90
92
94
96
CS (mmHg)

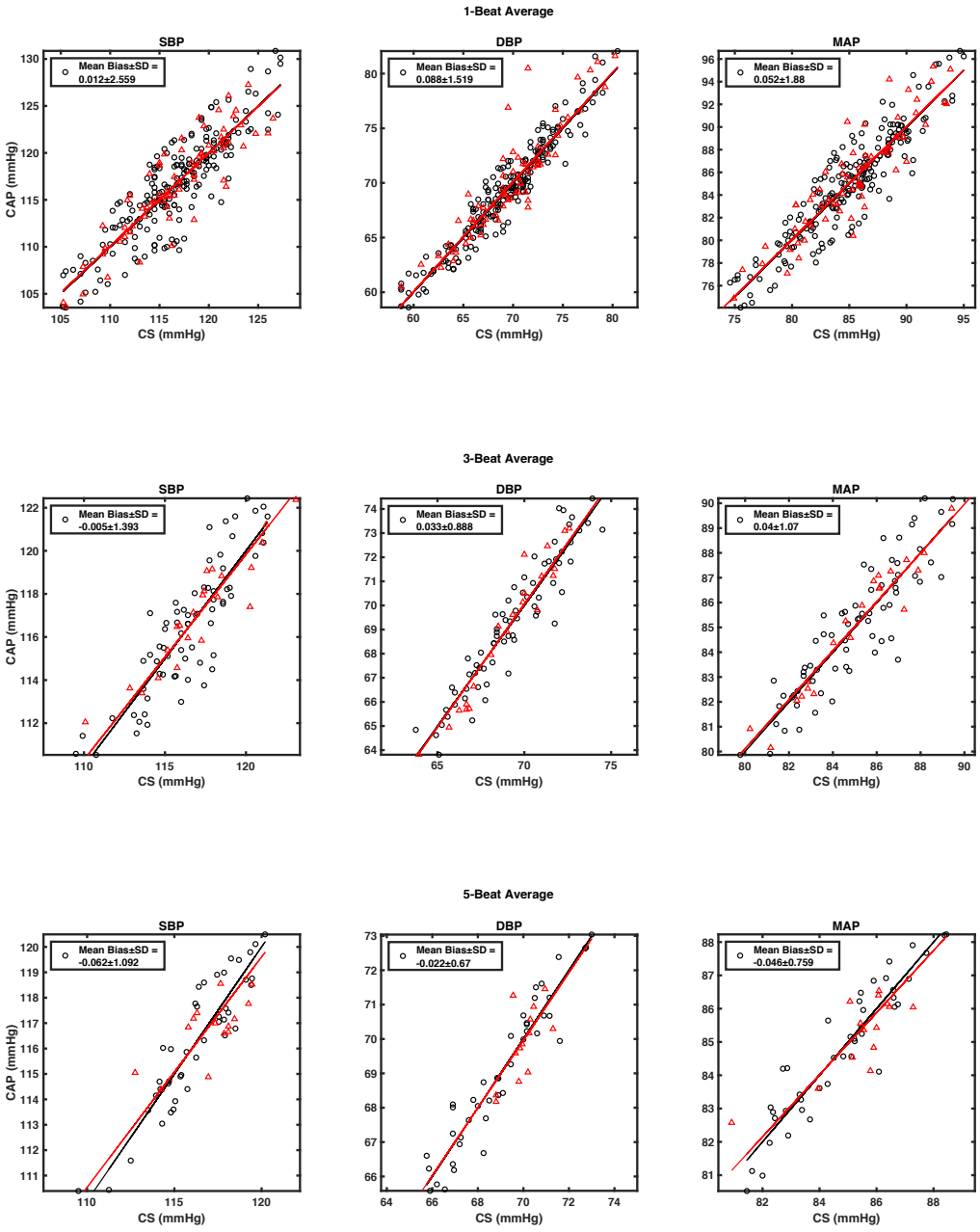
1-Beat Average
SBP
Mean Bias±SD =
0.012±2.559
DBP
Mean Bias±SD =
0.088±1.519
MAP
Mean Bias±SD =
0.052±1.88
3-Beat Average
SBP
Mean Bias±SD =
-0.005±1.393
DBP
Mean Bias±SD =
0.033±0.888
MAP
Mean Bias±SD =
0.04±1.07
5-Beat Average
SBP
Mean Bias±SD =
-0.062±1.092
DBP
Mean Bias±SD =
-0.022±0.67
MAP
Mean Bias±SD =
-0.046±0.759
CAP (mmHg)
CS (mmHg)

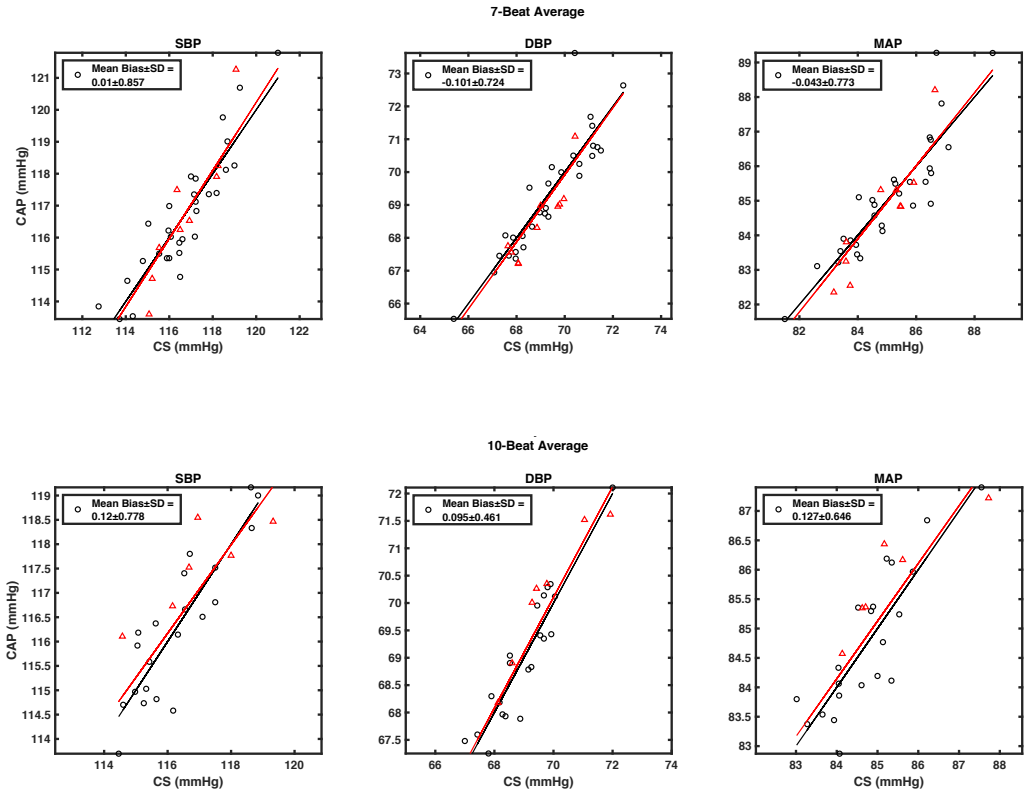

Tables 1-3 summarizes the linear regression analysis for all subjects for SBP, DBP, and MAP. To further investigate the correlation between CAP and CS, the CAP sensor was calibrated to the CS. This was validated by calibrating 75% of the CAP data to the CS device. Next the correlation between the remaining 25% of the data from the CAP sensor and the CS device was analyzed. The mean bias and standard deviation were calculated for Subject 1. Mean bias was negligible, with standard deviations of less than 1 mmHg suggesting strong agreement between the CAP and CS device. The linear regression plots can be found in the supplemental material.

Table 1. Linear regression analysis for SBP.

Subject	Deep(1)	Normal(1)	Deep(2)	Normal(2)	Combined
1	0.744	0.601	0.815	0.915	0.767
2	0.824	0.769	0.827	0.639	0.754
3	0.460	0.798	0.839	0.767	0.657
4	0.650	0.821	0.720	0.886	0.578
5	0.755	0.235	0.317	0.469	0.554
6	0.429	0.479	0.866	0.680	0.468
7	0.733	0.743	0.619	0.289	0.536

Table 2. Linear regression analysis for DBP.

Subject	Deep(1)	Normal(1)	Deep(2)	Normal(2)	Combined
1	0.903	0.660	0.968	0.932	0.901
2	0.929	0.912	0.921	0.794	0.906
3	0.696	0.841	0.871	0.765	0.769
4	0.646	0.942	0.900	0.978	0.809
5	0.934	0.707	0.848	0.822	0.865
6	0.889	0.843	0.972	0.900	0.848
7	0.887	0.964	0.872	0.664	0.837

Table 3. Linear regression analysis for MAP.

Subject	Deep(1)	Normal(1)	Deep(2)	Normal(2)	Combined
1	0.848	0.575	0.903	0.928	0.839
2	0.897	0.843	0.845	0.684	0.843
3	0.513	0.836	0.809	0.728	0.687
4	0.404	0.893	0.728	0.936	0.636
5	0.896	0.535	0.693	0.734	0.789
6	0.637	0.663	0.871	0.805	0.576
7	0.764	0.913	0.769	0.471	0.704

7.5.8 Bland Altman Analysis of All Subjects Combined

Following plot shows the Bland-Altman analysis of all subject data combined. Note that the 5 consecutive cardiac cycles were averaged prior to creating the calibration model. Bland-Altman plots with different number of average cardiac cycles can be seen in SI.7. Red triangles denote the DBP, green squares denote the MAP, and blue circles describe the SBP.

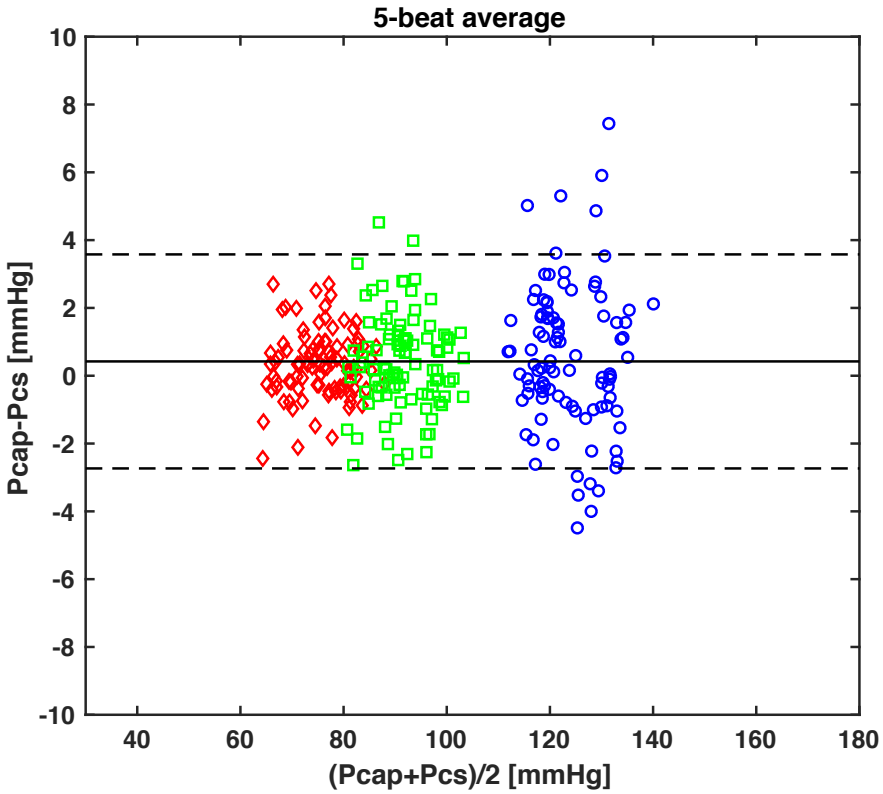

Figure 36. Bland-Altman plot of all subject data combined. 5 consecutive cardiac cycles were averaged prior to creating the model.

The mean bias and standard deviation for SBP, DBP, and MAP are shown in Table 4. Table 5 shows the mean bias and standard deviation for the combined blood pressure values. The results from Table 4 show minimal mean biases with small standard deviations suggesting strong agreement between the CAP and CS device. However, as seen in Table 1 the SBP had moderate

to low R^2 values across many subjects. This is evident in the Bland-Altman plots in Figure 36 and SI.7. It has been reported that the CS device has difficulties measuring SBP, and is apparent when compared to a radial catheter device.[3] Therefore, large mean biases and standard deviations are to be expected for SBP.

Table 4. CAP and CS comparison of SBP, DBP, and MAP.

Beat Average	Pairs	Mean Bias ± SD SBP	Mean Bias ± SD DBP	Mean Bias ± SD MAP
1	475	-0.527±4.416	-0.185±2.038	-0.338±2.940
3	160	0.108±2.702	0.056±1.182	0.086±1.750
5	97	0.529±2.148	0.329±0.979	0.410±1.390
7	70	-0.206±2.472	-0.123±0.864	-0.151±1.372
10	49	0.106±1.390	0.004±0.671	0.030±0.881

Table 5. Combined CAP and CS comparison.

Beat Average	Pairs	Mean Bias ± SD Combined
1	1,425	-0.350±3.282
3	480	0.083±1.976
5	291	0.422±1.578
7	210	-0.160±1.699
10	147	0.047±1.020

Bland-Altman analysis shows when calibrated against the CS device, the CAP sensor is able to accurately and precisely measure blood pressure. This is validated by observing the mean bias and standard deviation as shown in Table 5. International Standard Organization (ISO) standard 81060-2 requires the NIBP accuracy (mean bias) and precision (standard deviation) not exceed 5 mmHg and 8 mmHg respectively against an arterial line. Here, I have shown results showing accuracy and precision well below the ISO standard. However, the measurements tested here used a NIBP as a reference. Further studies testing against an arterial are required to determine

true accuracy and precision. Nevertheless, statistical analysis shows strong agreement between the CAP and CS suggesting CAP sensors are capable of measuring beat-to-beat blood pressure.

7.4 Conclusion

Here I have introduced a flexible capacitive pressure sensor using a shrinking fabrication process platform with wrinkled Au thin film. The wrinkled structures in addition to air gaps in dielectric layers have improved pressure sensitivities by approximately 3 times to allow for detections of radial pulsatile blood flow. I have shown robustness of these sensors by subjecting to cyclical pressure over 1000 cycles. Lastly, I have introduced another means of measuring beat-to-beat blood pressure using soft CAP sensors. Next future studies that may expand the scope of this work will be discussed.

CHAPTER 8: FUTURE DIRECTIONS

In this dissertation, I have shown a proof of concept on how to develop soft piezocapacitive pressure sensors using a thermally induced shrinking fabrication process. However, there is a need to better understand and engineer these sensors to be able to more robustly capture the target signal. For example, as shown in the figures there were many difficulties in being able to measure pulsatile blood flow due to low sensitivities and noise from environmental movement. To address this issue, ridged structures were introduced to create larger airgaps to improve pressure sensitivities in the z-direction. With these sensors pulsatile blood flow detection was more robustly measured and had better correlations to continuous blood pressure measurements taken with the ClearSight.

8.1 Dielectric Doping

Another opportunity for future studies is to investigate doping of the dielectric layer to form a larger dynamic pressure sensitivity. As explained by Equation 6, compression of air gaps will change effective dielectric constant closer to that of the bulk dielectric material (in this case silicone elastomer ~2-3). Doping thin layers of the dielectric layer can increase pressure sensitivities during compression by modulating between a low and high dielectric constant. Such materials may include piezoelectric nanoparticles such as $BaTiO_3$, which has a dielectric constant of 150. However, thin film thicknesses should be carefully considered to optimize the dynamic dielectric layer.

8.2 Mapping with Redundant Sensors

Another future study that must be done is to incorporate signal processing methods such as adaptive filtering. Soft sensors inherently will not be perfect and will be prone to motion artifacts and will require signal processing strategies. For example, noise coming from environmental noise can be subtracted by introducing a redundant sensor that does not measure the target signal. This

signal can then be used as a baseline for the target sensor which can help filter out low frequency changes that come from environmental noise. To accomplish this, a grid of electrodes can be made such that each overlapping electrode is a sensing 'pixel'. These sensors can also be fabricated all on one substrate. Preliminary measurements show this may be possible as shown in Figure 37.

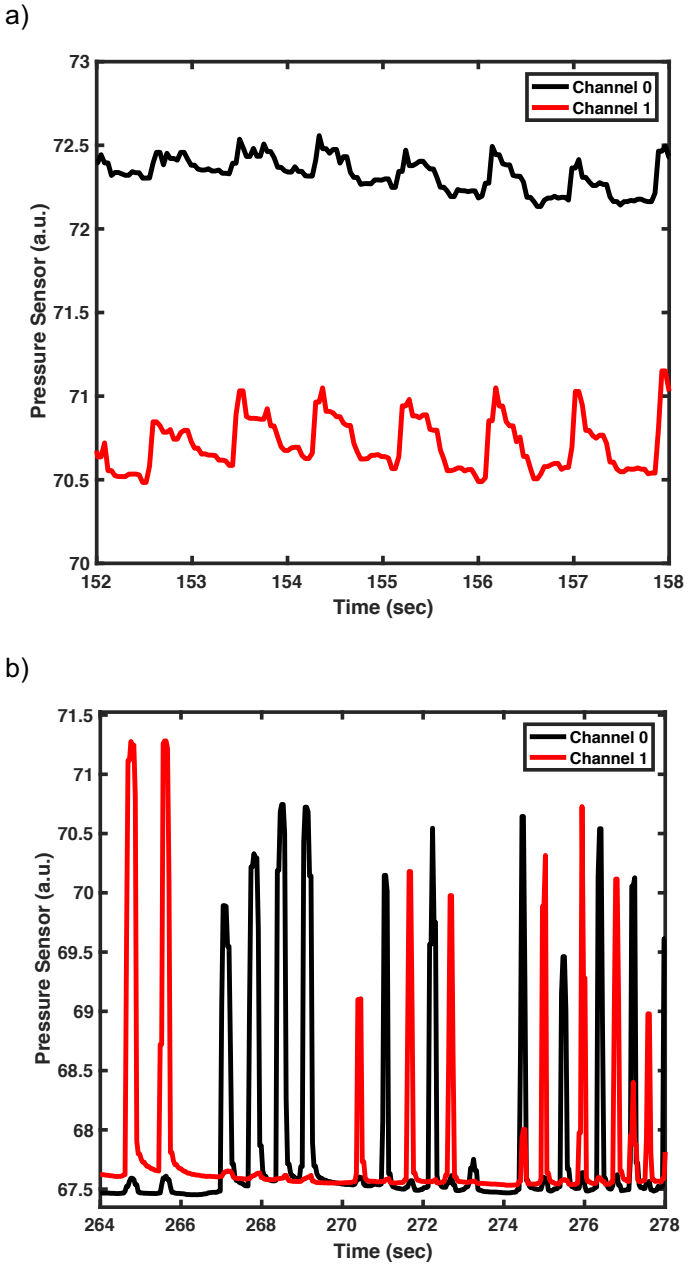

Figure 37. a) Radial pulse detection using two capacitive sensors simultaneously. Measurements taken on Texas Instruments FDC 2214 EVM. b) Manual pressing of different sensors separated by ~ 2mm apart.

Soft sensors demonstrated in this thesis are capable of fine spatial resolution of mechanical pressure. The spatial resolution will depend on the mechanical properties of the sensor substrate. Stiffer substrates will delocalize stress over the entire substrate. Softer substrates will have more localized stress which may greatly improve spatial resolution. Further investigation is required to support these claims.

8.3 Ambulatory NIBP monitoring applications

Finally, deep dive studies are needed to better understand the data collected from these sensors. Here, I have shown that piezocapacitive sensors are able to capture blood pressure in a short time frame (~280 cardiac cycles). However, there is a need to extend these time frames for ambulatory monitoring applications (24/7). For example, in Figure 38 subject was tested for approximately 28 minutes.

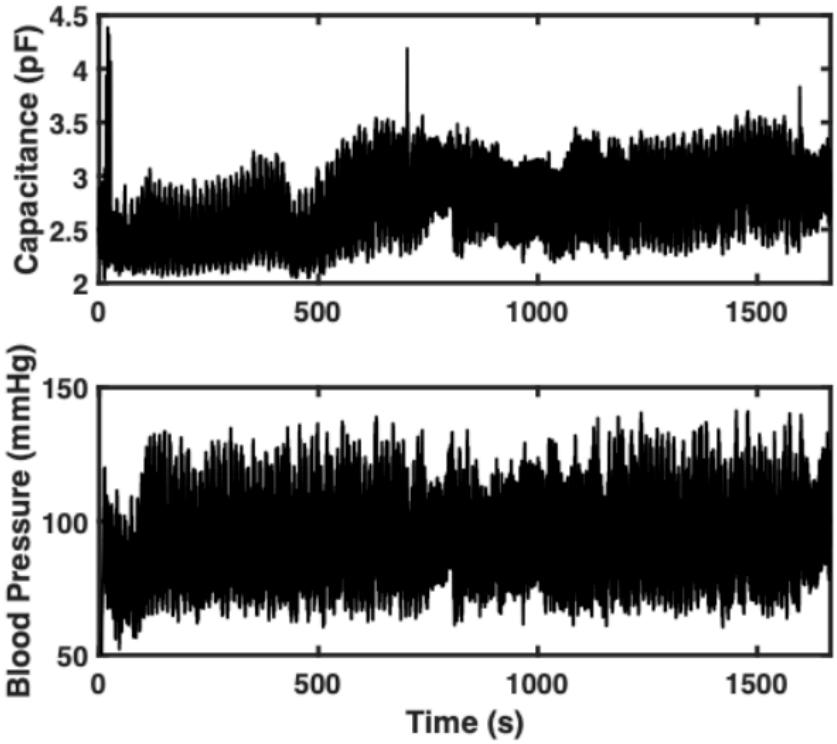

Figure 38. Radial tonometry measurement with capacitive pressure sensor for approximately 28 minutes.

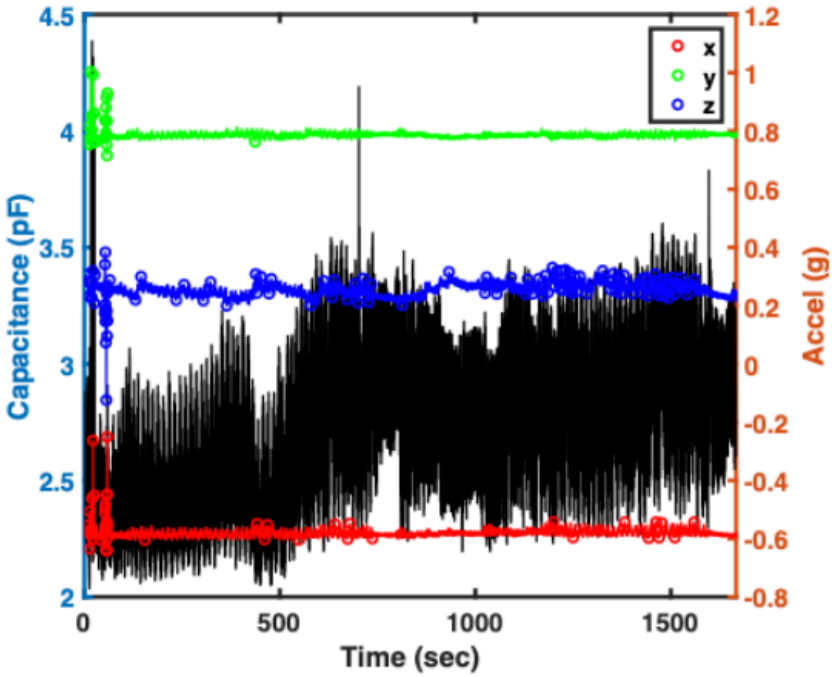

Figure 39. Accelerometer data and radial pulse data superimposed.

Figure 39 illustrates the subject's movement during the 28 minute measuring period. The measurement demonstrates that movement greatly impacts the fidelity of the signal leading to low frequency changes in the pulse measurements. For ambulatory measurements, additional sensors are needed to provide feedback for accurate radial pulse measurements. These sensors may include accelerometers, gyroscopes, and redundant pressure sensors as previously mentioned. By combining data from these sensors, it may be possible to develop a feedback loop for accurate blood pressure measurements.

In addition to longer term studies, the ability to quickly capture sudden changes in blood pressure is clinically relevant and necessary. Therefore, further investigation is needed to improve response times and dynamic range of the pressure sensitivity to capture these quick and large changes in blood pressure. Preliminary results show that this may be possible with the CAP sensors

introduced here as shown in Figure 39. Subject was asked to hold breath and blow air out against a closed nose. This induces large and sudden changes in blood pressure after breathing in again.

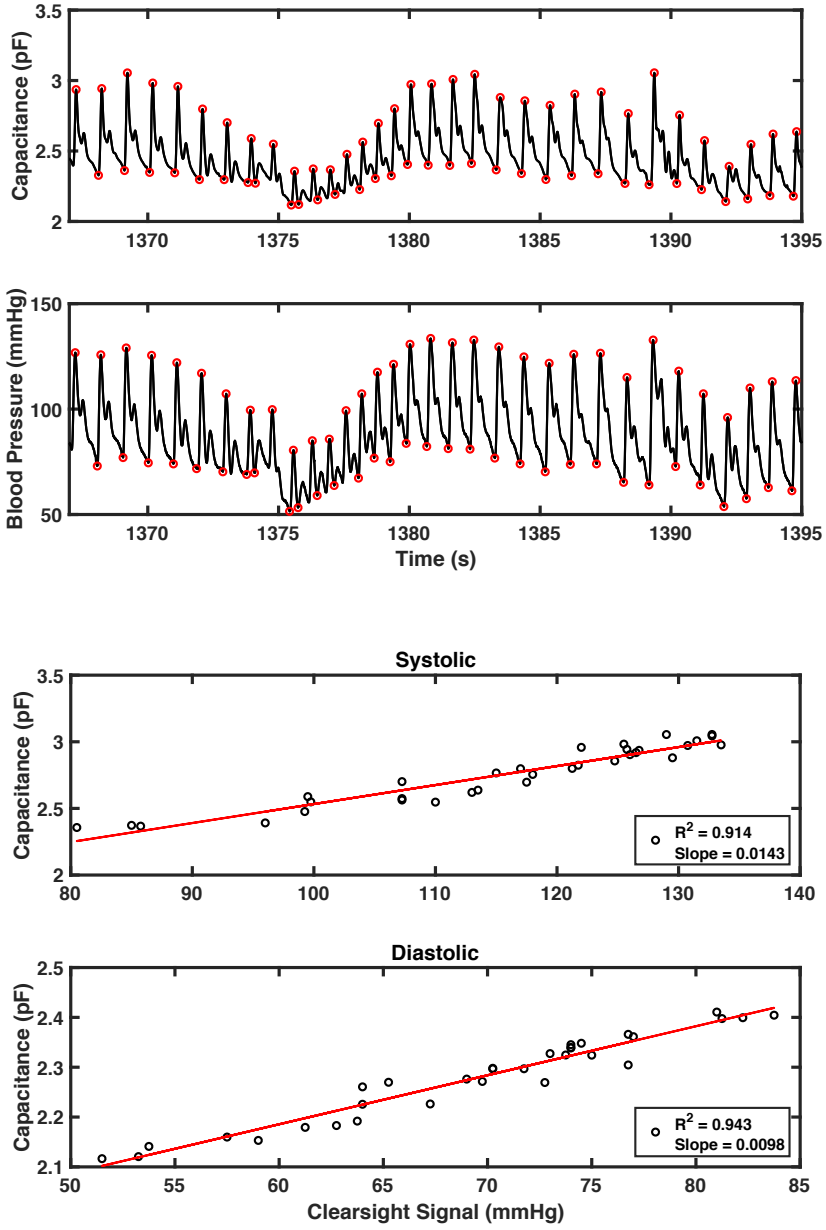

Figure 40. Sudden changes in blood pressure are measured. Systolic and diastolic pressure show strong agreement between the CAP and CS devices. *Note: some peaks were not properly detected, however the differences are negligible.

8.4 Blood Pressure Calibration

Another advancement that is needed is a way to calibrate radial tonometry measurements to blood pressure. Currently, the studies done here have shown a correlation and calibration to a continuous beat-to-beat NIBP device. A robust protocol must be designed in order to accurately calibrate the radial pulse measurements for ambulatory applications. In addition, other methods of calibration should be pursued that do not rely on other NIBP devices. For example, calibration studies may include understanding how the radial arterial pressure propagates through the tissue. Characterizing the mechanical properties of the human tissue in the wrist may provide a means to develop a model for accurate blood pressure measurements using radial tonometry. Imaging tools such as ultrasound doppler and optical coherence tomography may be used to characterize the mechanical properties of the human tissue to help develop this model.

In this work, central blood pressure was never measured. There is increasing evidence that central pressure is better correlated with future cardiovascular events than brachial artery pressure.[116,122] Therefore, there is still a need to measure at different locations of the body to better estimate the central arterial pressure. Other locations might include the carotid artery which is closer to the heart in comparison to the radial artery. The temporal artery is also another suitable artery for detecting blood pressure. By quantifying the pressure exerted at other arterial locations, it may be possible to develop a robust model for measuring central arterial pressure using pressure sensors.

8.7 Other Biometric Signals

The human body has many different biometric signals that can be measured to evaluate one's health. Another interesting parameter is to investigate respiration. Using stretchable strain sensors, it is possible to estimate lung volume based off the expansion of the torso. More importantly, there is sufficient evidence that respiration greatly impacts blood pressure.[123–126]

Preliminary study using stretchable strain sensors and pressure sensors attached to the radial artery show a correlation between the sensors as seen in Figure 41. As seen in Figure 41, inhalation (increased electrical resistance) is followed by an increase in radial arterial pressure.

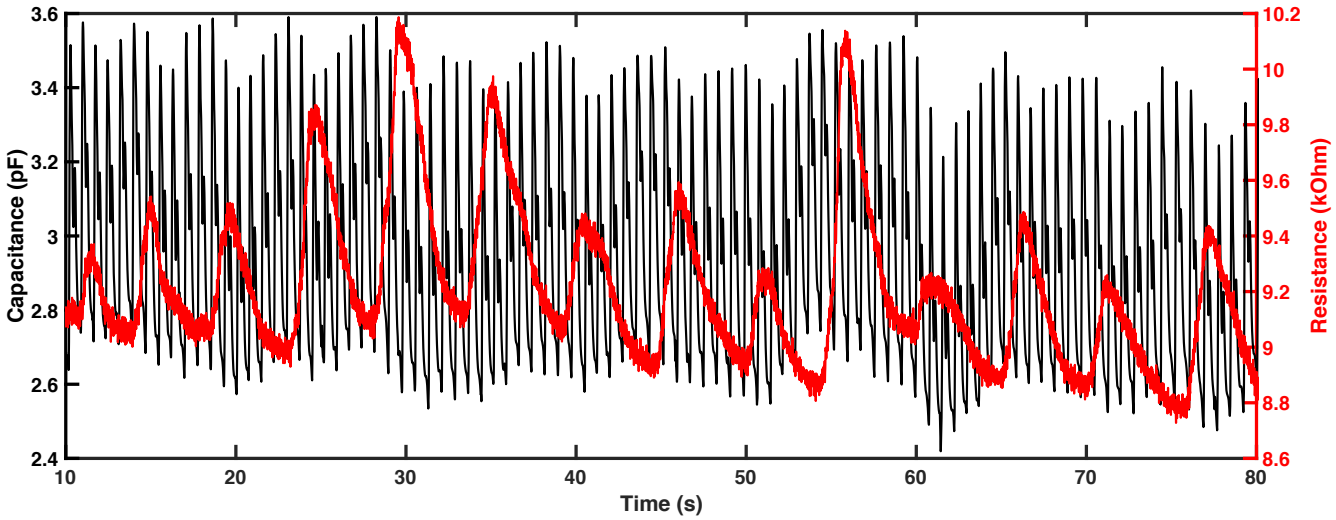

Figure 41. Respiration data shown in red and radial pulse data shown in black. Inhalation corresponds to increased electrical resistance and exhalation corresponds to decreased electrical resistance.

Pulse transit time (PTT) is another parameter that has become increasingly popular to estimate using an electrocardiogram (ECG) and an optical/pressure sensor attached at a peripheral site. PTT is the time it takes for a pulse wave to travel from the heart to the peripheral site. The time it takes to reach the peripheral site can be used to estimate blood pressure and arterial stiffness.[127–130] Preliminary studies using a commercially available ECG and capacitive pressure sensors is shown in Figure 42.

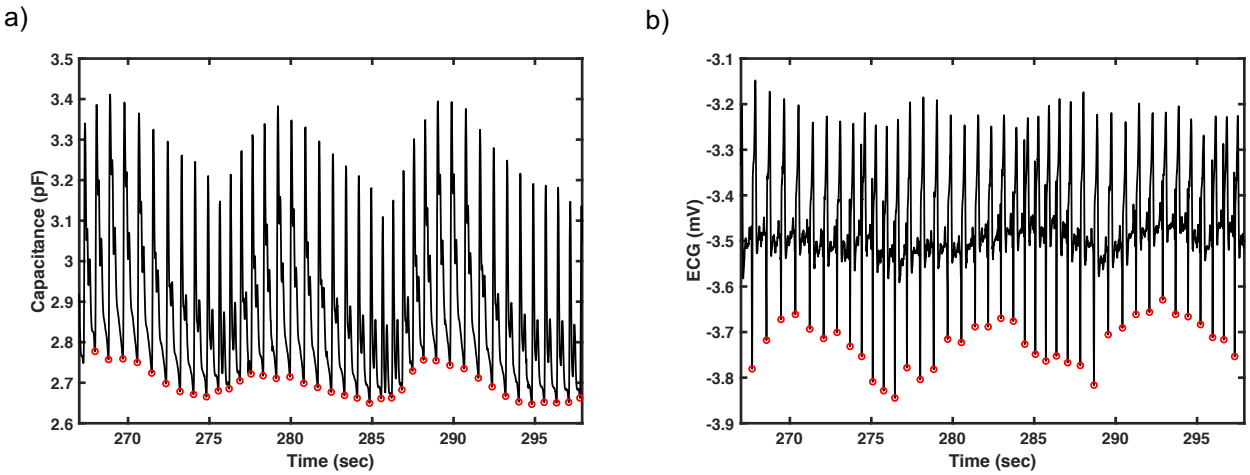

Figure 42. a) Radial pulse measurement and b) ECG measurement taken simultaneously. Diastolic peaks of the radial pulse and the 'S' wave of the ECG was chosen (R-wave was minimal therefore S-wave was used as a proxy).

PTT was then calculated using the ECG and the radial pulse information. This was calculated by taking the time difference between the S-wave of the ECG signal and the following diastolic peak of the radial pulse. Note, typically R-wave is used in PTT calculations, however the dampened ECG signal made it difficult to detect the R-wave. Therefore S-wave was used as a proxy. As seen in Figure 43, the PTT was plotted with the CAP signal. The PTT was then plotted against the systolic peaks of the radial pulse measurements as seen in Figure 44.

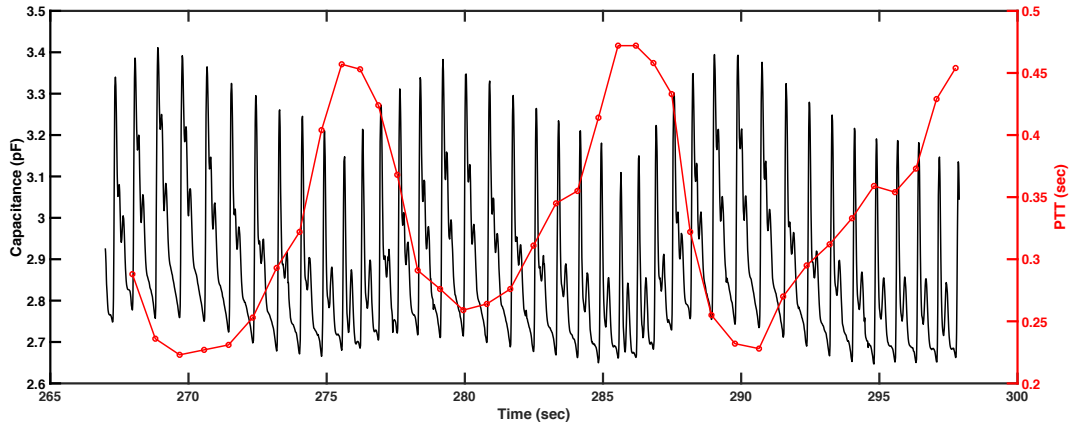

Figure 43. PTT calculated for the corresponding radial pulse measurement.

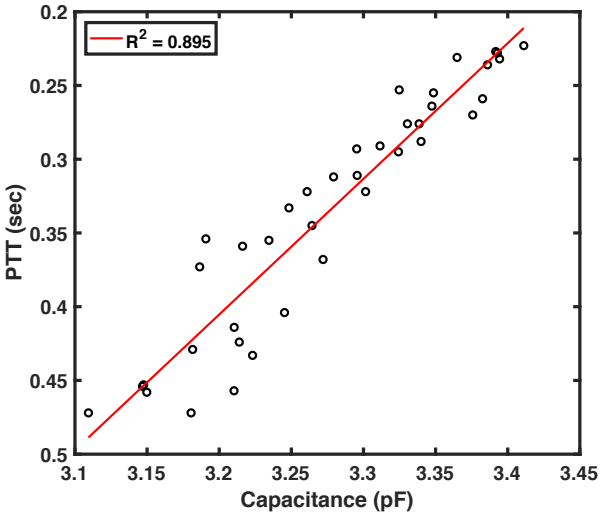

Figure 44. PTT plotted against the systolic peak from the radial pulse measurement.

Finally, heart rate variability (HRV) is another common parameter that has clinical relevance.[131–133] This is easily calculated by measuring the time difference between each cardiac cycle. For radial pulse measurements, the HRV can be measured by taking the time difference between the systolic peaks. For ECG, HRV is typically calculated by observing the R-R peak intervals. An example of HRV from radial pulse measurements and ECG can be seen in Figure 45.

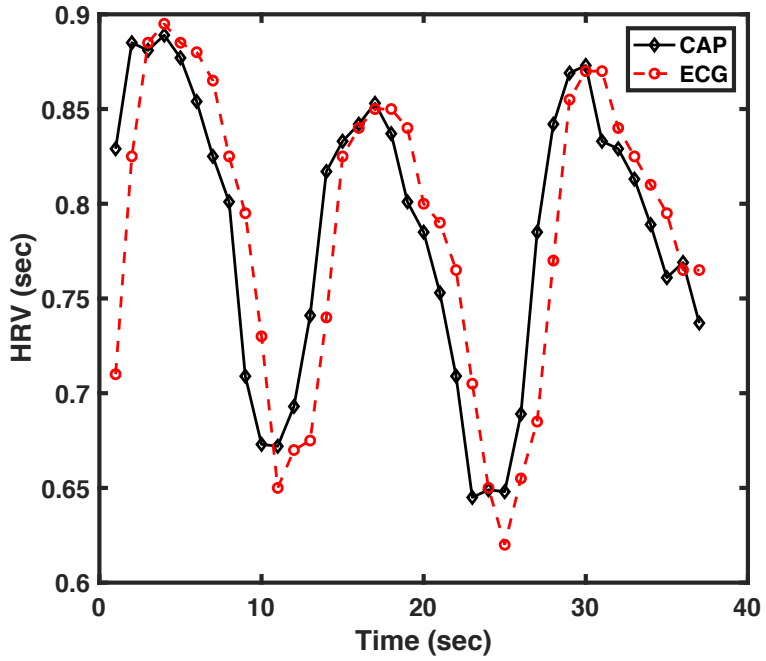

Figure 45. HRV measurements from radial pulse using capacitive pressure sensor (CAP) and ECG.

As expected, the ECG signal leads the CAP signal. Also, it is also expected that the peak-to-peak interval time difference should be mirrored between the ECG and CAP sensor. By measuring at peripheral sites, more information can be captured that may reveal localized cardiovascular complications. This should be further investigated.

8.6 Sensor Materials and Form Factor

I have demonstrated pressure sensors using PDMS substrates. These materials are still an order of magnitude stiffer than the human skin and are not ideal for conformal electronics. Other materials such as Ecoflex (~*E:* 60 kPa) may be more suitable for conformal contact to the body. However, pressure sensing may become more difficult when sensor substrates are softer. The soft nature of the materials may make it difficult to carefully stack electronic materials consistently on top of each other, which is necessary process to develop sensitive capacitive pressure sensors. Further investigation of other substrate materials is required to determine the best form factor wearable pressure sensor.

8.7 Final Remarks

With the advent of novel methods and materials to develop soft sensors, ambulatory monitoring today can be more accurate and precise. Developing soft sensor biomedical devices may prove beneficial and contribute greatly to the field of epidemiology. As researchers gather unprecedented large amounts of human health data, our understanding of human health may greatly change that which can influence health guidelines and policies. As manufacturing technologies improve and evolve, soft sensors may receive the necessary scalability to become prevalent in our everyday lives. Here in this work, I have demonstrated one of many possibilities to develop these types of soft sensors that may potentially motivate other new biomedical technologies in the future.

SUPPLEMENTAL MATERIALS

SI.1 Subject 2

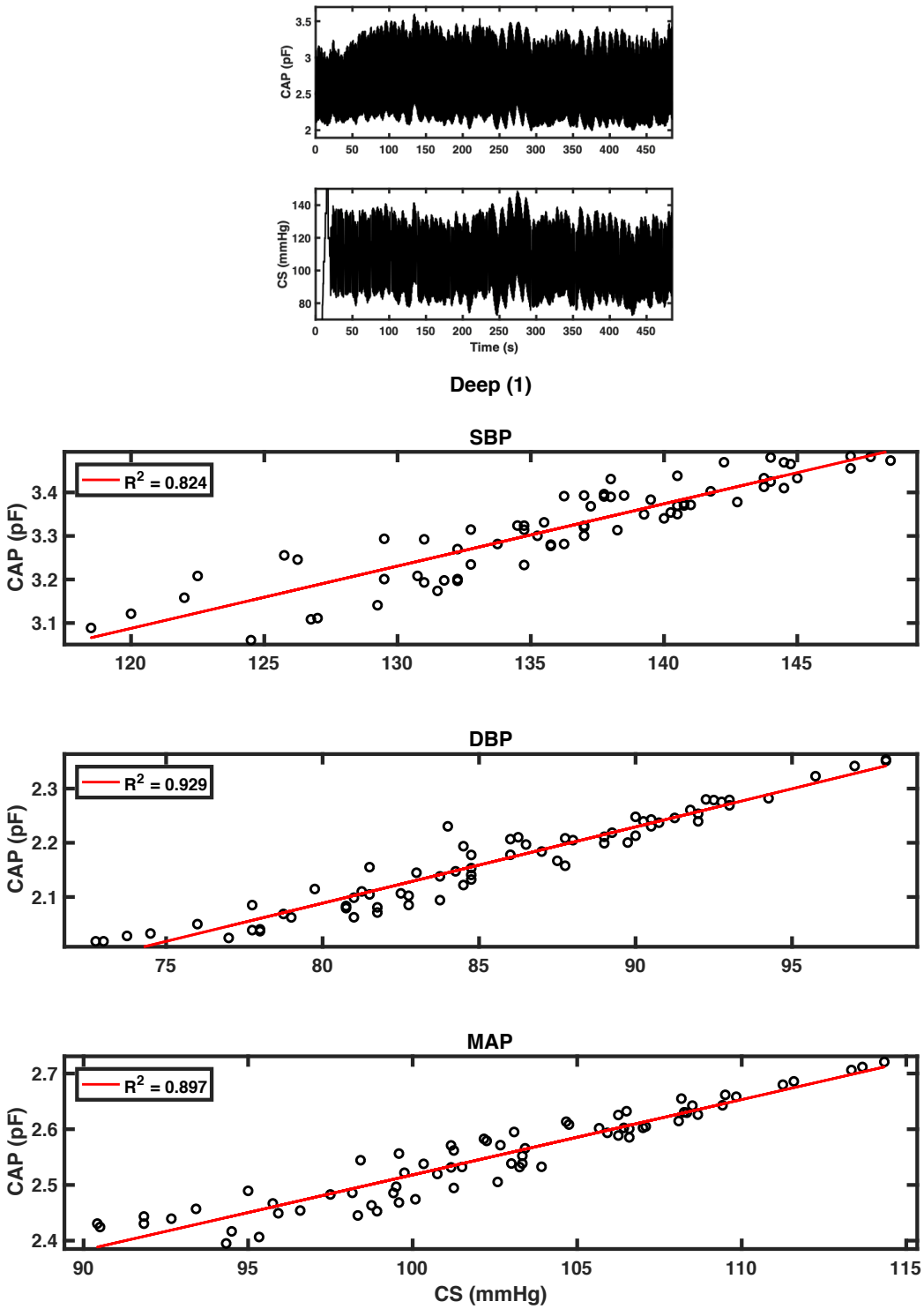

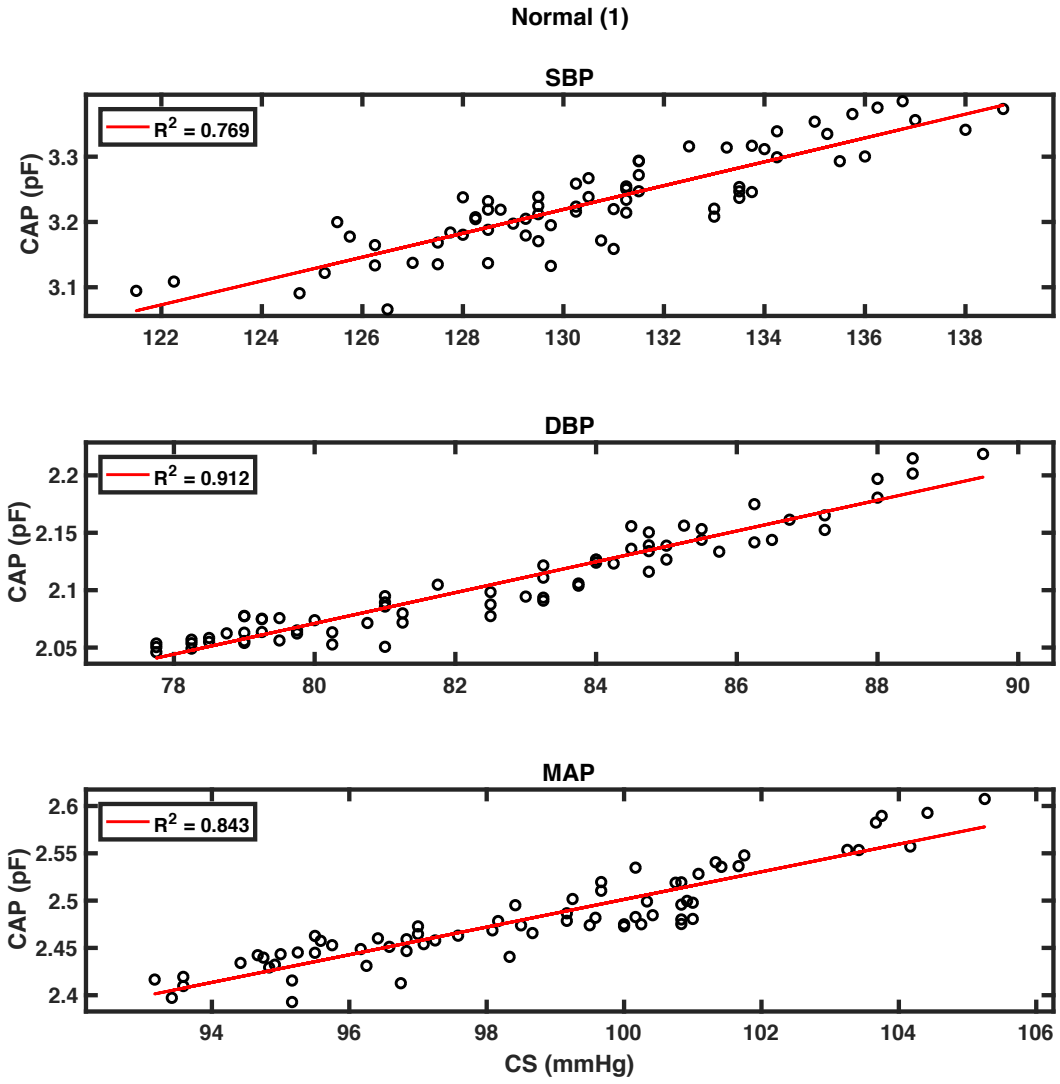
Normal (1)
SBP
R2 = 0.769
CAP (pF)
3.3
3.2
3.1
122
124
126
128
130
132
134
136
138
DBP
R2 = 0.912
CAP (pF)
2.2
2.15
2.1
2.05
78
80
82
84
86
88
90
MAP
R2 = 0.843
CAP (pF)
2.6
2.55
2.5
2.45
2.4
94
96
98
100
102
104
106
CS (mmHg)

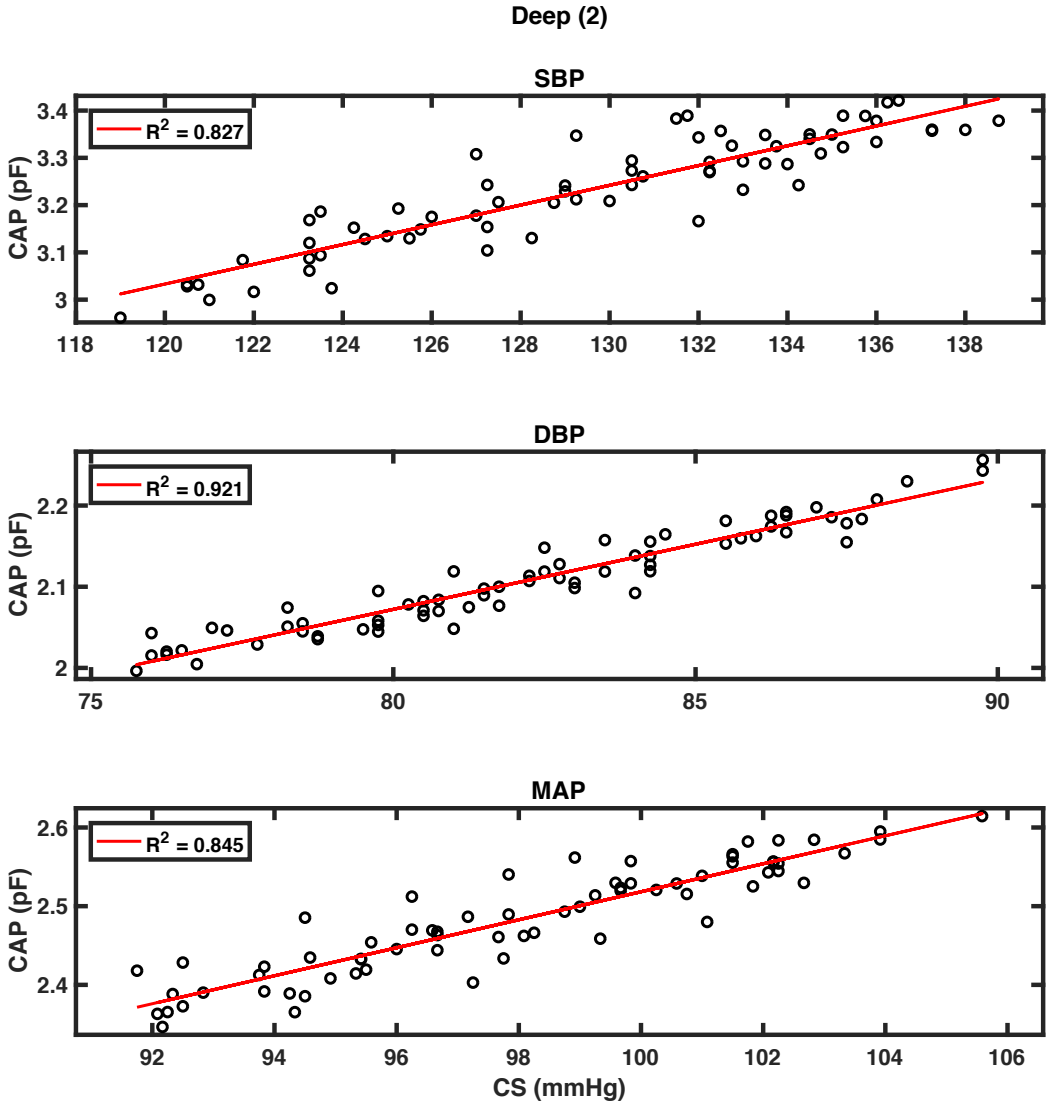
Deep (2)
SBP
R2 = 0.827
CAP (pF)
3.4
3.3
3.2
3.1
3
118
120
122
124
126
128
130
132
134
136
138
DBP
R2 = 0.921
CAP (pF)
2.2
2.1
2
75
80
85
90
MAP
R2 = 0.845
CAP (pF)
2.6
2.5
2.4
92
94
96
98
100
102
104
106
CS (mmHg)

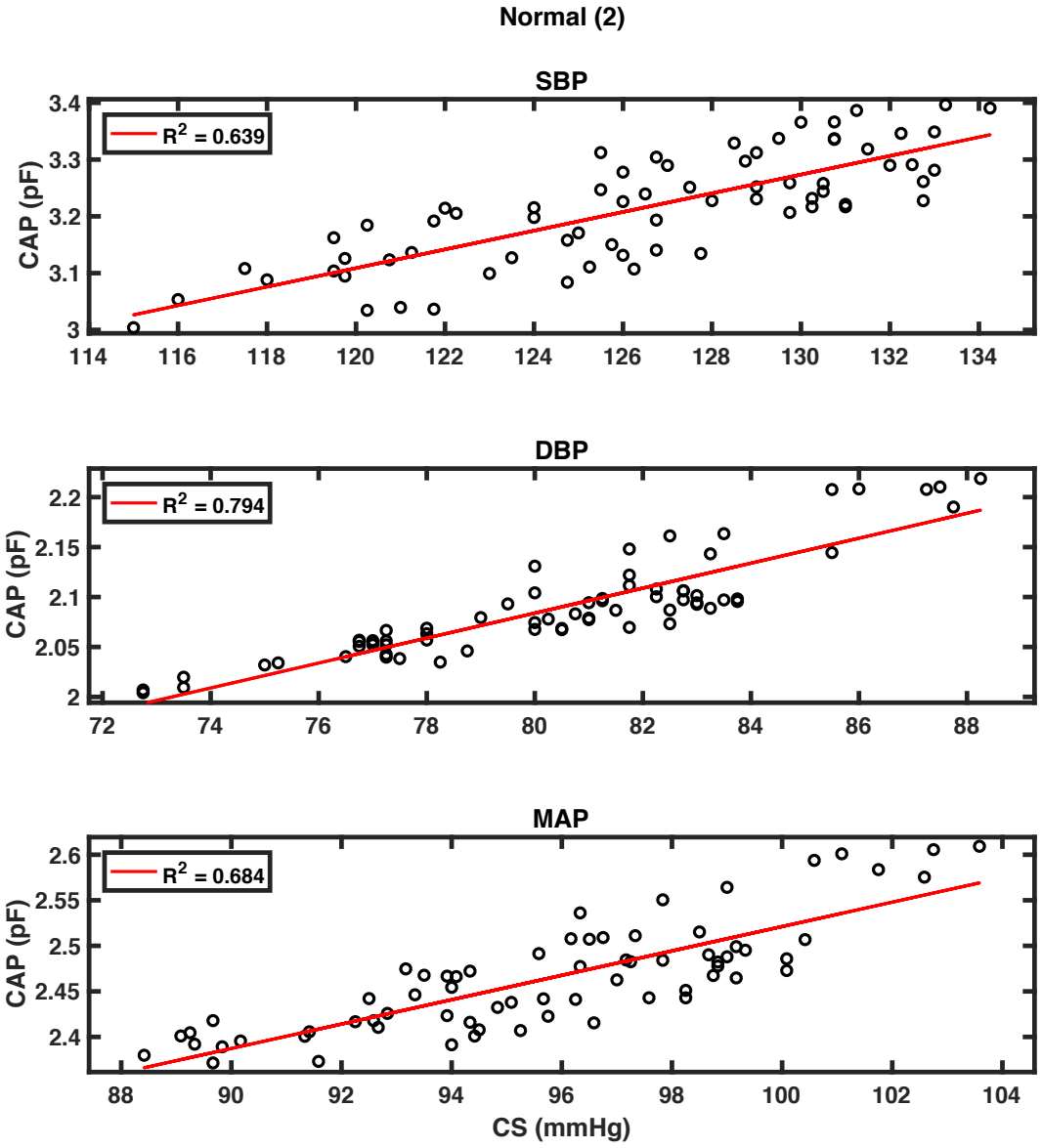
Normal (2)
SBP
R2 = 0.639
CAP (pF)
3.4
3.3
3.2
3.1
3
114
116
118
120
122
124
126
128
130
132
134
DBP
R2 = 0.794
CAP (pF)
2.2
2.15
2.1
2.05
2
72
74
76
78
80
82
84
86
88
MAP
R2 = 0.684
CAP (pF)
2.6
2.55
2.5
2.45
2.4
88
90
92
94
96
98
100
102
104
CS (mmHg)

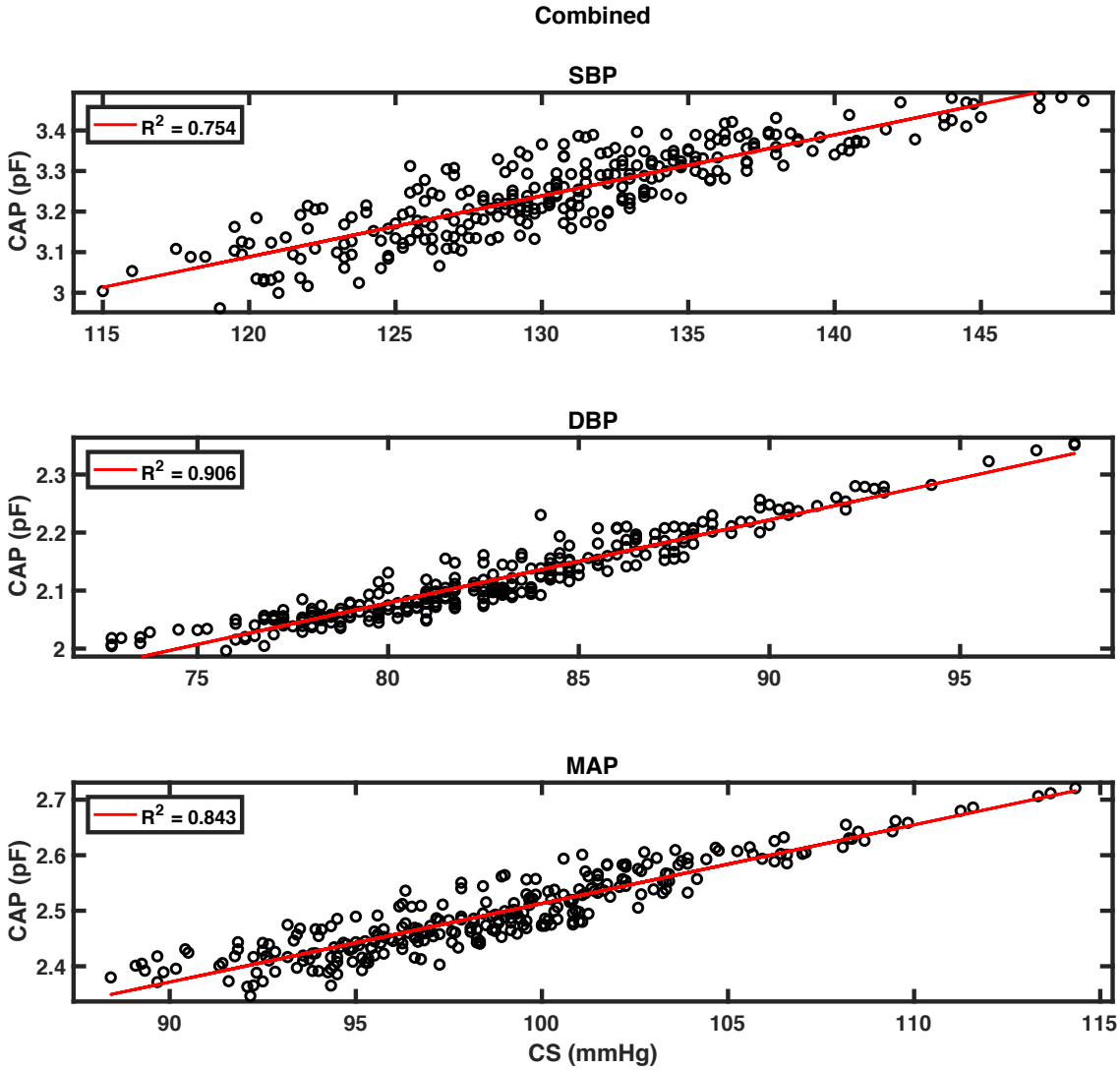
Combined
SBP
R2 = 0.754
CAP (pF)
3.4
3.3
3.2
3.1
3
115
120
125
130
135
140
145
DBP
R2 = 0.906
CAP (pF)
2.3
2.2
2.1
2
75
80
85
90
95
MAP
R2 = 0.843
CAP (pF)
2.7
2.6
2.5
2.4
90
95
100
105
110
115
CS (mmHg)

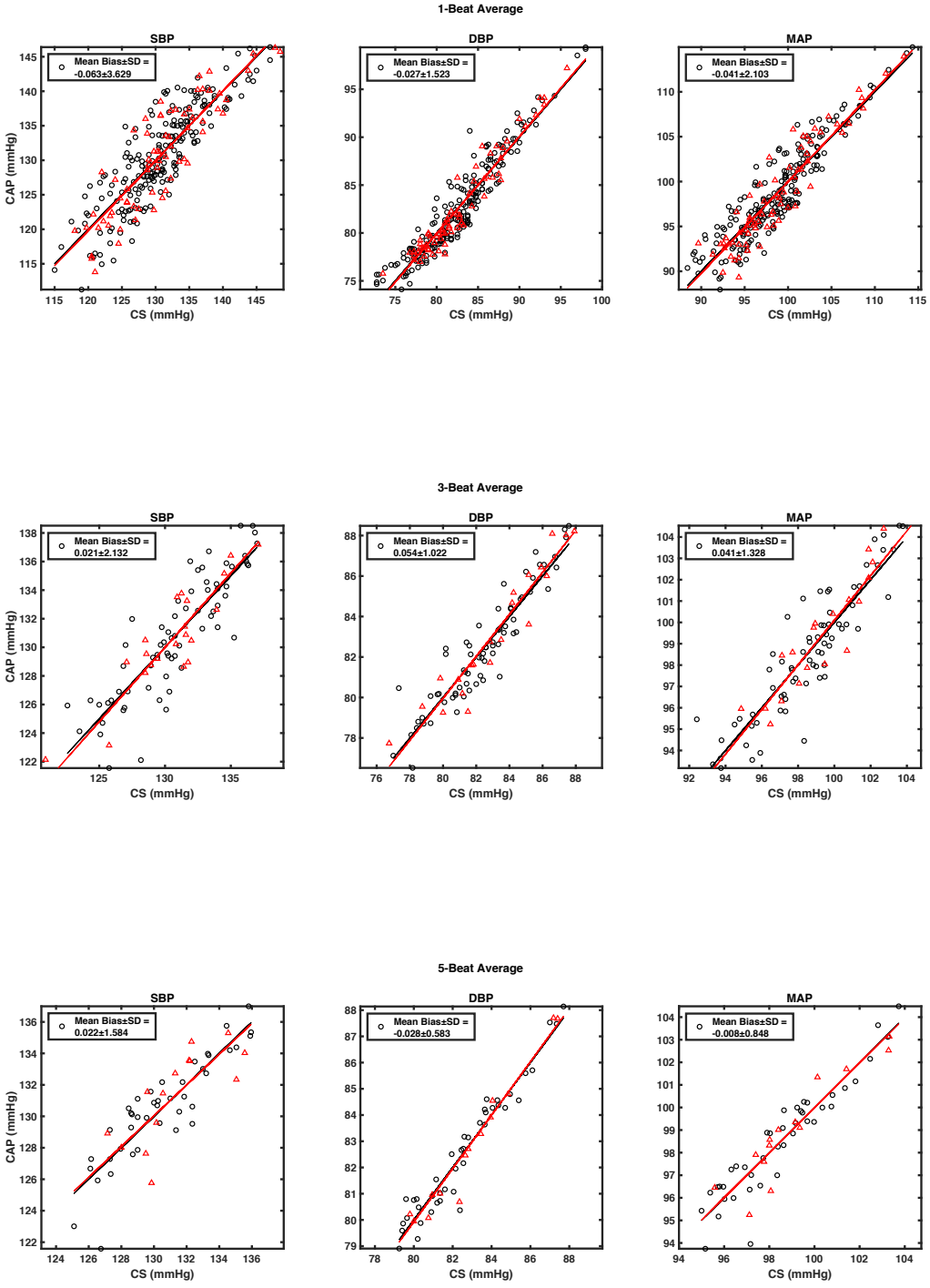
1-Beat Average
SBP
Mean Bias±SD =
-0.063±3.629
CAP (mmHg)
CS (mmHg)
DBP
Mean Bias±SD =
-0.027±1.523
CS (mmHg)
MAP
Mean Bias±SD =
-0.041±2.103
CS (mmHg)
3-Beat Average
SBP
Mean Bias±SD =
0.021±2.132
CAP (mmHg)
CS (mmHg)
DBP
Mean Bias±SD =
0.054±1.022
CS (mmHg)
MAP
Mean Bias±SD =
0.041±1.328
CS (mmHg)
5-Beat Average
SBP
Mean Bias±SD =
0.022±1.584
CAP (mmHg)
CS (mmHg)
DBP
Mean Bias±SD =
-0.028±0.583
CS (mmHg)
MAP
Mean Bias±SD =
-0.008±0.848
CS (mmHg)

7-Beat Average

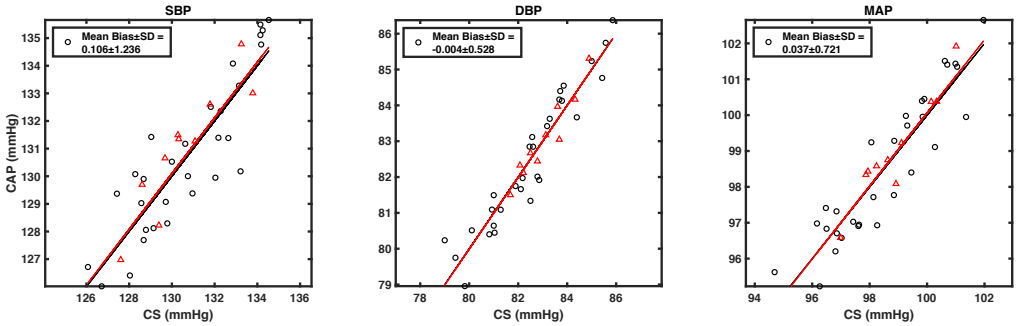

10-Beat Average

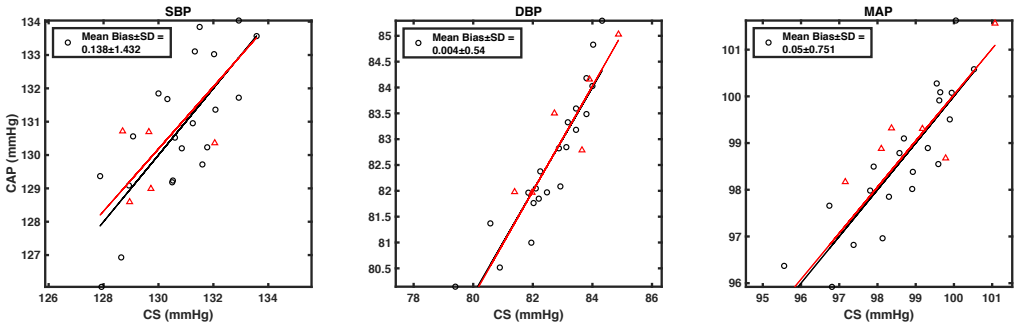

SI.2 Subject 3

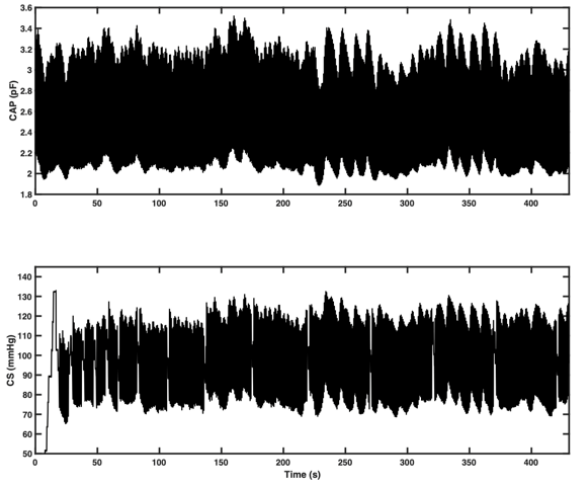

Deep (1)

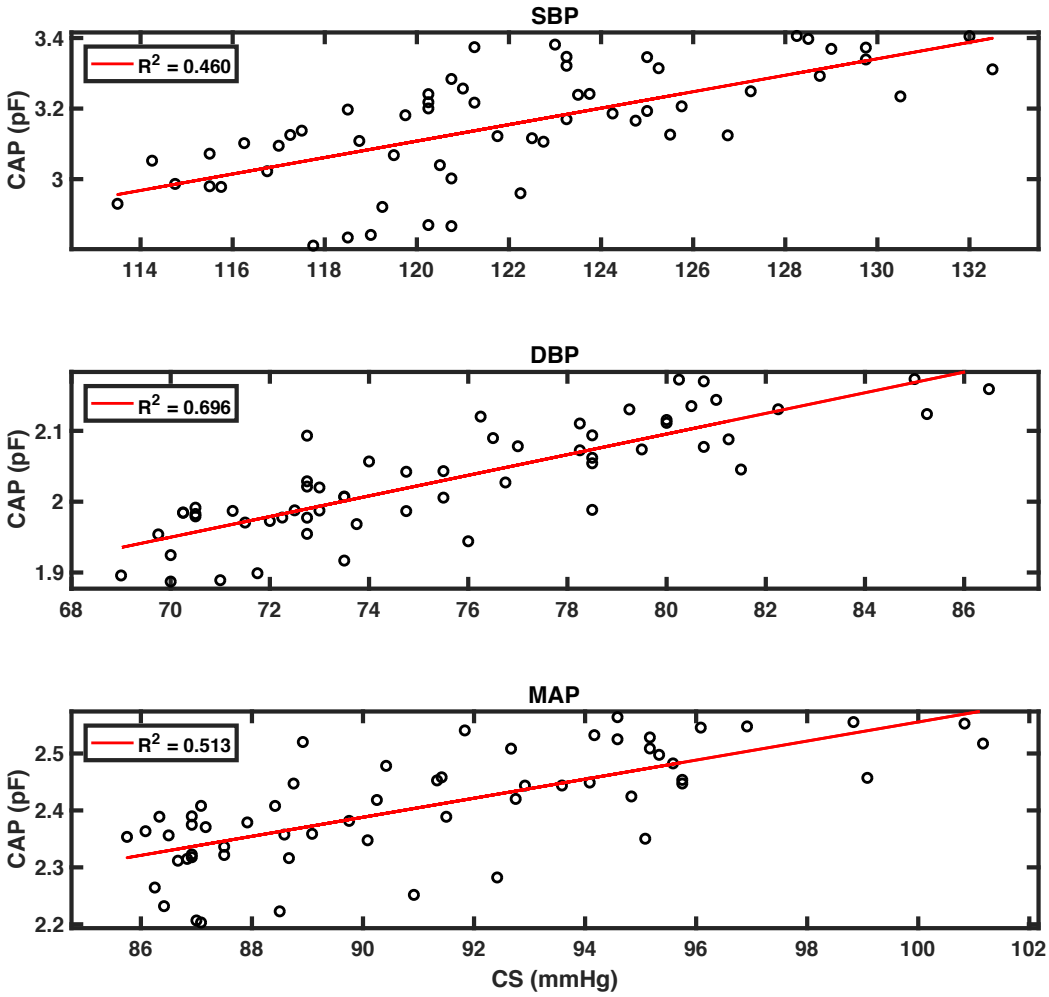

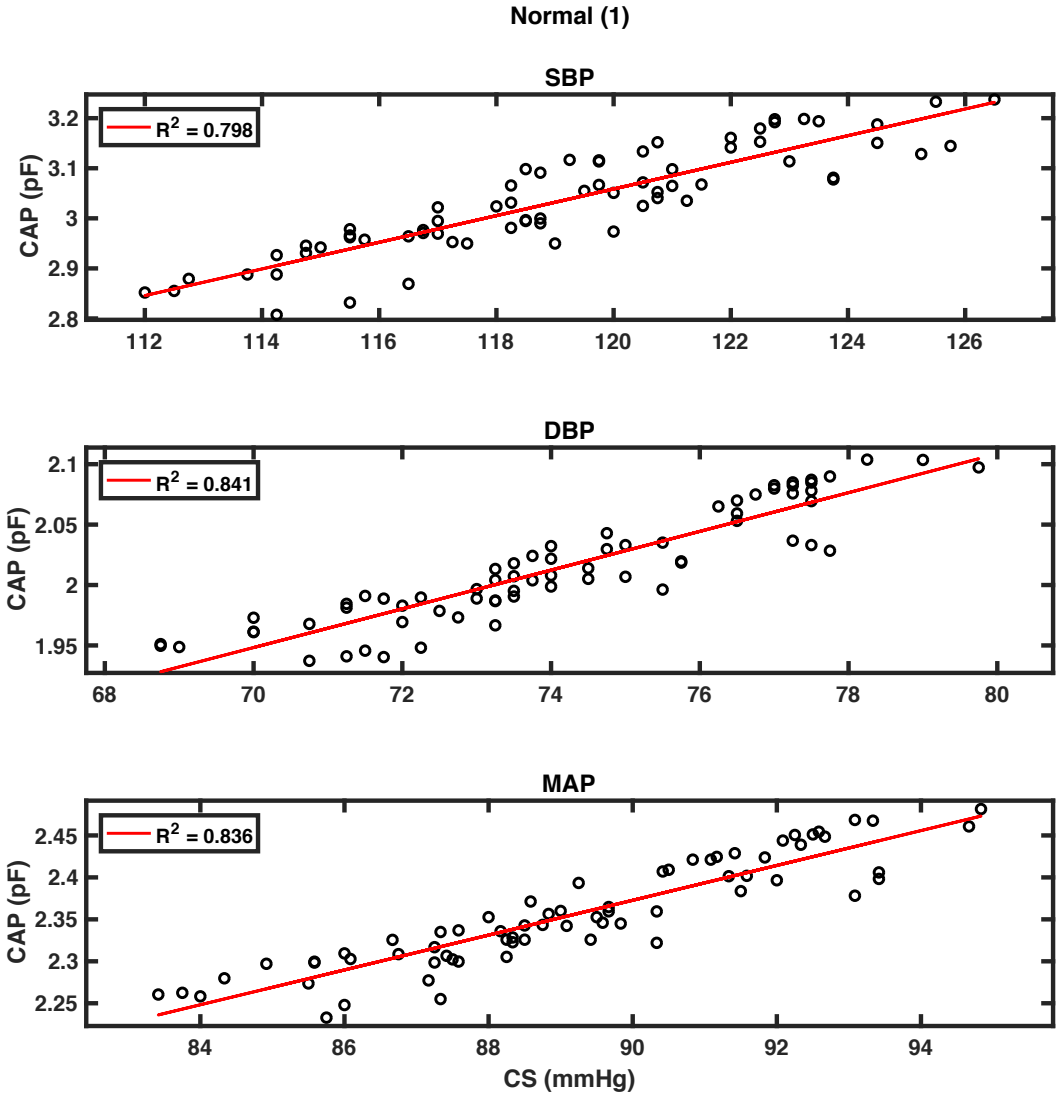
Normal (1)
SBP
R2 = 0.798
CAP (pF)
3.2
3.1
3
2.9
2.8
112
114
116
118
120
122
124
126
DBP
R2 = 0.841
CAP (pF)
2.1
2.05
2
1.95
68
70
72
74
76
78
80
MAP
R2 = 0.836
CAP (pF)
2.45
2.4
2.35
2.3
2.25
84
86
88
90
92
94
CS (mmHg)

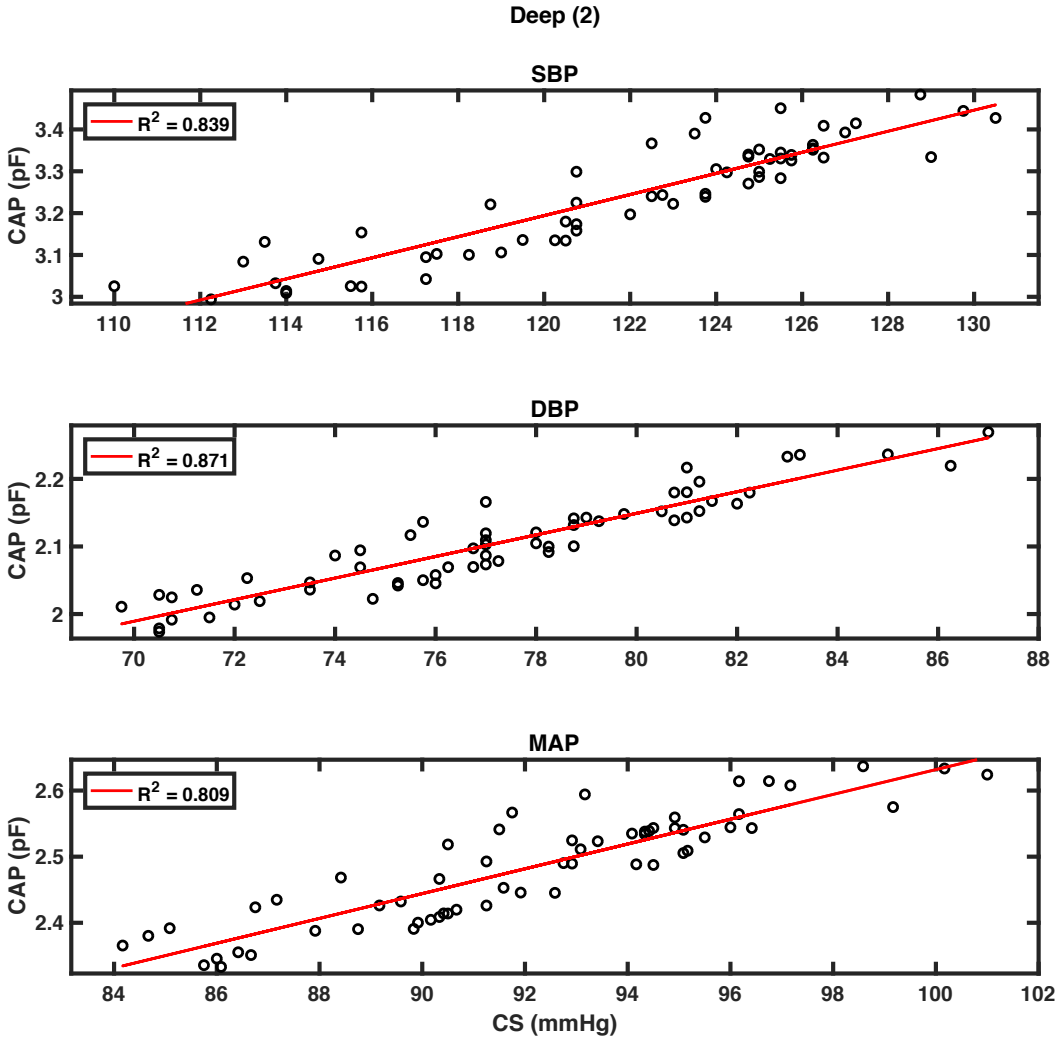
Deep (2)
SBP
R2 = 0.839
CAP (pF)
3
3.1
3.2
3.3
3.4
110
112
114
116
118
120
122
124
126
128
130
DBP
R2 = 0.871
CAP (pF)
2
2.1
2.2
70
72
74
76
78
80
82
84
86
88
MAP
R2 = 0.809
CAP (pF)
2.4
2.5
2.6
84
86
88
90
92
94
96
98
100
102
CS (mmHg)

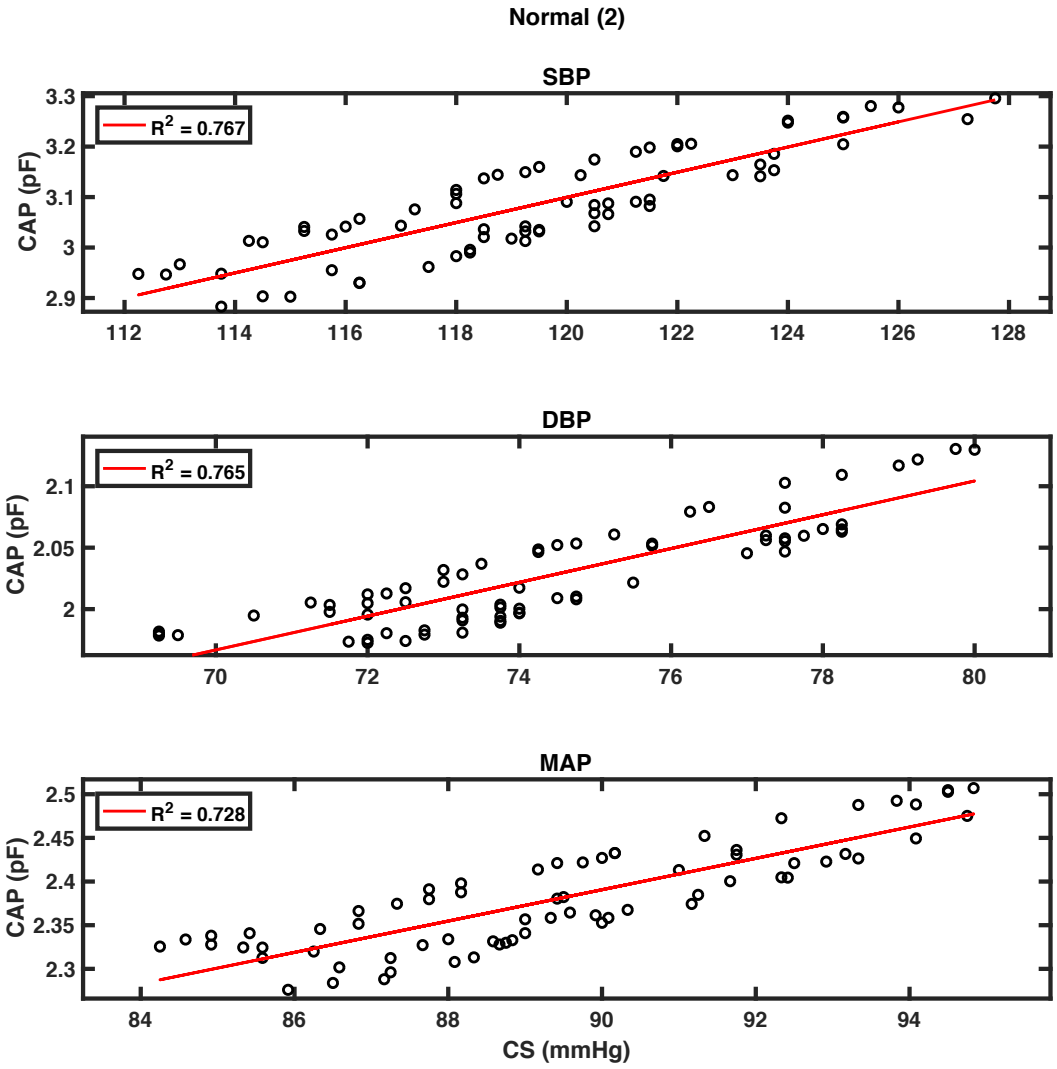
Normal (2)
SBP
R2 = 0.767
CAP (pF)
3.3
3.2
3.1
3
2.9
112
114
116
118
120
122
124
126
128
DBP
R2 = 0.765
CAP (pF)
2.1
2.05
2
70
72
74
76
78
80
MAP
R2 = 0.728
CAP (pF)
2.5
2.45
2.4
2.35
2.3
84
86
88
90
92
94
CS (mmHg)

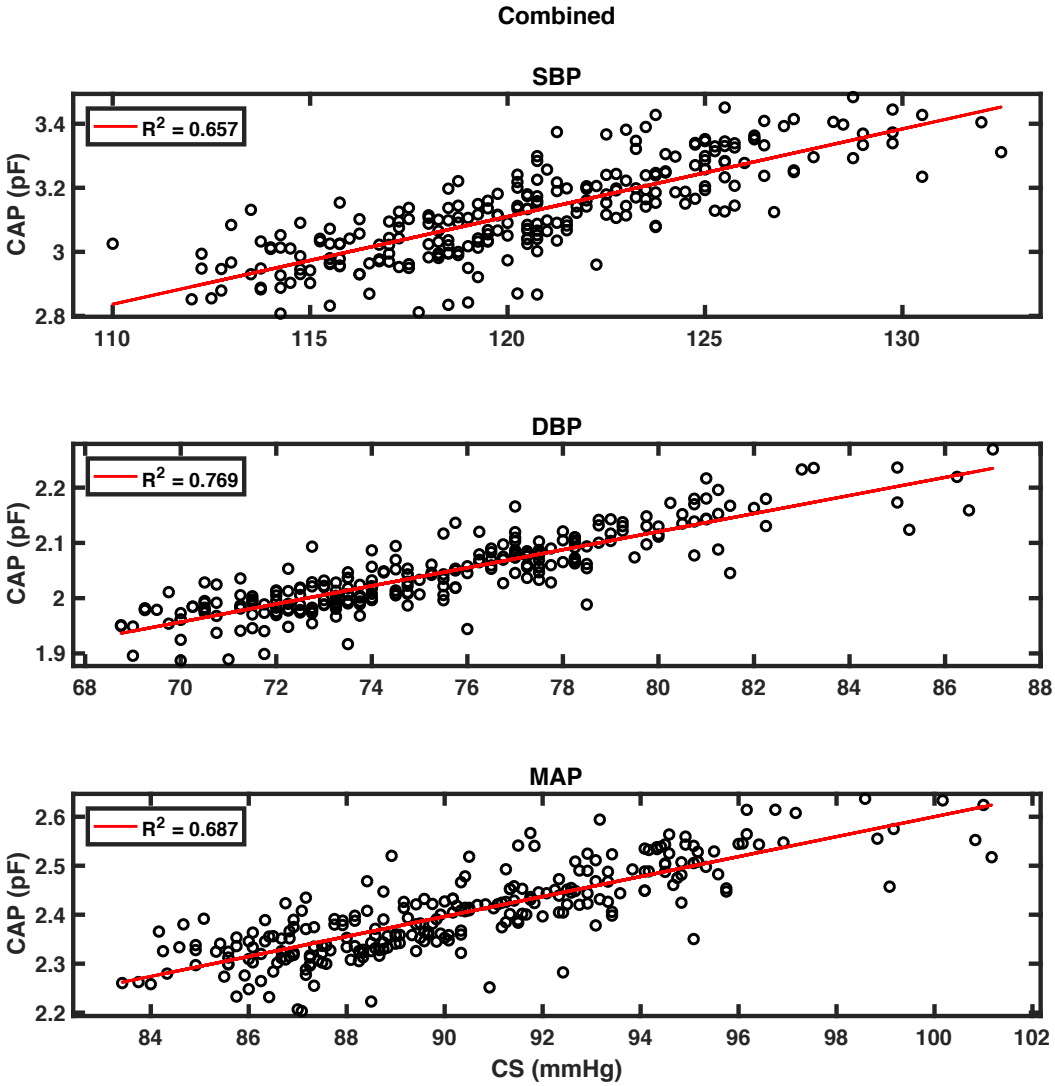
Combined
SBP
R2 = 0.657
CAP (pF)
3.4
3.2
3
2.8
110
115
120
125
130
DBP
R2 = 0.769
CAP (pF)
2.2
2.1
2
1.9
68
70
72
74
76
78
80
82
84
86
88
MAP
R2 = 0.687
CAP (pF)
2.6
2.5
2.4
2.3
2.2
84
86
88
90
92
94
96
98
100
102
CS (mmHg)

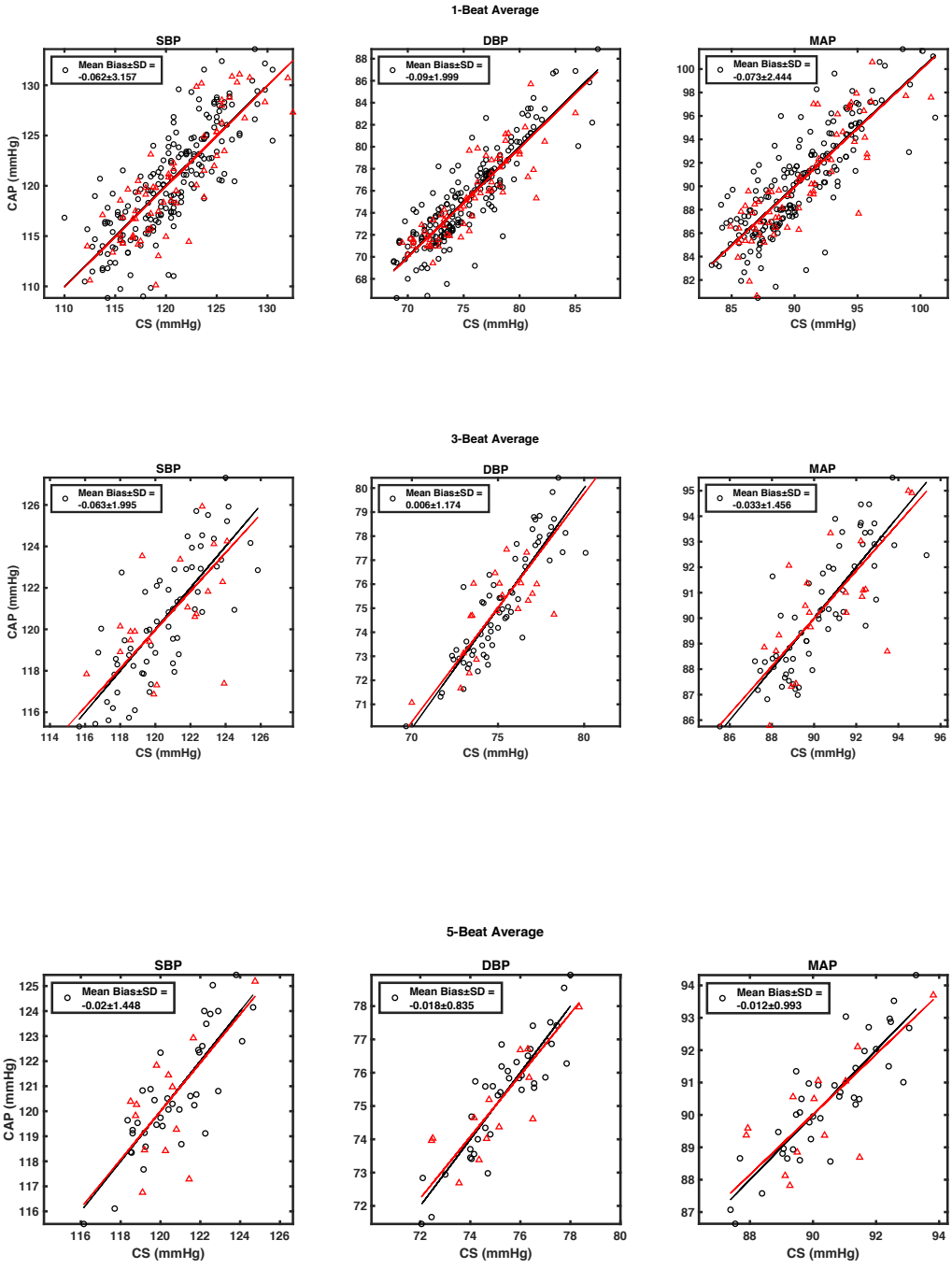
1-Beat Average
SBP
Mean Bias±SD =
-0.062±3.157
DBP
Mean Bias±SD =
-0.09±1.999
MAP
Mean Bias±SD =
-0.073±2.444
CAP (mmHg)
CS (mmHg)
3-Beat Average
SBP
Mean Bias±SD =
-0.063±1.995
DBP
Mean Bias±SD =
0.006±1.174
MAP
Mean Bias±SD =
-0.033±1.456
CAP (mmHg)
CS (mmHg)
5-Beat Average
SBP
Mean Bias±SD =
-0.02±1.448
DBP
Mean Bias±SD =
-0.018±0.835
MAP
Mean Bias±SD =
-0.012±0.993
CAP (mmHg)
CS (mmHg)

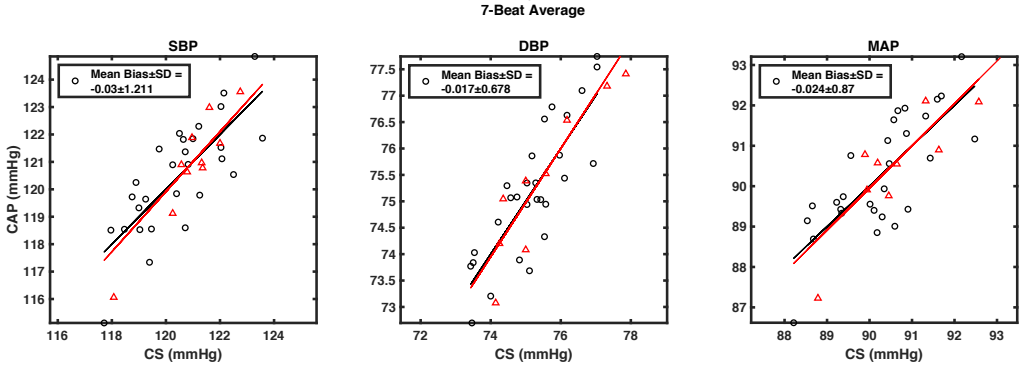
7-Beat Average
SBP
Mean Bias±SD =
-0.03±1.211
DBP
Mean Bias±SD =
-0.017±0.678
MAP
Mean Bias±SD =
-0.024±0.87
CAP (mmHg)
CS (mmHg)
CS (mmHg)
CS (mmHg)

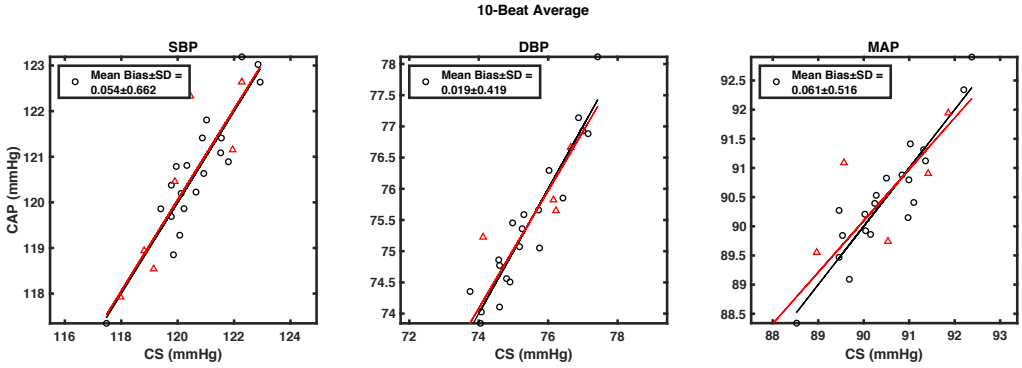
10-Beat Average
SBP
Mean Bias±SD =
0.054±0.662
DBP
Mean Bias±SD =
0.019±0.419
MAP
Mean Bias±SD =
0.061±0.516
CAP (mmHg)
CS (mmHg)
CS (mmHg)
CS (mmHg)

SI.3 Subject 4

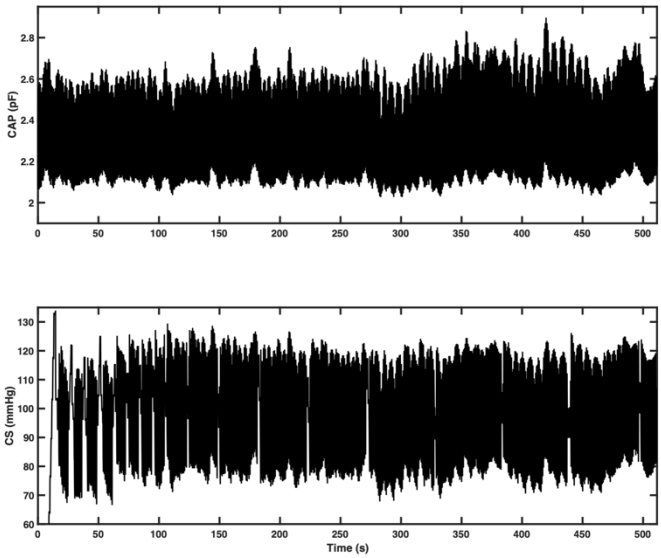

Deep (1)

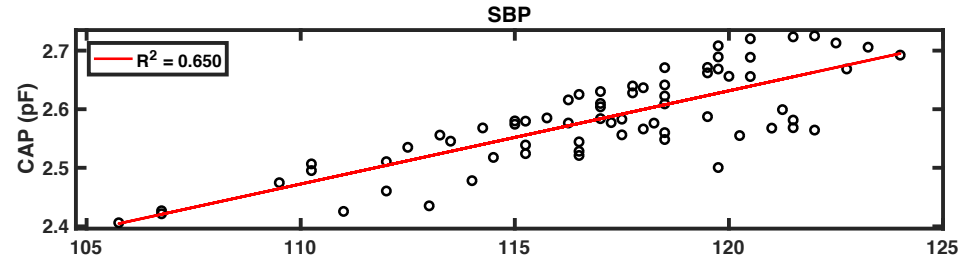

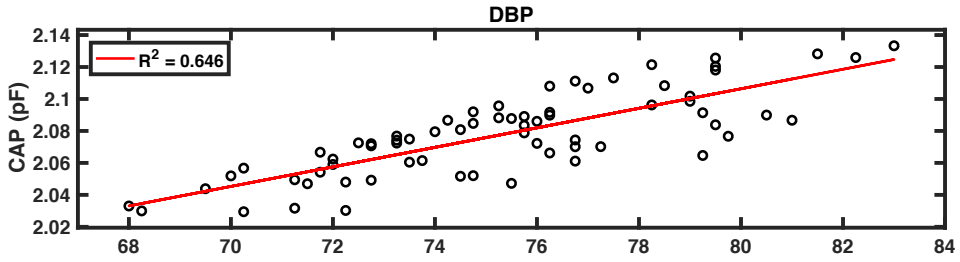

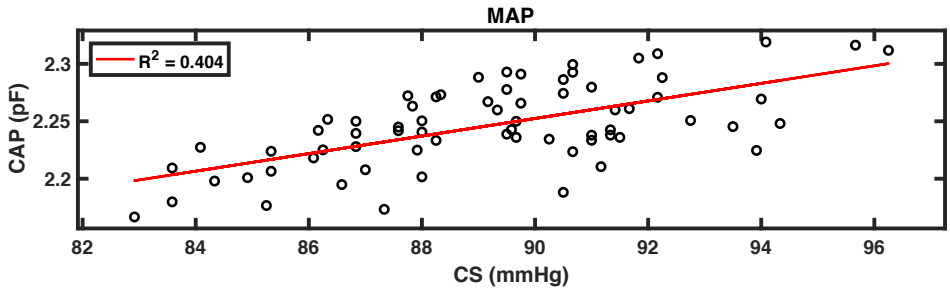

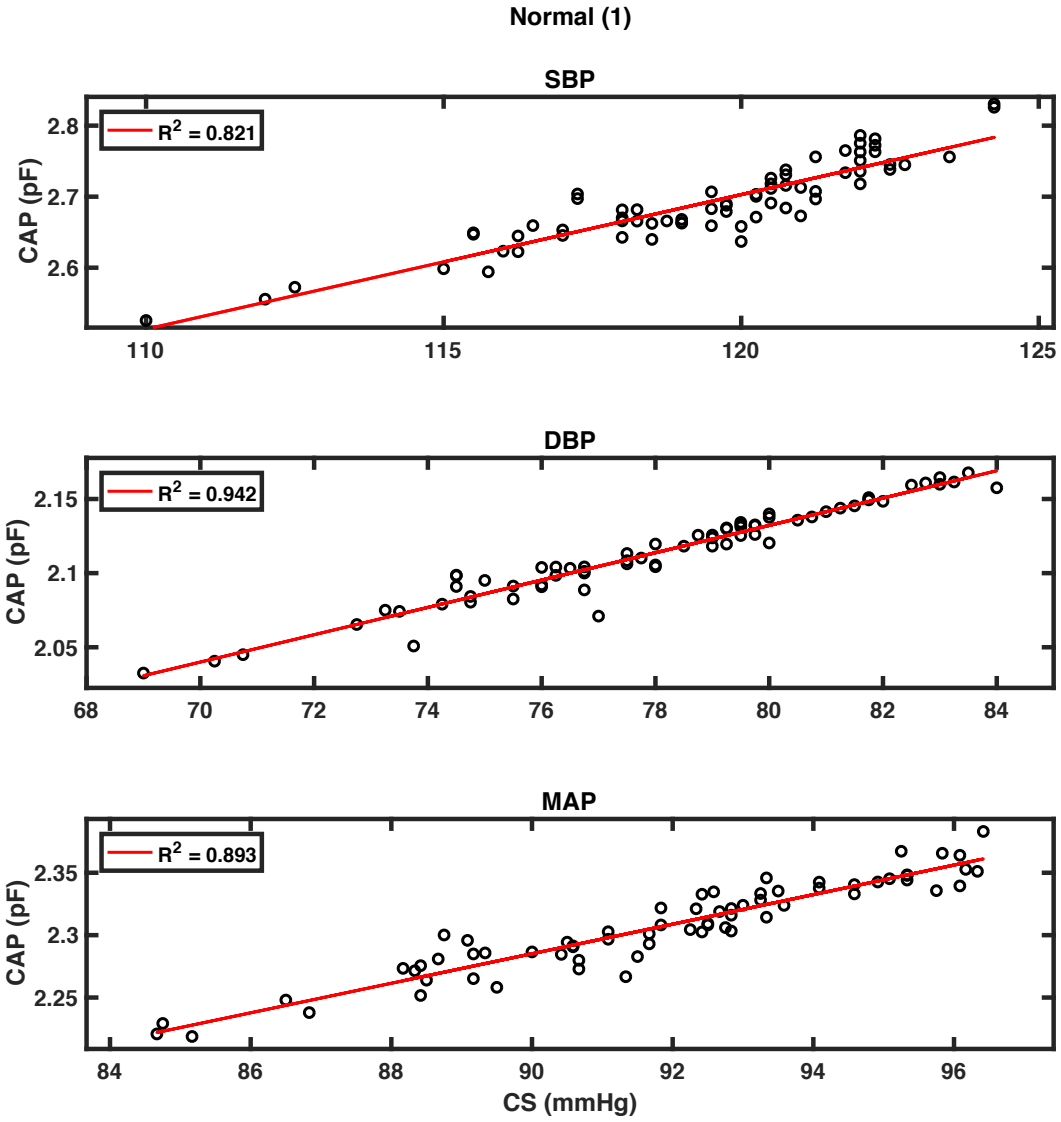
Normal (1)
SBP
R2 = 0.821
CAP (pF)
2.8
2.7
2.6
110
115
120
125
DBP
R2 = 0.942
CAP (pF)
2.15
2.1
2.05
68
70
72
74
76
78
80
82
84
MAP
R2 = 0.893
CAP (pF)
2.35
2.3
2.25
84
86
88
90
92
94
96
CS (mmHg)

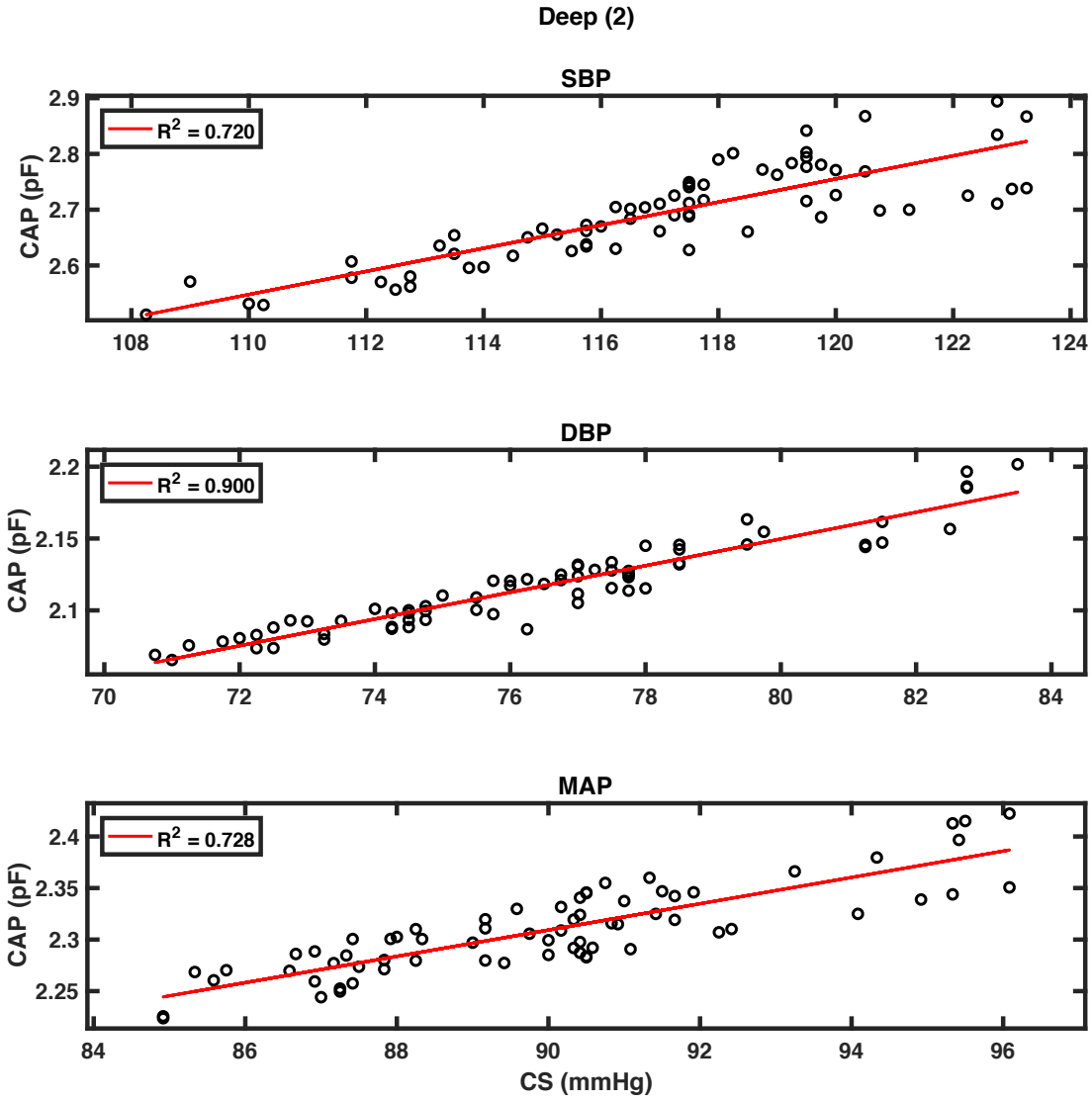
Deep (2)
SBP
R2 = 0.720
CAP (pF)
2.9
2.8
2.7
2.6
108
110
112
114
116
118
120
122
124
DBP
R2 = 0.900
CAP (pF)
2.2
2.15
2.1
70
72
74
76
78
80
82
84
MAP
R2 = 0.728
CAP (pF)
2.4
2.35
2.3
2.25
84
86
88
90
92
94
96
CS (mmHg)

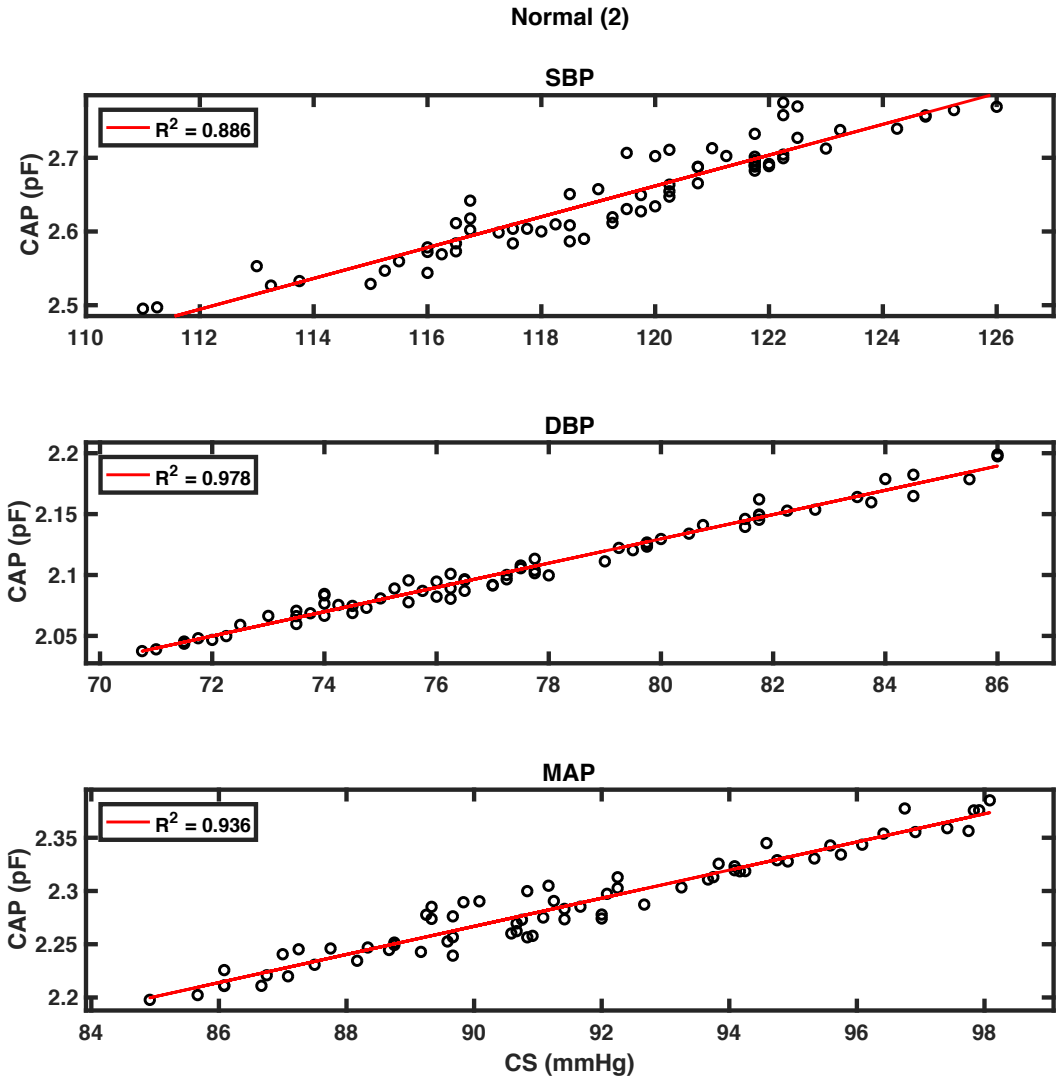
Normal (2)
SBP
R2 = 0.886
CAP (pF)
2.5
2.6
2.7
110
112
114
116
118
120
122
124
126
DBP
R2 = 0.978
CAP (pF)
2.05
2.1
2.15
2.2
70
72
74
76
78
80
82
84
86
MAP
R2 = 0.936
CAP (pF)
2.2
2.25
2.3
2.35
84
86
88
90
92
94
96
98
CS (mmHg)

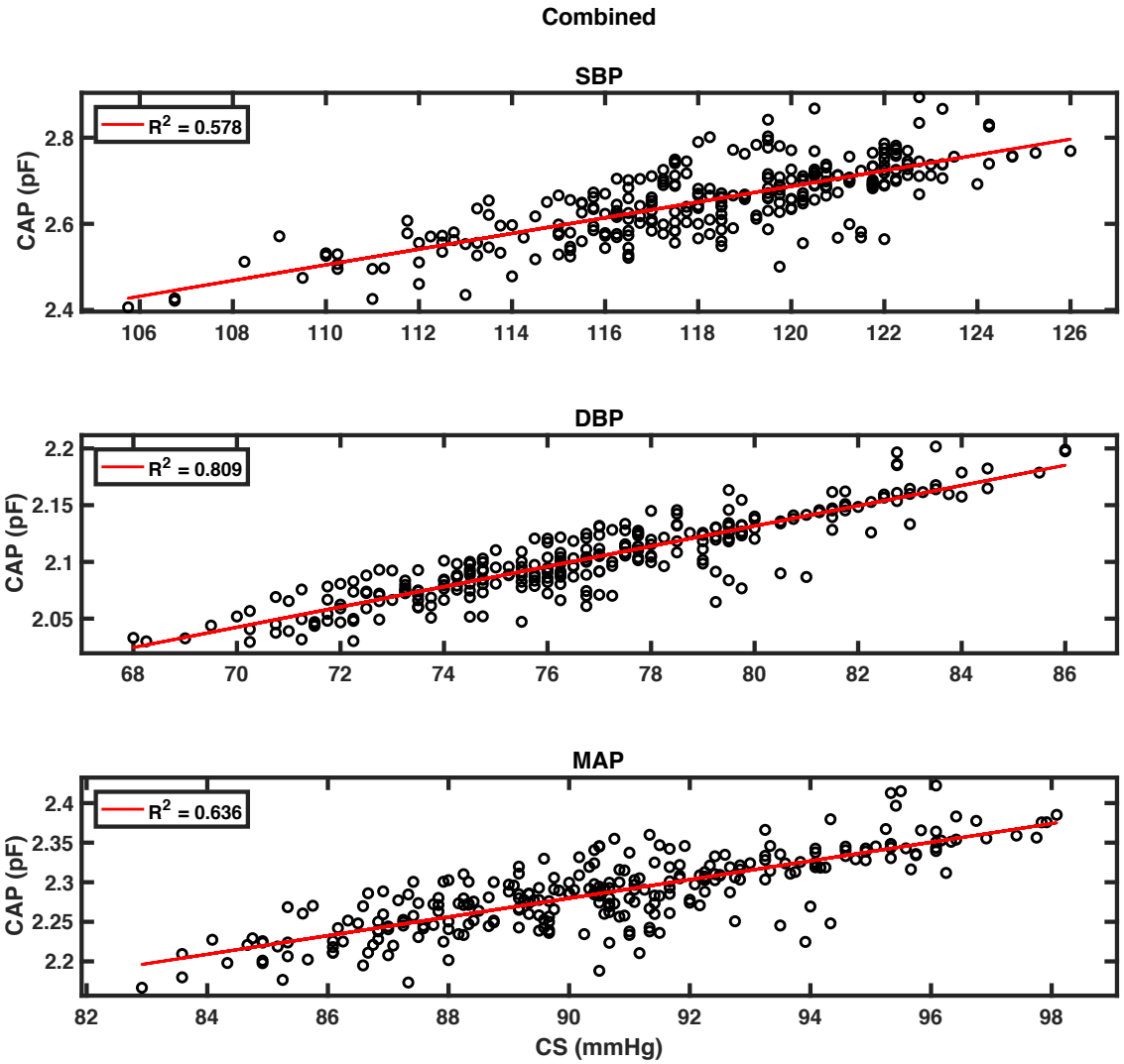
Combined
SBP
R2 = 0.578
CAP (pF)
2.8
2.6
2.4
106
108
110
112
114
116
118
120
122
124
126
DBP
R2 = 0.809
CAP (pF)
2.2
2.15
2.1
2.05
68
70
72
74
76
78
80
82
84
86
MAP
R2 = 0.636
CAP (pF)
2.4
2.35
2.3
2.25
2.2
82
84
86
88
90
92
94
96
98
CS (mmHg)

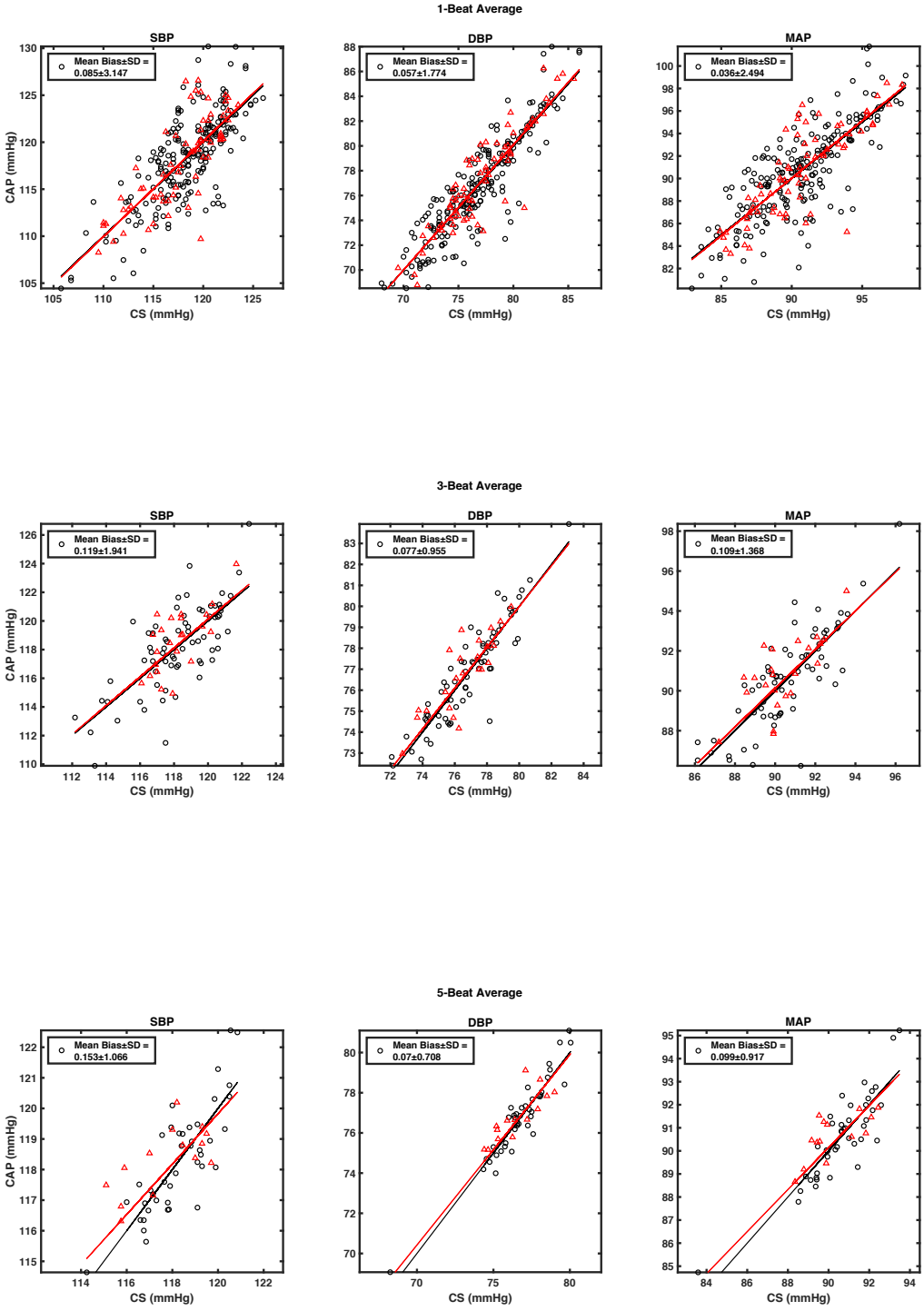
1-Beat Average
SBP
Mean Bias±SD =
0.085±3.147
CAP (mmHg)
CS (mmHg)
DBP
Mean Bias±SD =
0.057±1.774
CS (mmHg)
MAP
Mean Bias±SD =
0.036±2.494
CS (mmHg)
3-Beat Average
SBP
Mean Bias±SD =
0.119±1.941
CAP (mmHg)
CS (mmHg)
DBP
Mean Bias±SD =
0.077±0.955
CS (mmHg)
MAP
Mean Bias±SD =
0.109±1.368
CS (mmHg)
5-Beat Average
SBP
Mean Bias±SD =
0.153±1.066
CAP (mmHg)
CS (mmHg)
DBP
Mean Bias±SD =
0.07±0.708
CS (mmHg)
MAP
Mean Bias±SD =
0.099±0.917
CS (mmHg)

SI.4 Subject 5

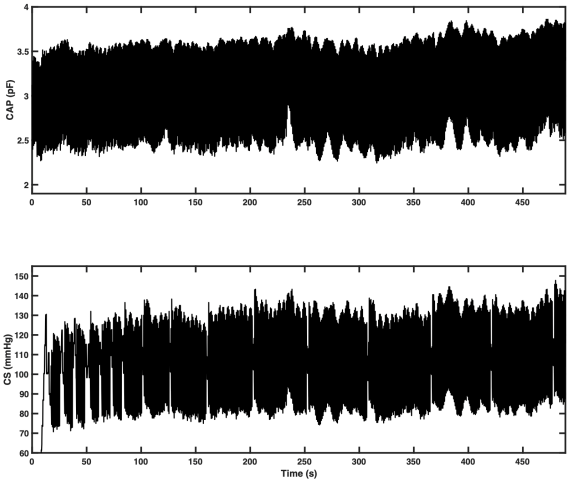

Deep (1)

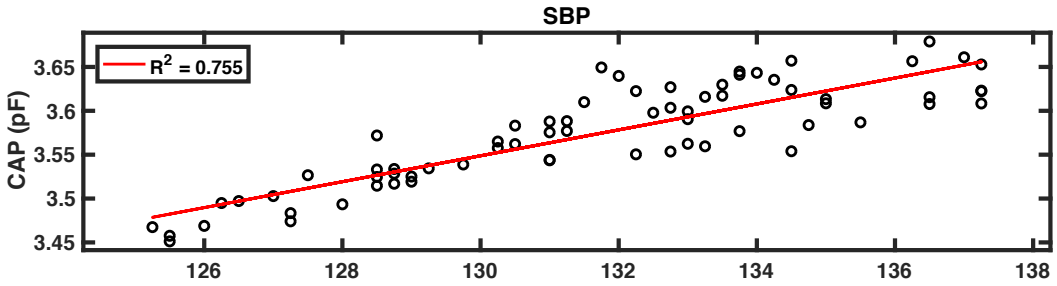

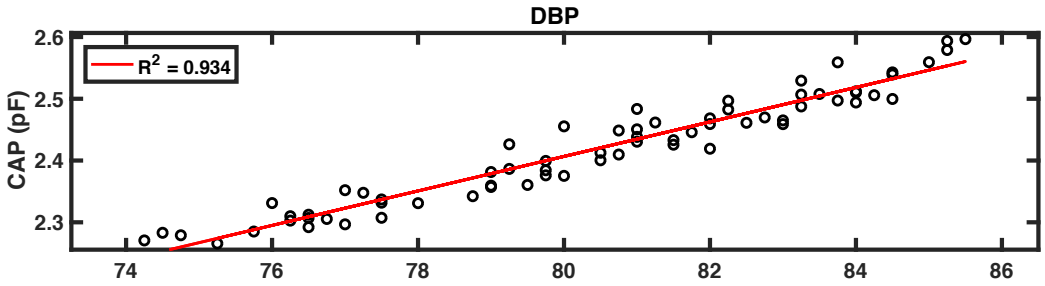

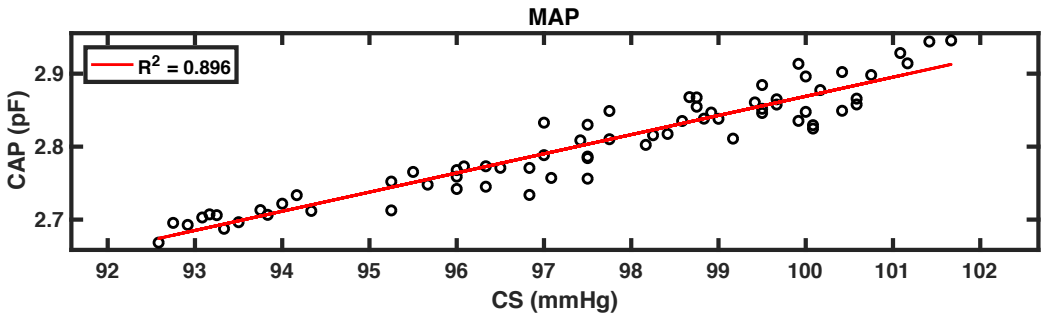

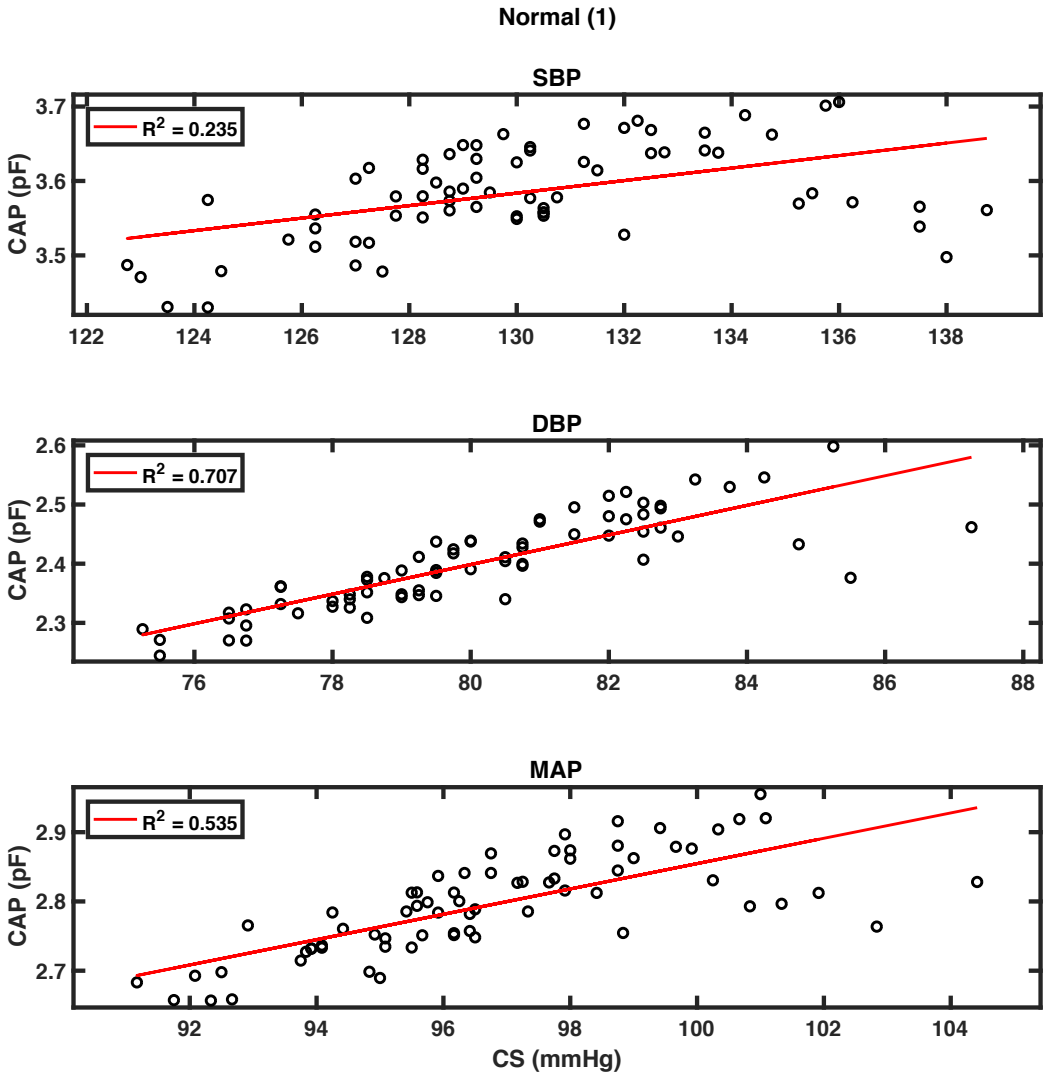
Normal (1)
SBP
R2 = 0.235
CAP (pF)
3.7
3.6
3.5
122
124
126
128
130
132
134
136
138
DBP
R2 = 0.707
CAP (pF)
2.6
2.5
2.4
2.3
76
78
80
82
84
86
88
MAP
R2 = 0.535
CAP (pF)
2.9
2.8
2.7
92
94
96
98
100
102
104
CS (mmHg)

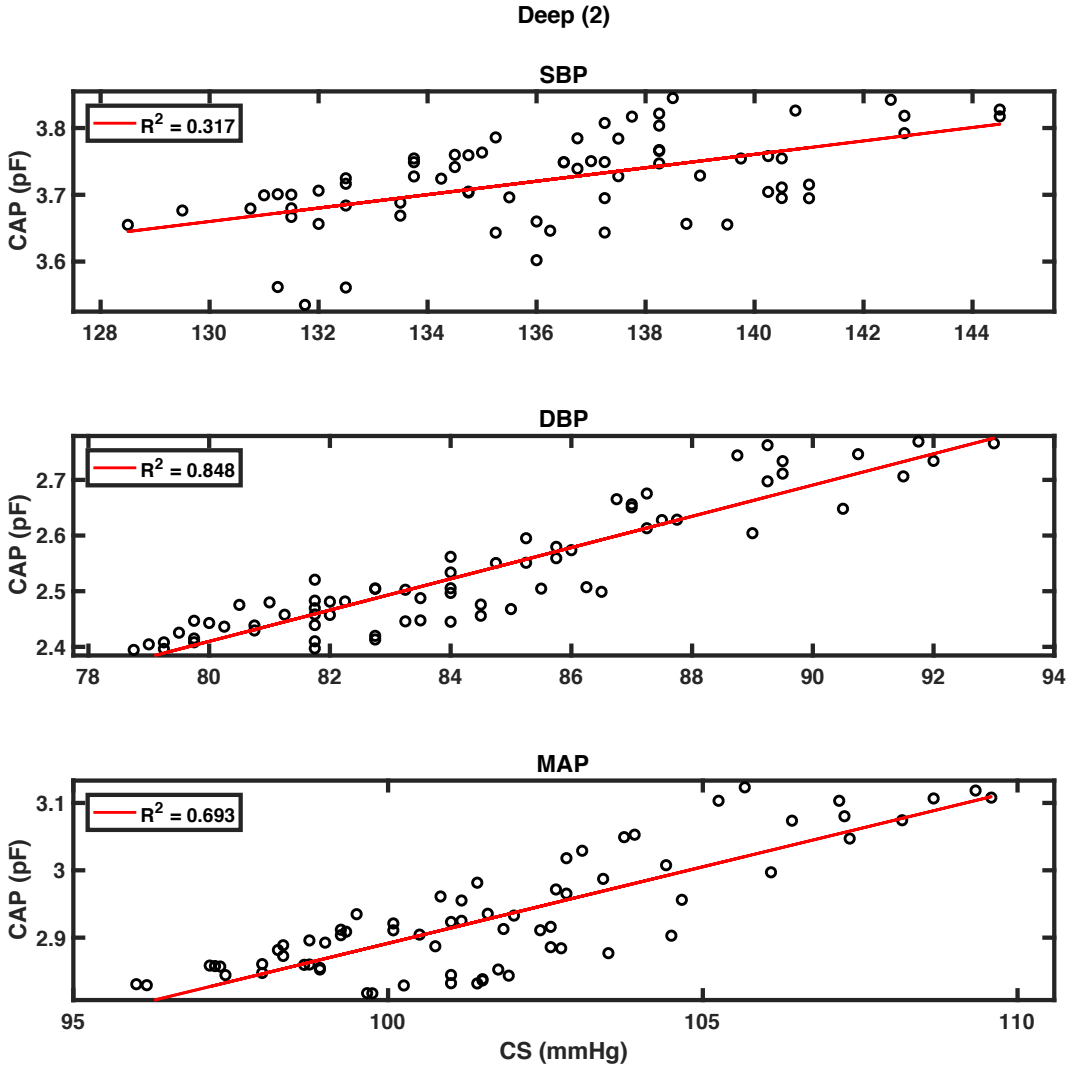
Deep (2)
SBP
R2 = 0.317
CAP (pF)
3.8
3.7
3.6
128
130
132
134
136
138
140
142
144
DBP
R2 = 0.848
CAP (pF)
2.7
2.6
2.5
2.4
78
80
82
84
86
88
90
92
94
MAP
R2 = 0.693
CAP (pF)
3.1
3
2.9
95
100
105
110
CS (mmHg)

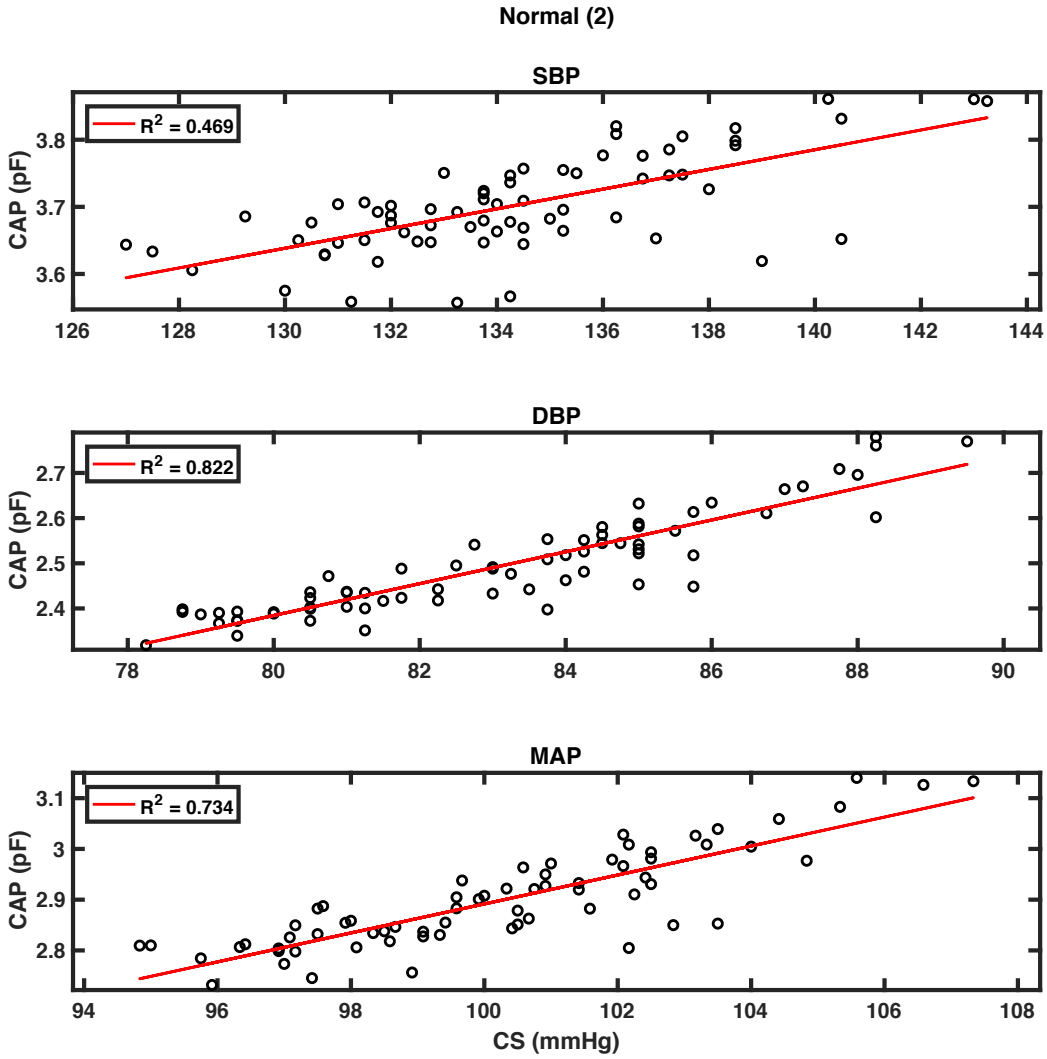
Normal (2)
SBP
R2 = 0.469
CAP (pF)
3.8
3.7
3.6
126
128
130
132
134
136
138
140
142
144
DBP
R2 = 0.822
CAP (pF)
2.7
2.6
2.5
2.4
78
80
82
84
86
88
90
MAP
R2 = 0.734
CAP (pF)
3.1
3
2.9
2.8
94
96
98
100
102
104
106
108
CS (mmHg)

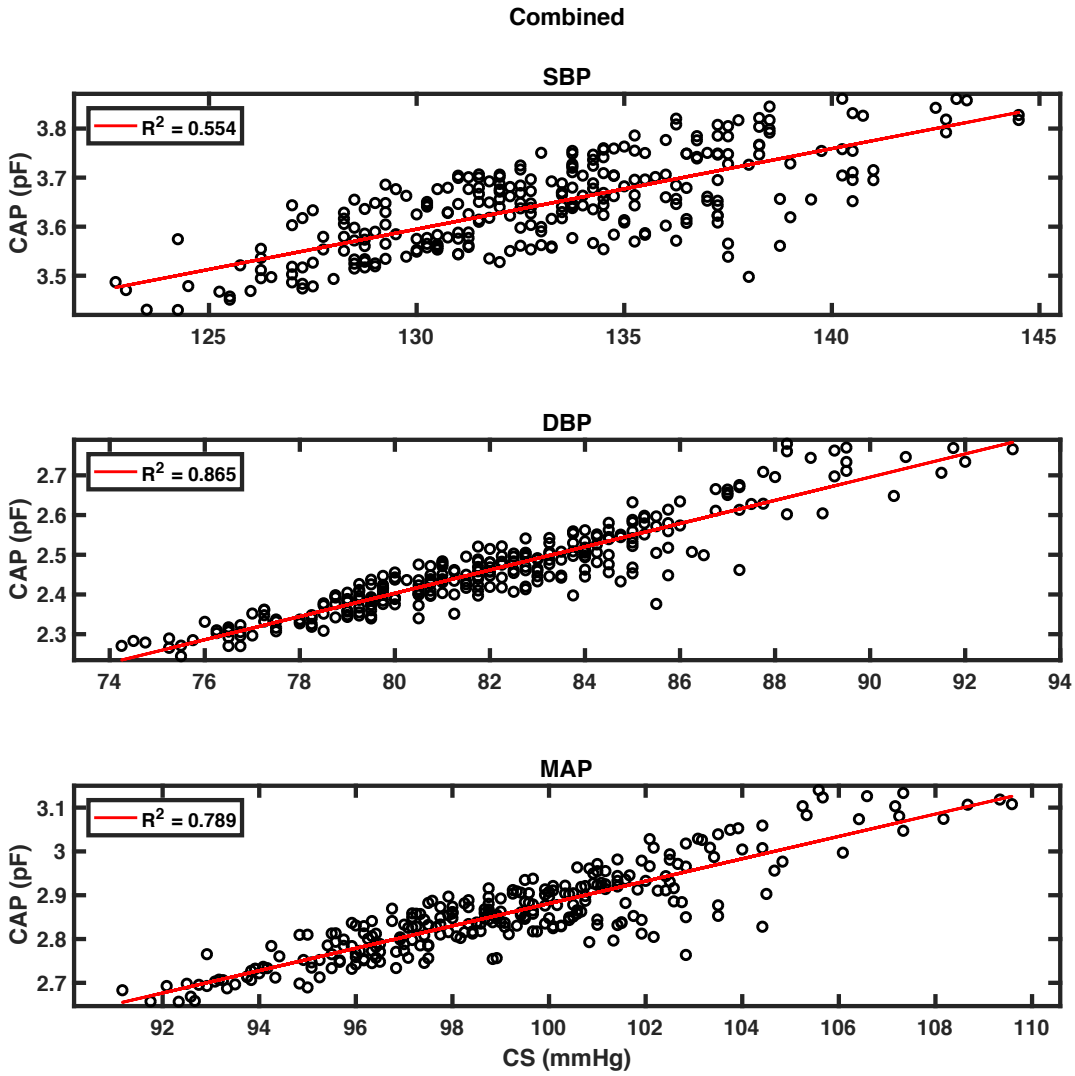
Combined
SBP
R2 = 0.554
CAP (pF)
3.8
3.7
3.6
3.5
125
130
135
140
145
DBP
R2 = 0.865
CAP (pF)
2.7
2.6
2.5
2.4
2.3
74
76
78
80
82
84
86
88
90
92
94
MAP
R2 = 0.789
CAP (pF)
3.1
3
2.9
2.8
2.7
92
94
96
98
100
102
104
106
108
110
CS (mmHg)

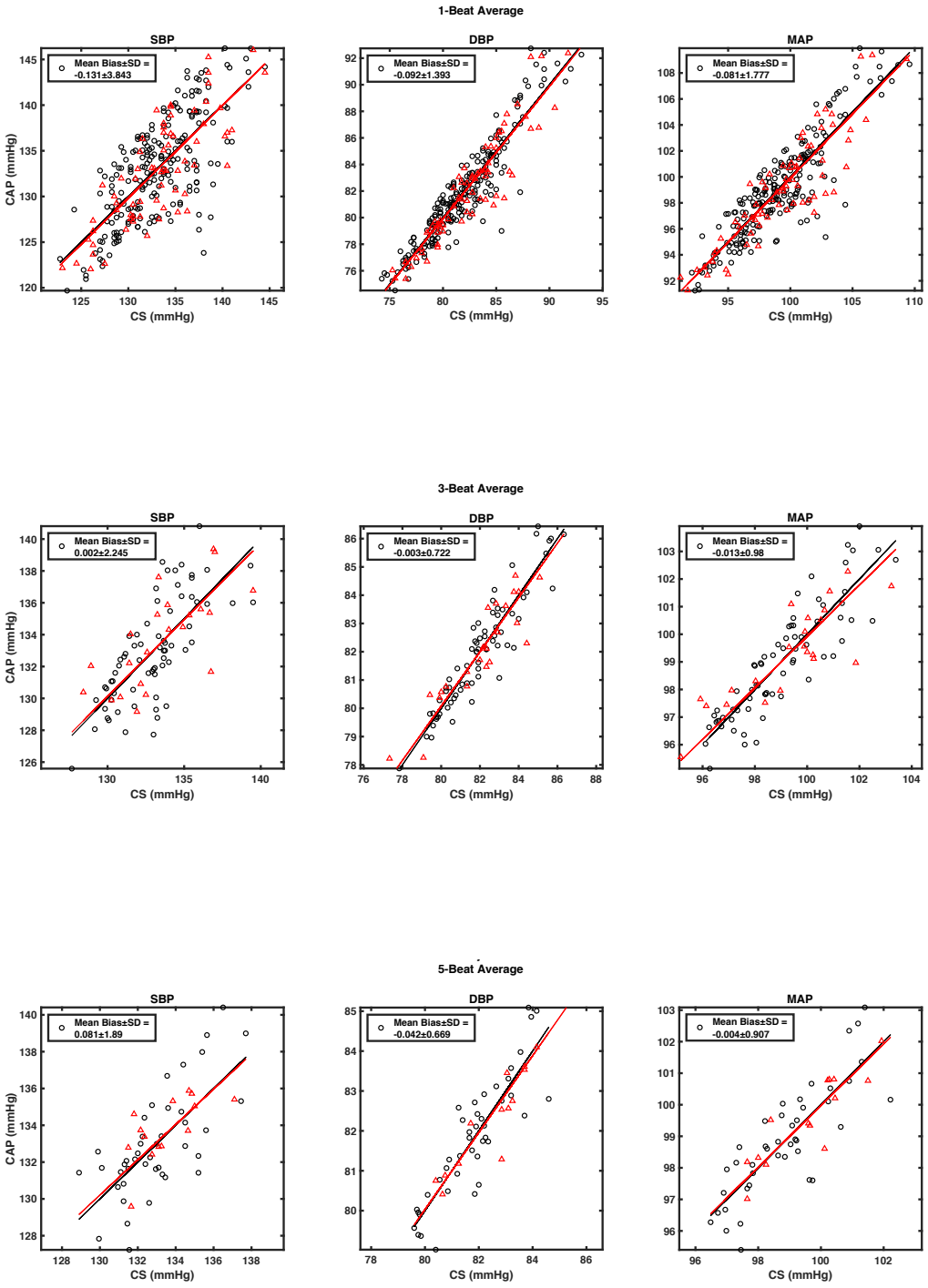
1-Beat Average
SBP
Mean Bias±SD =
-0.131±3.843
CAP (mmHg)
CS (mmHg)
DBP
Mean Bias±SD =
-0.092±1.393
CS (mmHg)
MAP
Mean Bias±SD =
-0.081±1.777
CS (mmHg)
3-Beat Average
SBP
Mean Bias±SD =
0.002±2.245
CAP (mmHg)
CS (mmHg)
DBP
Mean Bias±SD =
-0.003±0.722
CS (mmHg)
MAP
Mean Bias±SD =
-0.013±0.98
CS (mmHg)
5-Beat Average
SBP
Mean Bias±SD =
0.081±1.89
CAP (mmHg)
CS (mmHg)
DBP
Mean Bias±SD =
-0.042±0.669
CS (mmHg)
MAP
Mean Bias±SD =
-0.004±0.907
CS (mmHg)

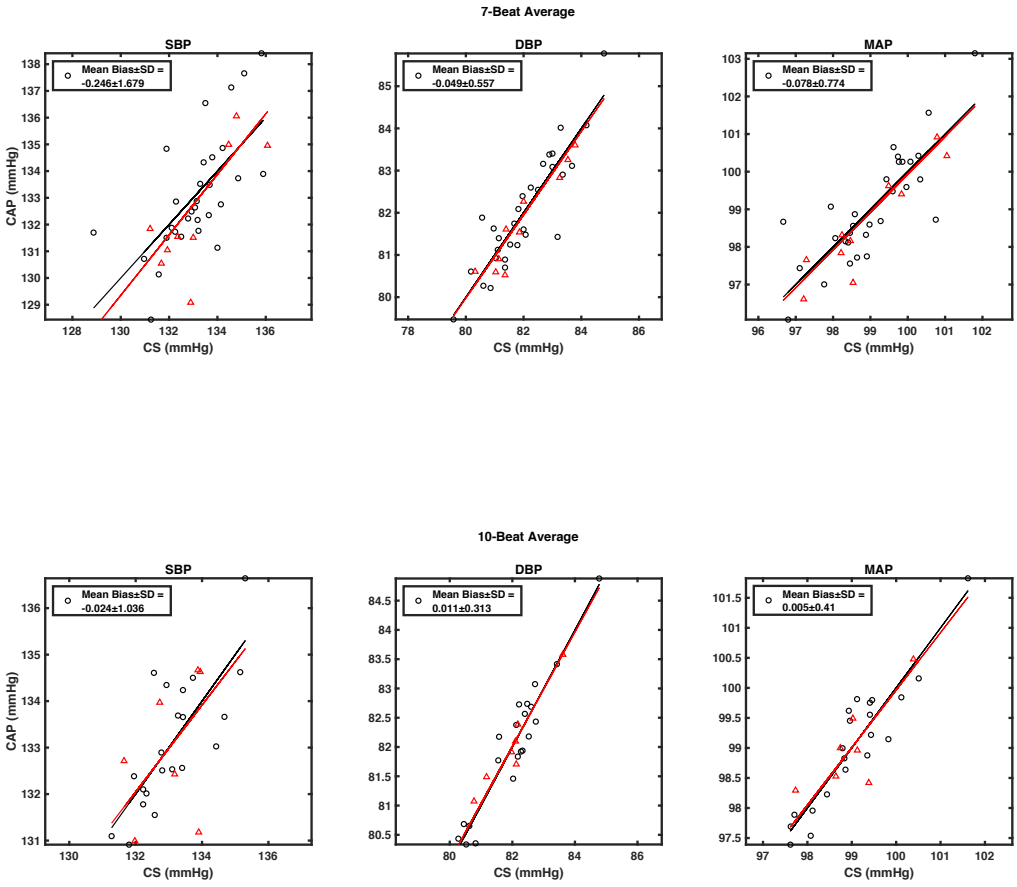
7-Beat Average
SBP
Mean Bias±SD =
-0.246±1.679
CAP (mmHg)
CS (mmHg)
DBP
Mean Bias±SD =
-0.049±0.557
CS (mmHg)
MAP
Mean Bias±SD =
-0.078±0.774
CS (mmHg)
10-Beat Average
SBP
Mean Bias±SD =
-0.024±1.036
CAP (mmHg)
CS (mmHg)
DBP
Mean Bias±SD =
0.011±0.313
CS (mmHg)
MAP
Mean Bias±SD =
0.005±0.41
CS (mmHg)

SI.5 Subject 6

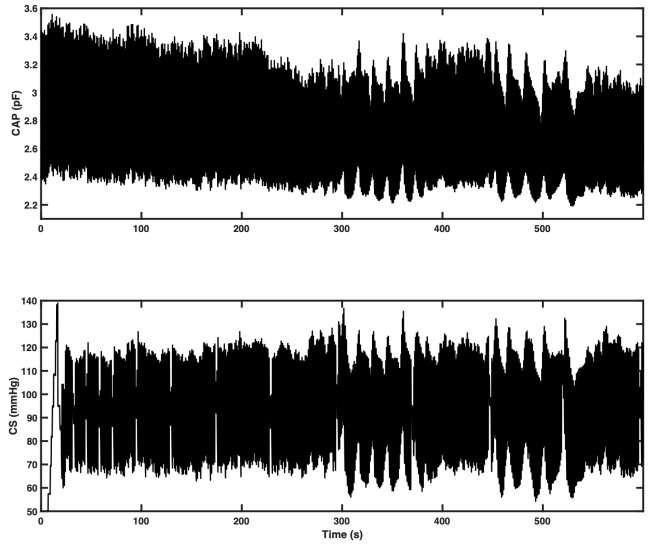

Deep (1)

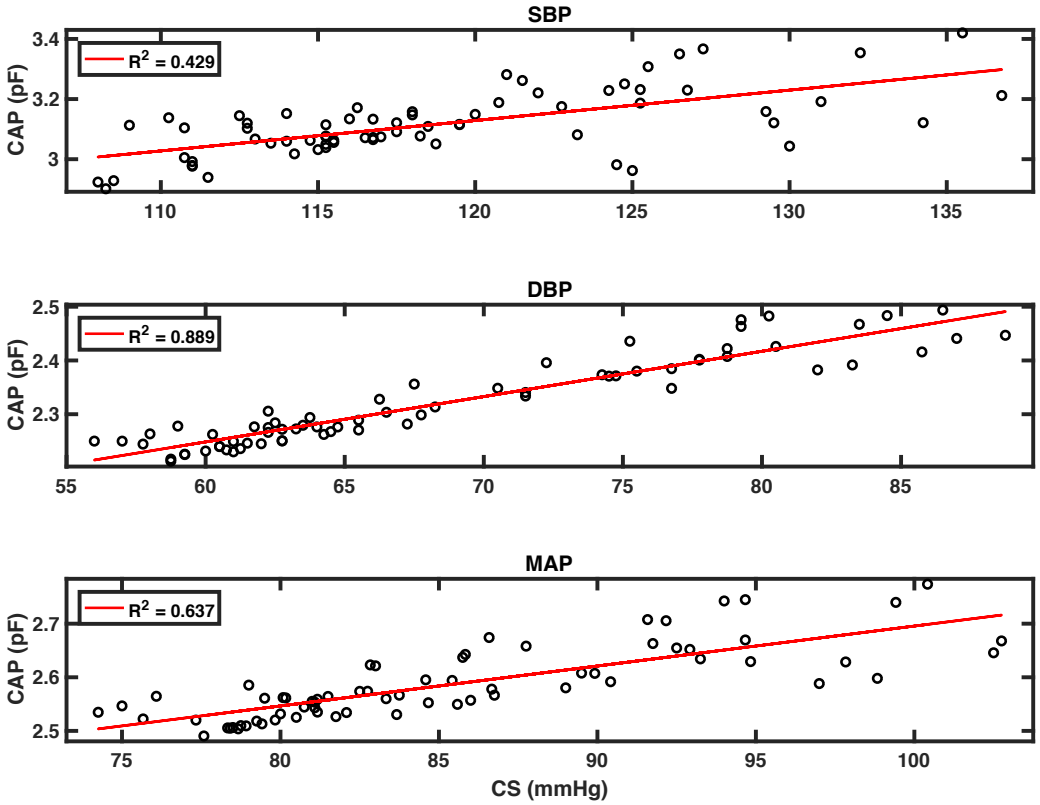

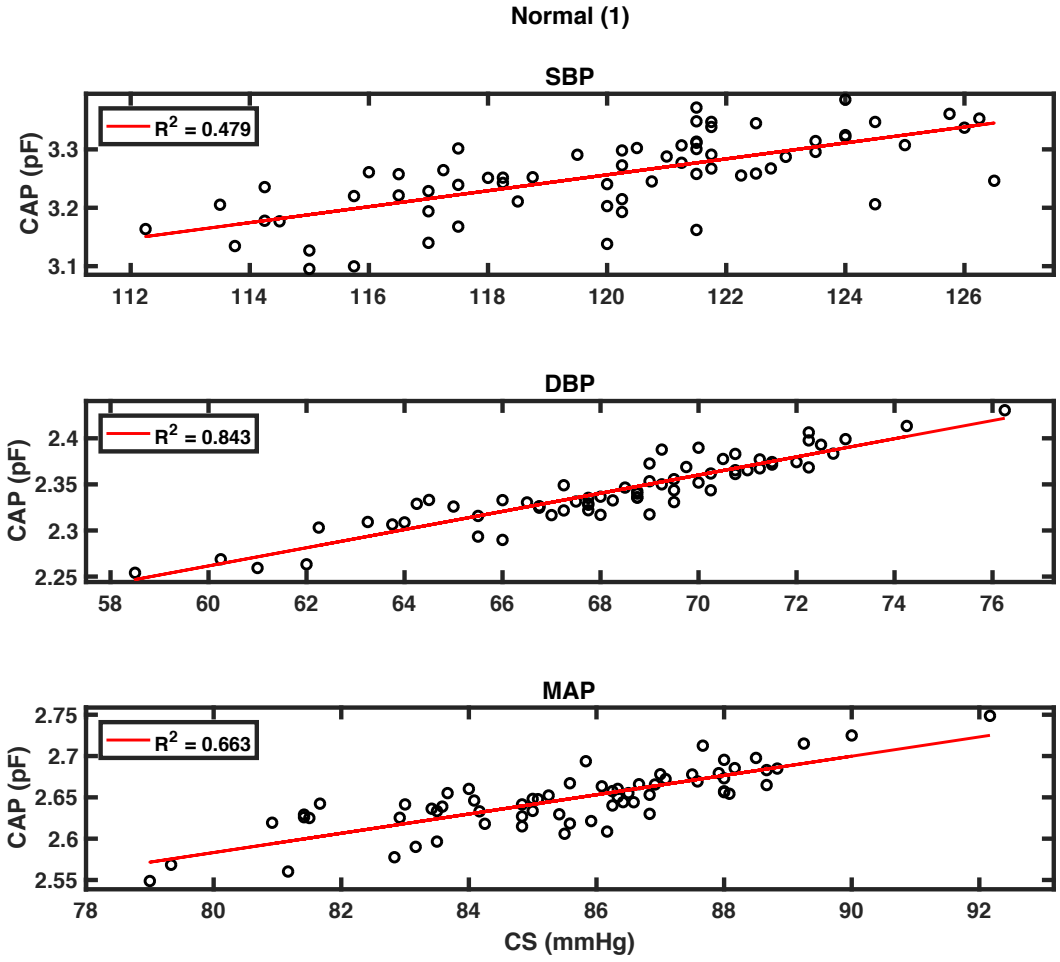
Normal (1)
SBP
R2 = 0.479
CAP (pF)
3.3
3.2
3.1
112
114
116
118
120
122
124
126
DBP
R2 = 0.843
CAP (pF)
2.4
2.35
2.3
2.25
58
60
62
64
66
68
70
72
74
76
MAP
R2 = 0.663
CAP (pF)
2.75
2.7
2.65
2.6
2.55
78
80
82
84
86
88
90
92
CS (mmHg)

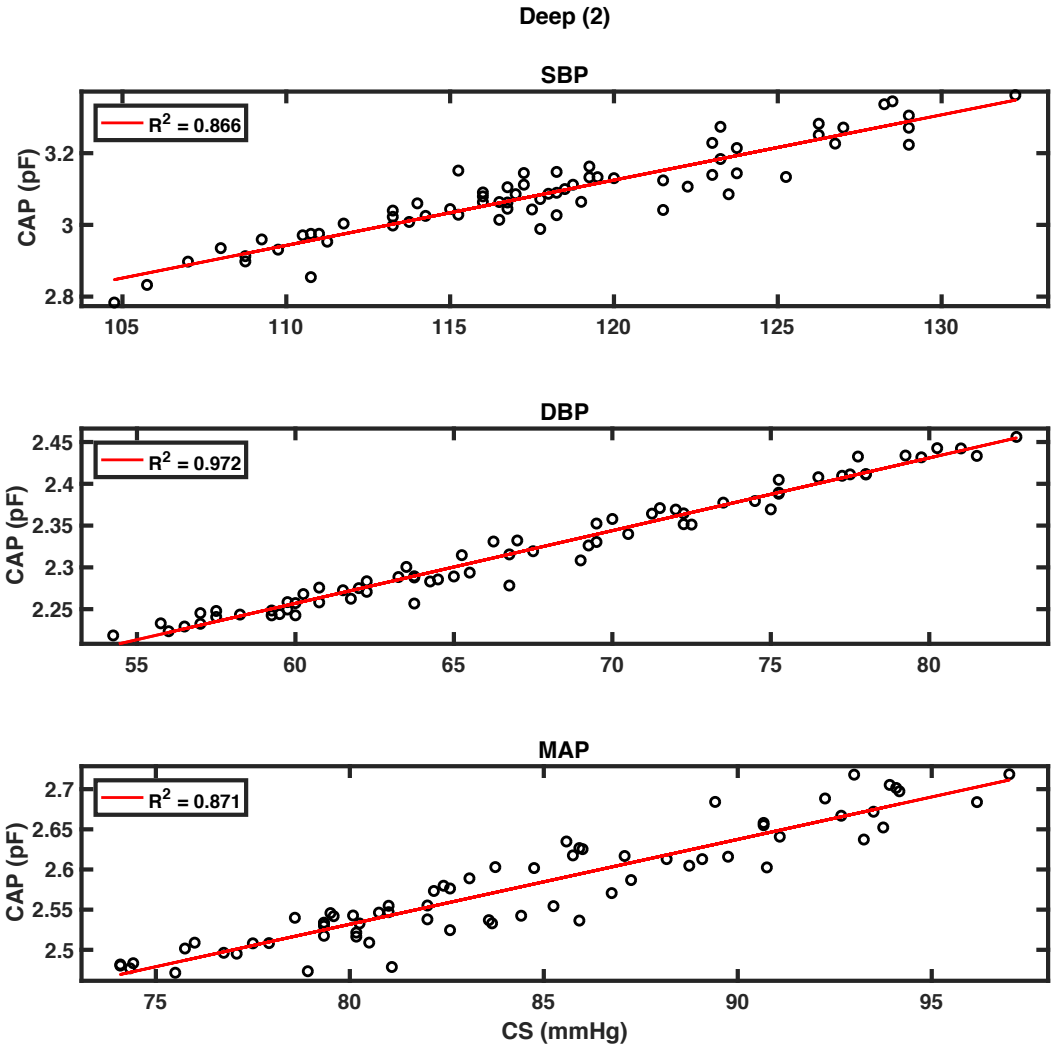
Deep (2)
SBP
R² = 0.866
CAP (pF)
3.2
3
2.8
105
110
115
120
125
130
DBP
R² = 0.972
CAP (pF)
2.45
2.4
2.35
2.3
2.25
55
60
65
70
75
80
MAP
R² = 0.871
CAP (pF)
2.7
2.65
2.6
2.55
2.5
75
80
85
90
95
CS (mmHg)

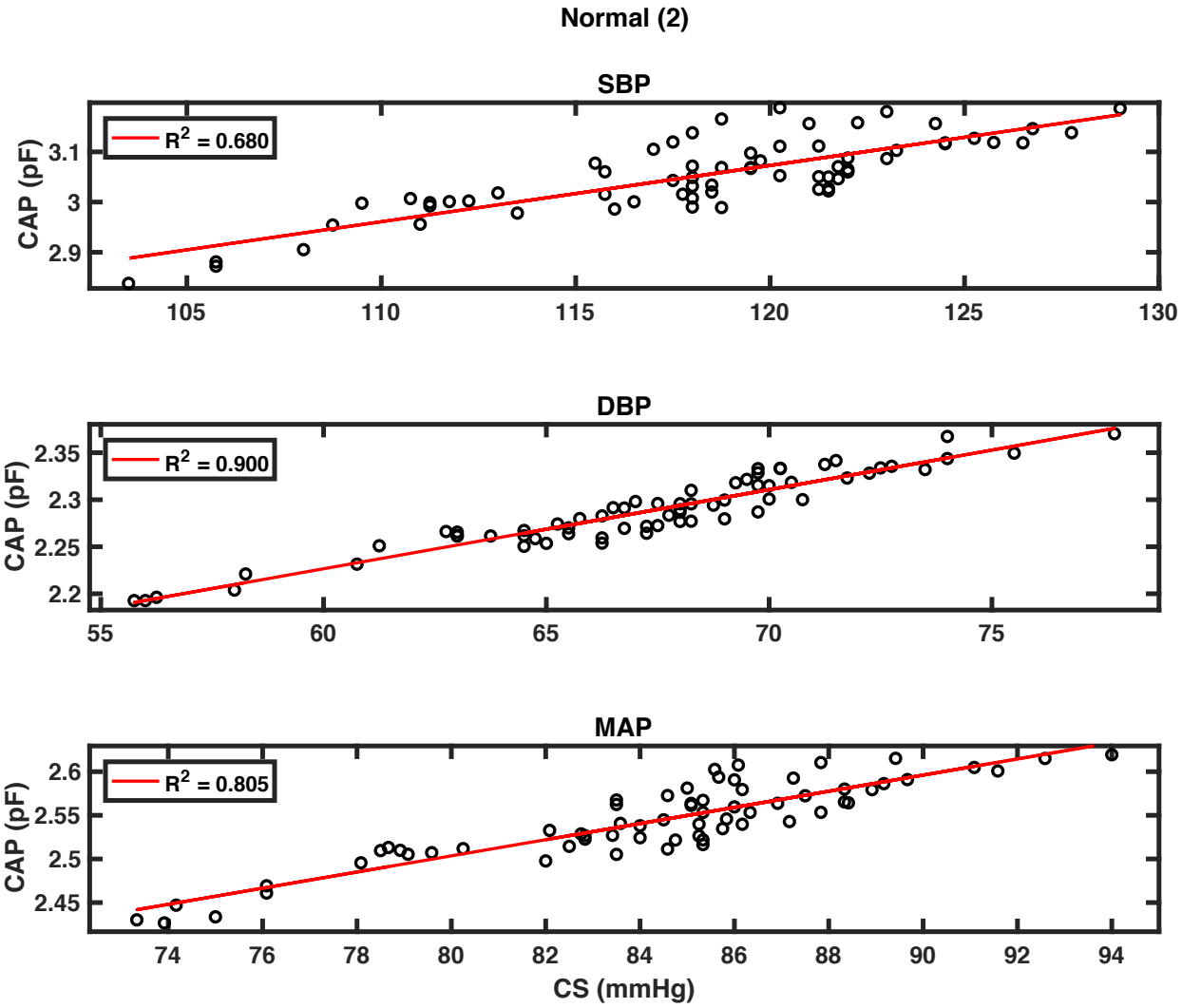
Normal (2)
SBP
R2 = 0.680
CAP (pF)
3.1
3
2.9
105
110
115
120
125
130
DBP
R2 = 0.900
CAP (pF)
2.35
2.3
2.25
2.2
55
60
65
70
75
MAP
R2 = 0.805
CAP (pF)
2.6
2.55
2.5
2.45
74
76
78
80
82
84
86
88
90
92
94
CS (mmHg)

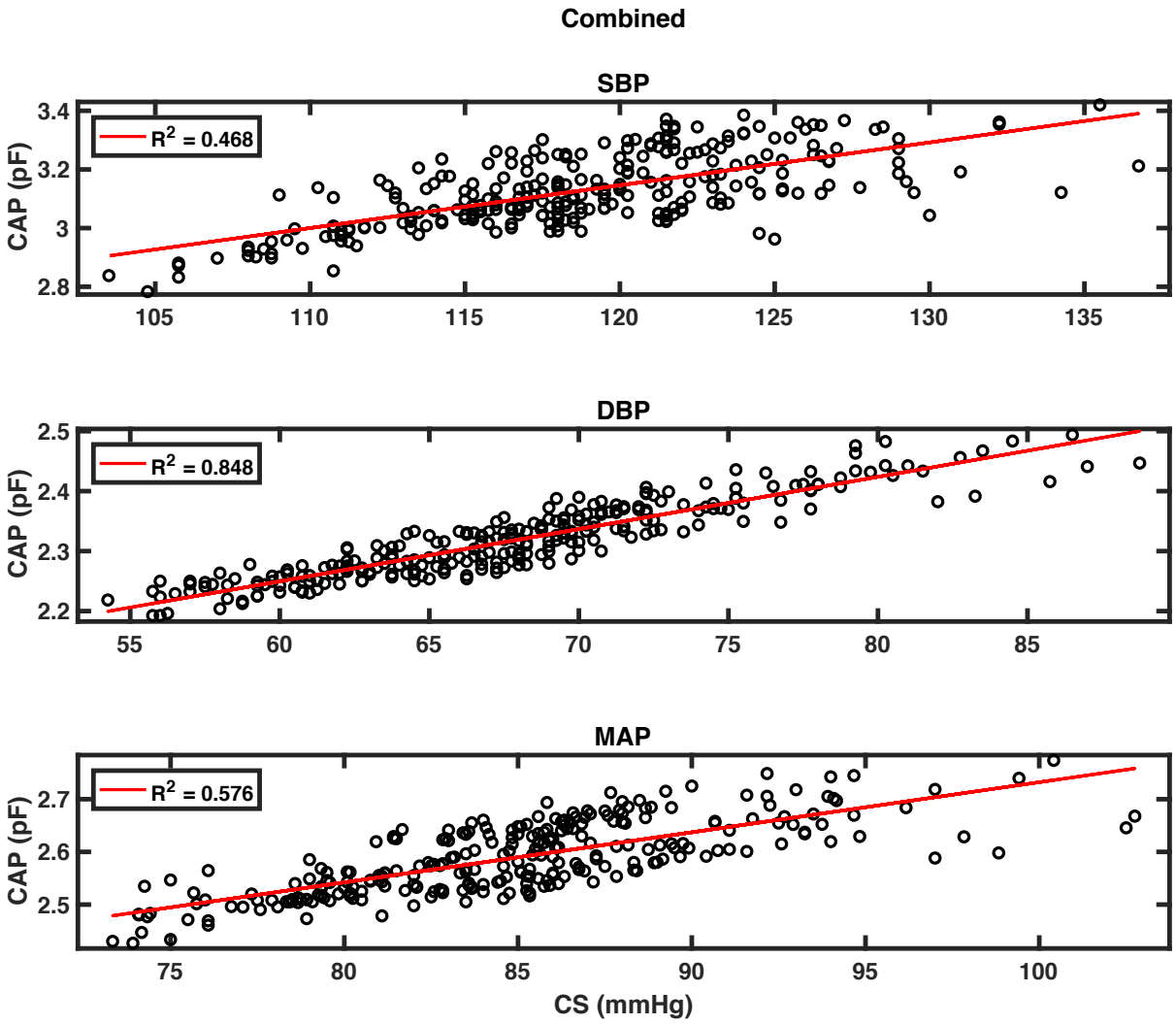
Combined
SBP
R2 = 0.468
CAP (pF)
3.4
3.2
3
2.8
105
110
115
120
125
130
135
DBP
R2 = 0.848
CAP (pF)
2.5
2.4
2.3
2.2
55
60
65
70
75
80
85
MAP
R2 = 0.576
CAP (pF)
2.7
2.6
2.5
75
80
85
90
95
100
CS (mmHg)

1-Beat Average

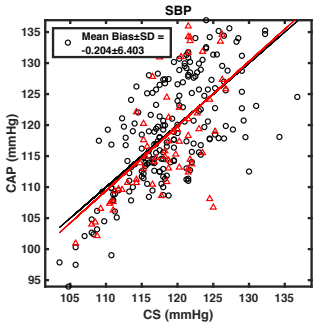

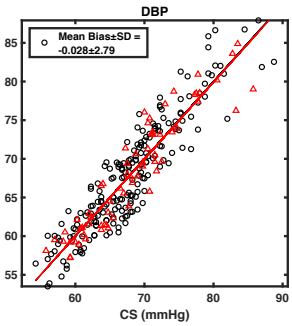

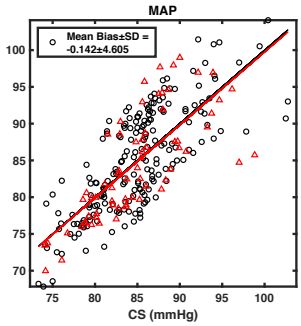

3-Beat Average

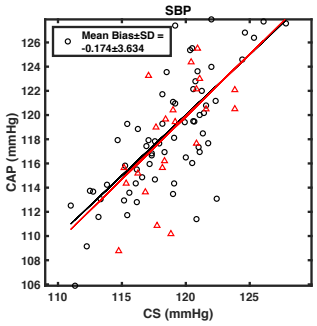

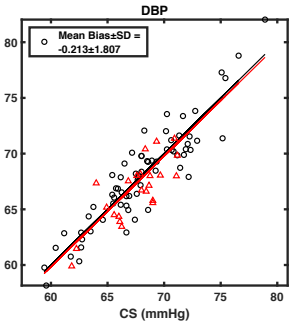

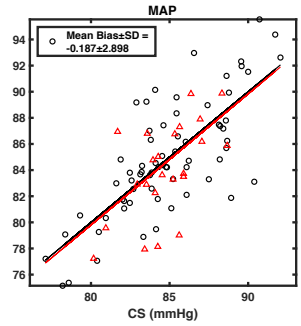

5-Beat Average

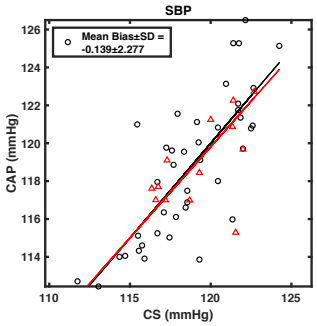

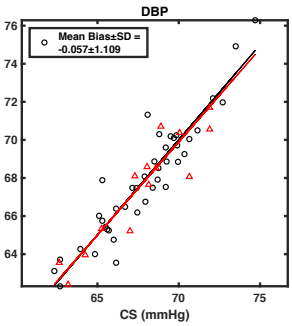

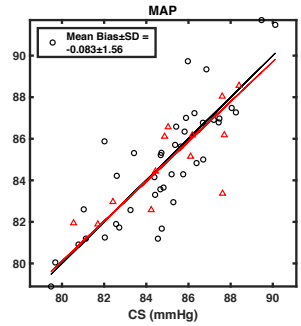

7-Beat Average

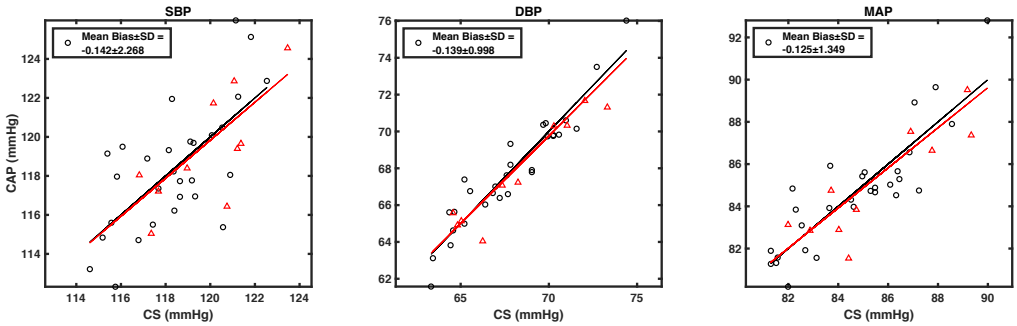

10-Beat Average

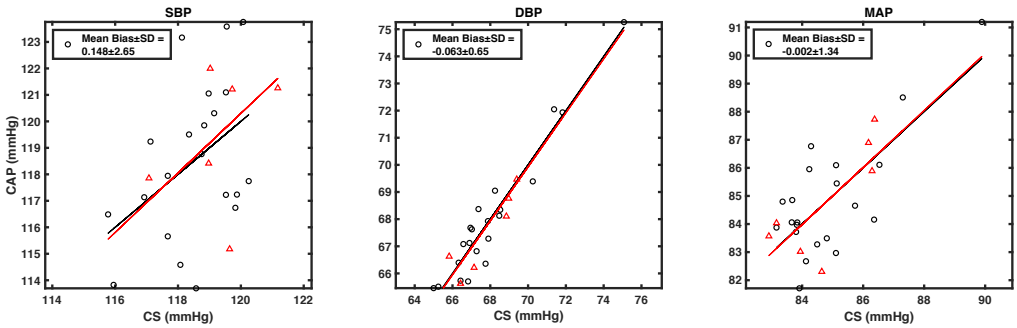

SI.6 Subject 7

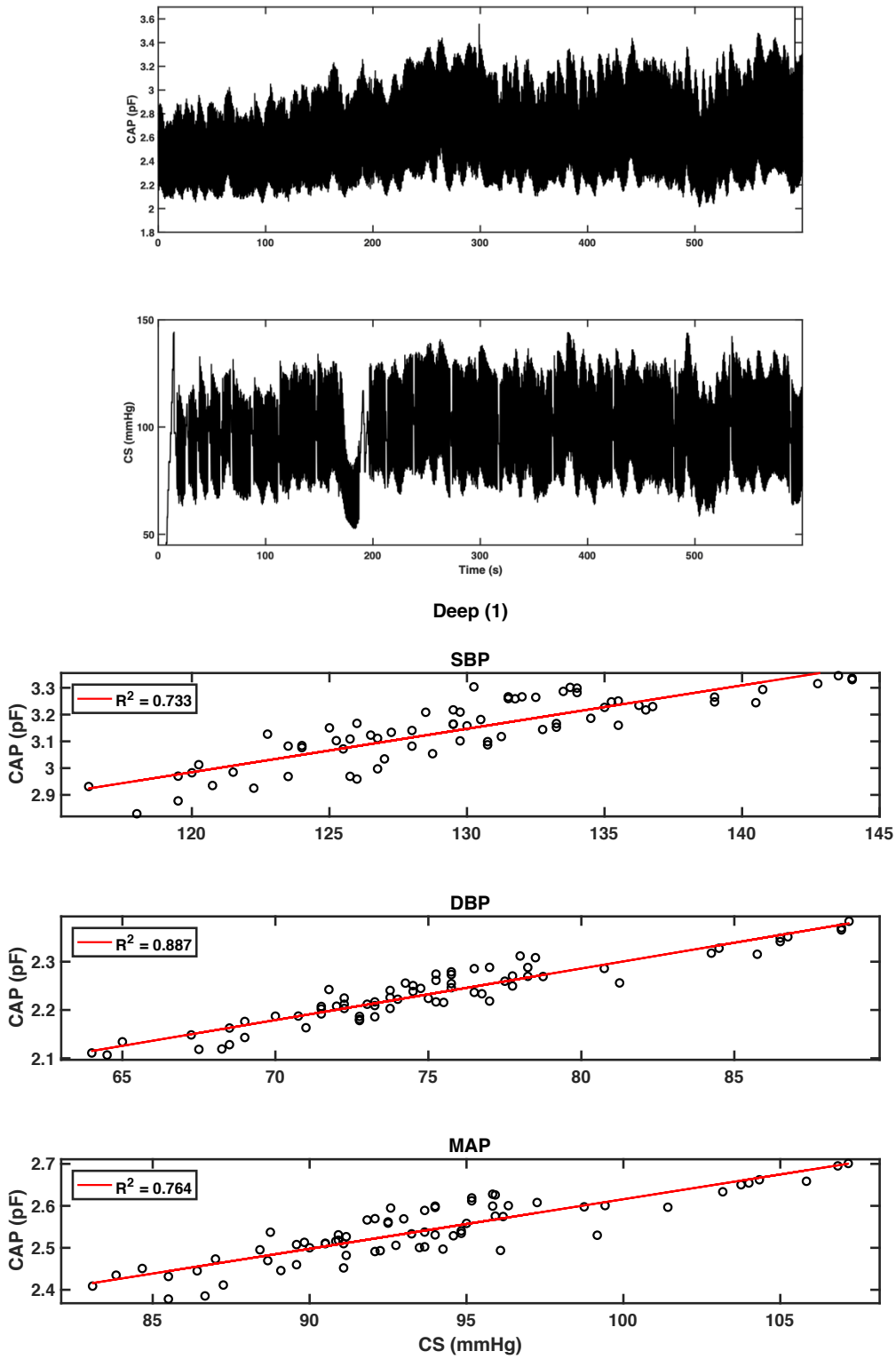

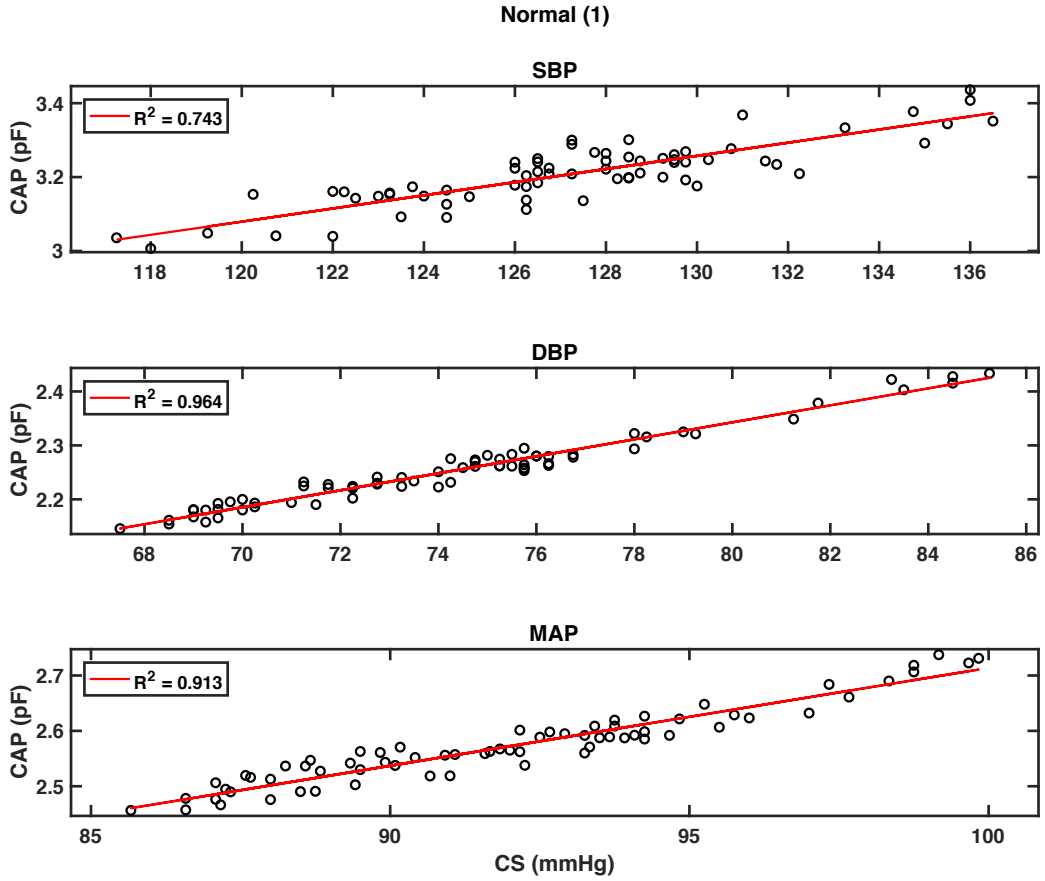
Normal (1)
SBP
R2 = 0.743
CAP (pF)
3.4
3.2
3
118
120
122
124
126
128
130
132
134
136
DBP
R2 = 0.964
CAP (pF)
2.4
2.3
2.2
68
70
72
74
76
78
80
82
84
86
MAP
R2 = 0.913
CAP (pF)
2.7
2.6
2.5
85
90
95
100
CS (mmHg)

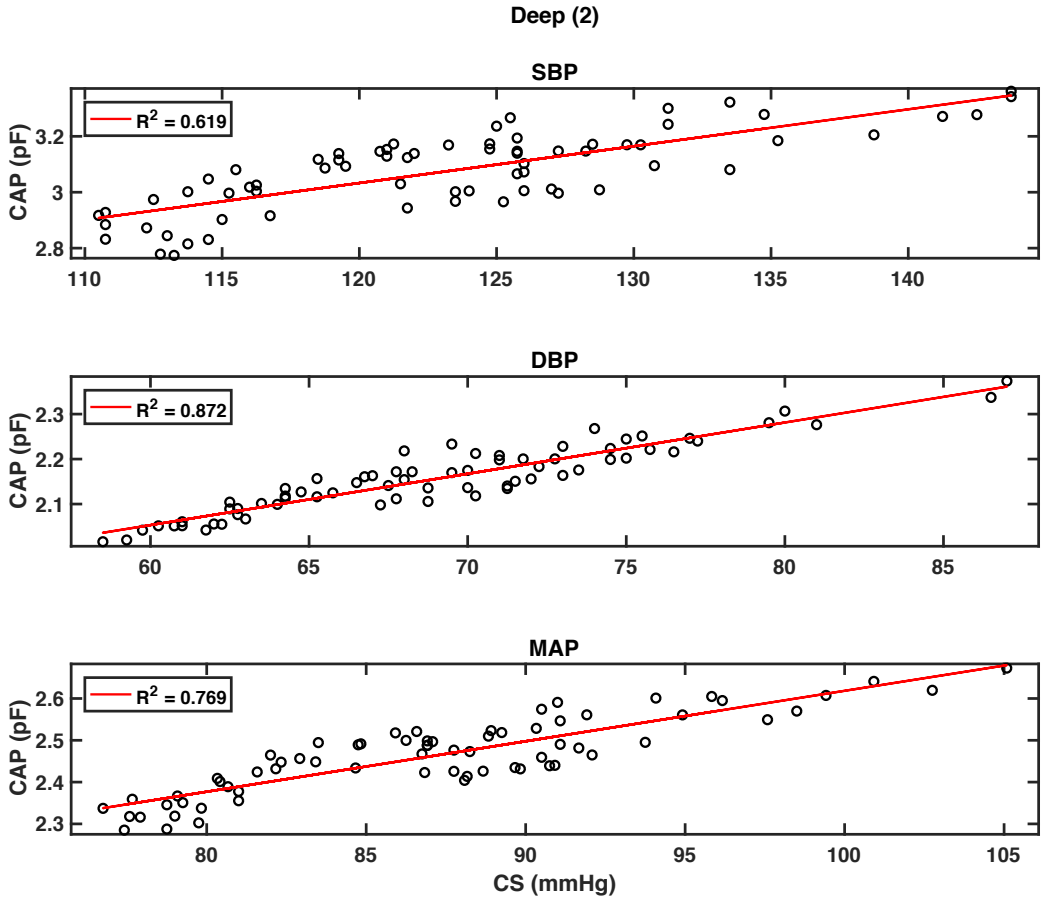
Deep (2)
SBP
R² = 0.619
CAP (pF)
3.2
3
2.8
110
115
120
125
130
135
140
DBP
R² = 0.872
CAP (pF)
2.3
2.2
2.1
60
65
70
75
80
85
MAP
R² = 0.769
CAP (pF)
2.6
2.5
2.4
2.3
80
85
90
95
100
105
CS (mmHg)

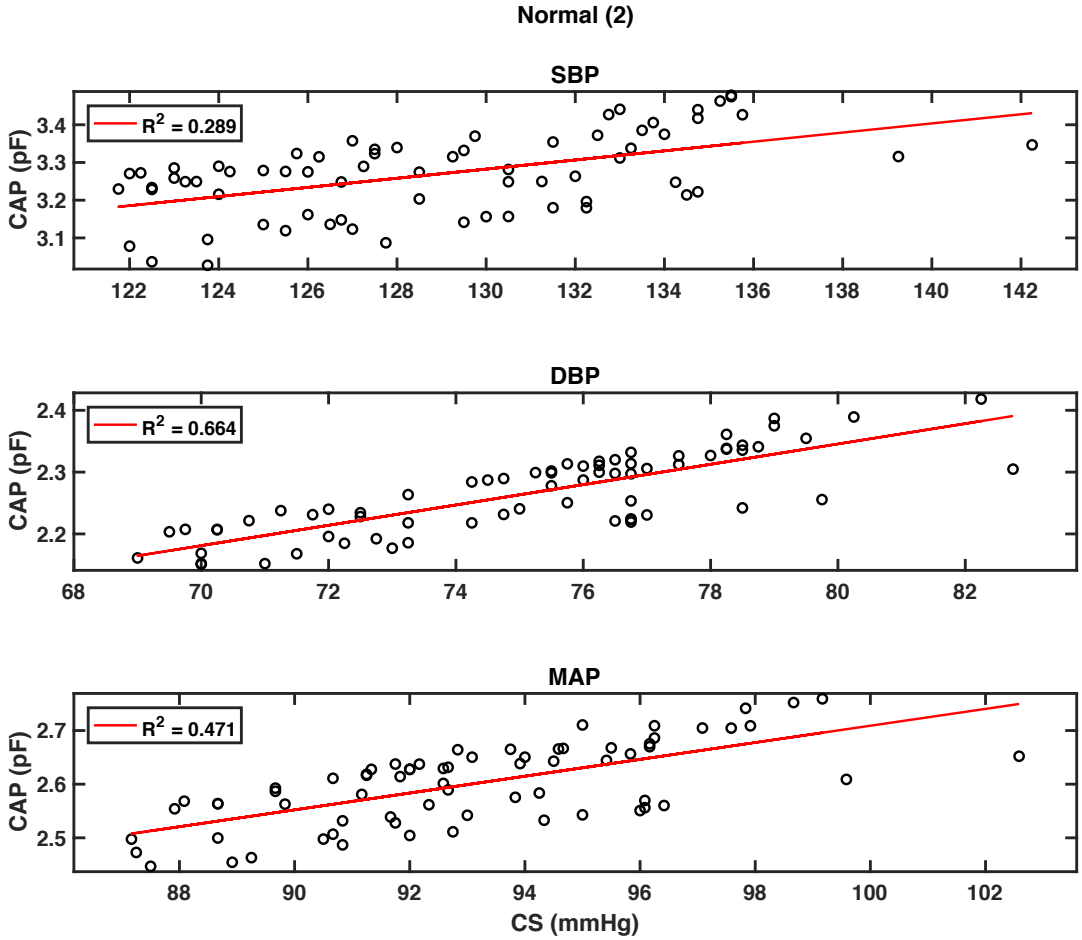
Normal (2)
SBP
R2 = 0.289
CAP (pF)
3.4
3.3
3.2
3.1
122
124
126
128
130
132
134
136
138
140
142
DBP
R2 = 0.664
CAP (pF)
2.4
2.3
2.2
68
70
72
74
76
78
80
82
MAP
R2 = 0.471
CAP (pF)
2.7
2.6
2.5
88
90
92
94
96
98
100
102
CS (mmHg)

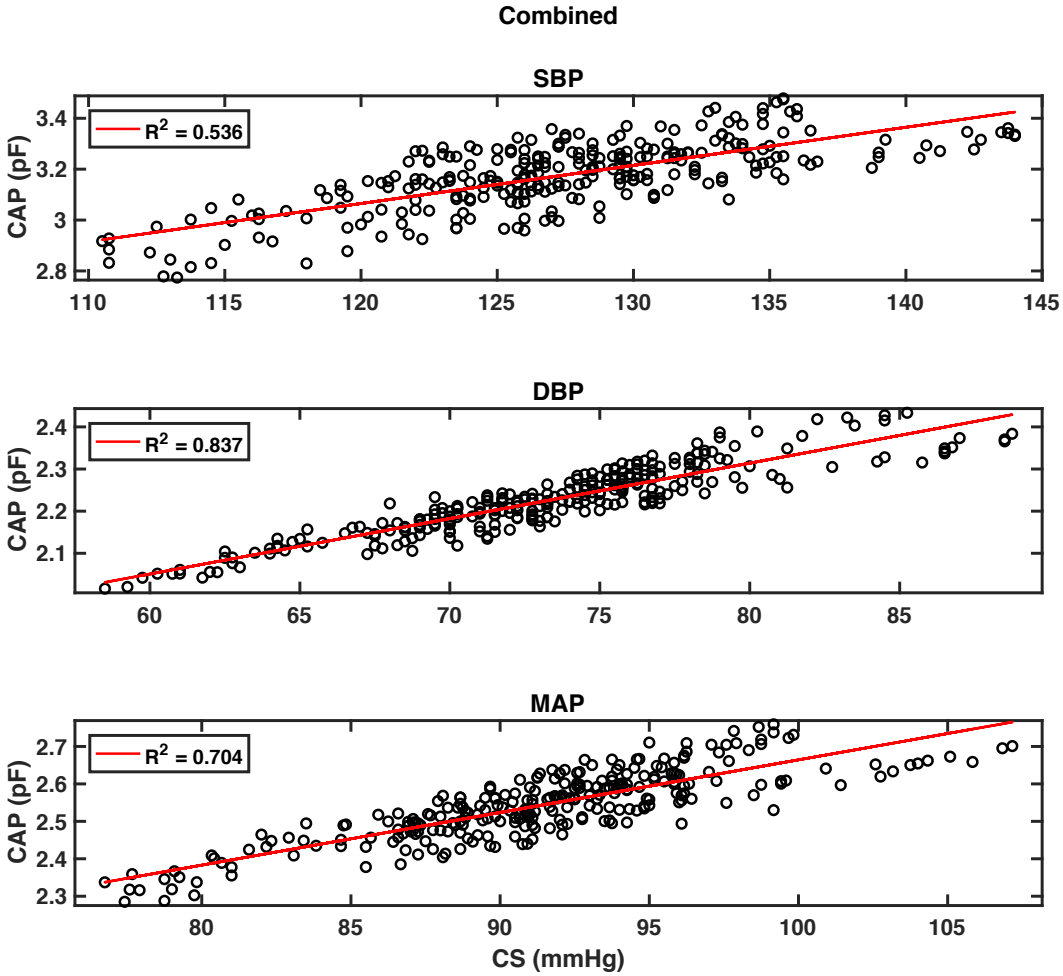
Combined
SBP
R2 = 0.536
CAP (pF)
3.4
3.2
3
2.8
110
115
120
125
130
135
140
145
DBP
R2 = 0.837
CAP (pF)
2.4
2.3
2.2
2.1
60
65
70
75
80
85
MAP
R2 = 0.704
CAP (pF)
2.7
2.6
2.5
2.4
2.3
80
85
90
95
100
105
CS (mmHg)

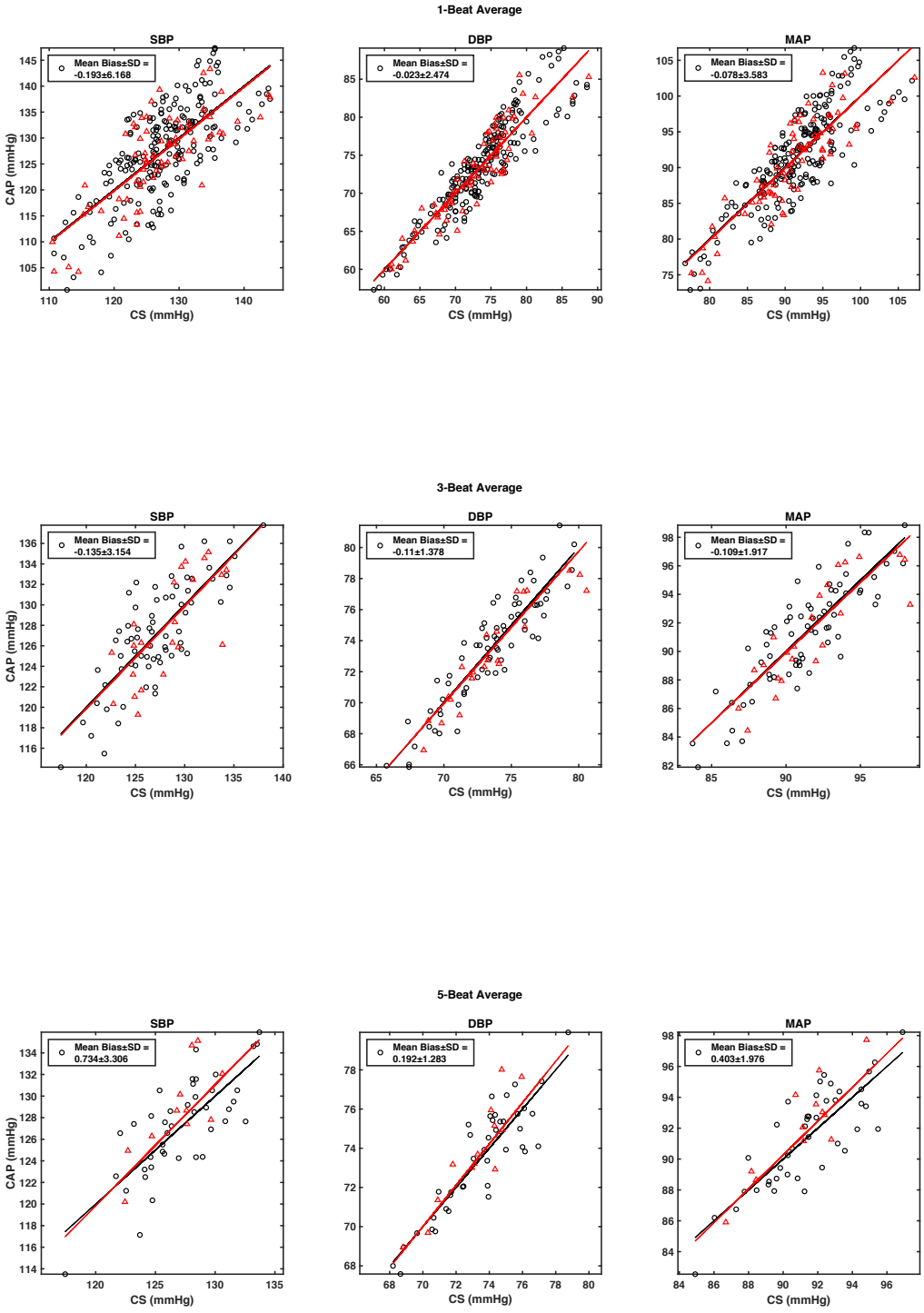
1-Beat Average
SBP
Mean Bias±SD =
-0.193±6.168
CAP (mmHg)
CS (mmHg)
DBP
Mean Bias±SD =
-0.023±2.474
CS (mmHg)
MAP
Mean Bias±SD =
-0.078±3.583
CS (mmHg)
3-Beat Average
SBP
Mean Bias±SD =
-0.135±3.154
CAP (mmHg)
CS (mmHg)
DBP
Mean Bias±SD =
-0.11±1.378
CS (mmHg)
MAP
Mean Bias±SD =
-0.109±1.917
CS (mmHg)
5-Beat Average
SBP
Mean Bias±SD =
0.734±3.306
CAP (mmHg)
CS (mmHg)
DBP
Mean Bias±SD =
0.192±1.283
CS (mmHg)
MAP
Mean Bias±SD =
0.403±1.976
CS (mmHg)

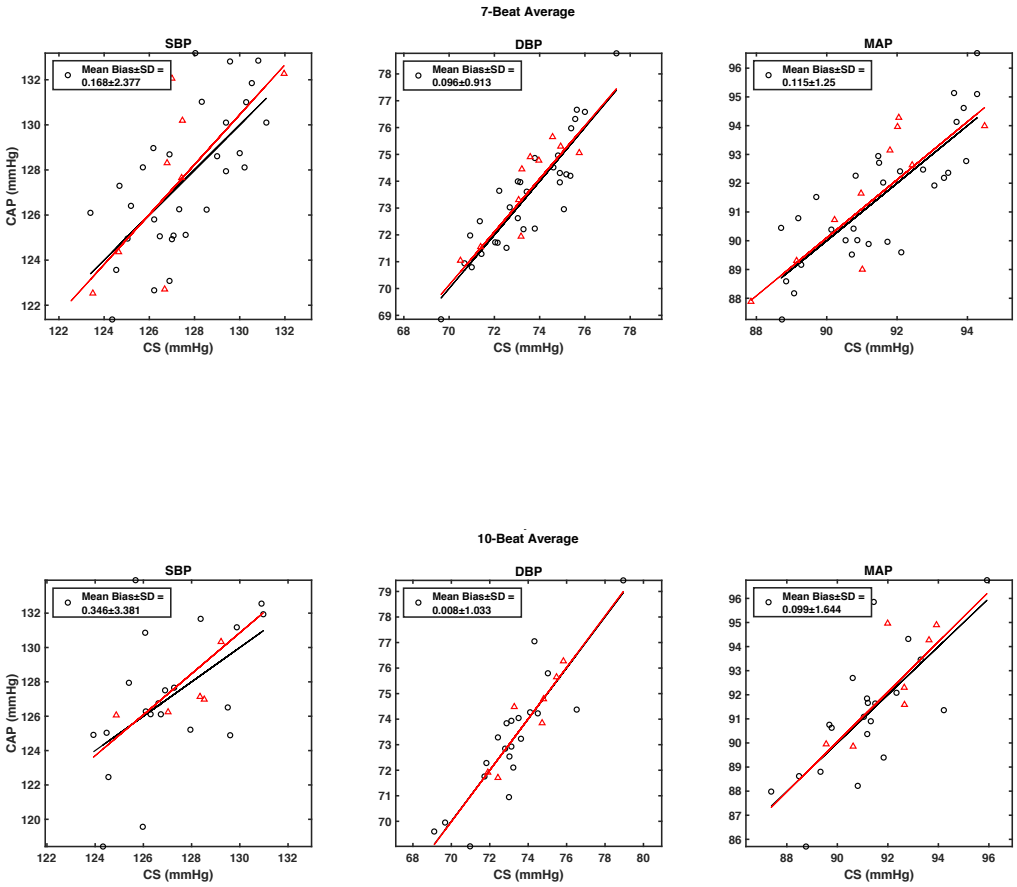
7-Beat Average
SBP
Mean Bias±SD =
0.168±2.377
CAP (mmHg)
CS (mmHg)
DBP
Mean Bias±SD =
0.096±0.913
CS (mmHg)
MAP
Mean Bias±SD =
0.115±1.25
CS (mmHg)
10-Beat Average
SBP
Mean Bias±SD =
0.346±3.381
CAP (mmHg)
CS (mmHg)
DBP
Mean Bias±SD =
0.008±1.033
CS (mmHg)
MAP
Mean Bias±SD =
0.099±1.644
CS (mmHg)

SI.7 Bland-Altman plots of averaged subject tests

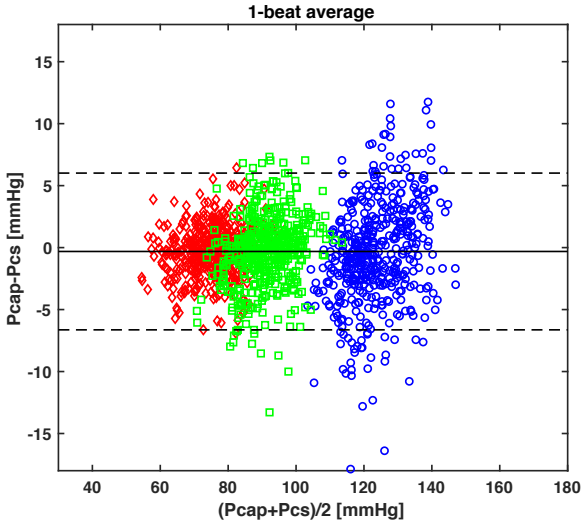

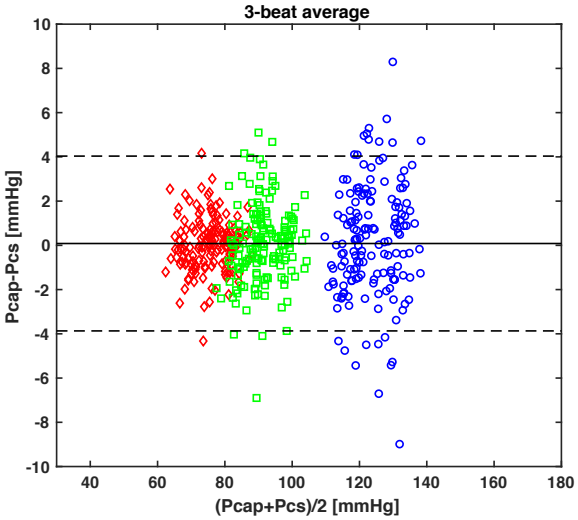

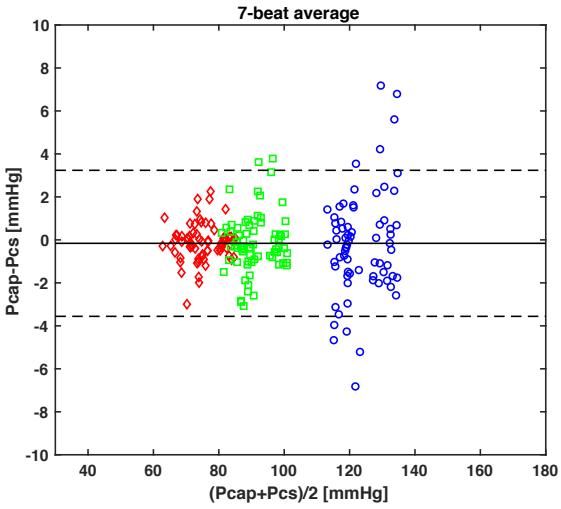

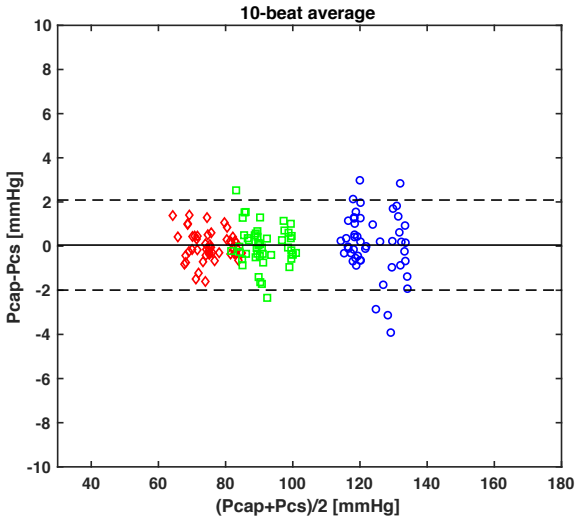

REFERENCES

1. Wang, Y. & Zhang, X. *CCIS 312 - Internet of Things*.

2. Xia, F., Yang, L. T., Wang, L. & Vinel, A. Internet of things. *International Journal of Communication Systems* **25,** 1101–1102 (2012).

3. Lakhal, K., Ehrmann, S. & Boulain, T. Noninvasive BP Monitoring in the Critically Ill: Time to Abandon the Arterial Catheter? *Chest* **153,** 1023–1039 (2018).

4. Dagdeviren, C. *et al.* Conformable amplified lead zirconate titanate sensors with enhanced piezoelectric response for cutaneous pressure monitoring. *Nat. Commun.* **5,** 4496 (2014).

5. Wang, Z. *et al.* High Sensitivity, Wearable, Piezoresistive Pressure Sensors Based on Irregular Microhump Structures and Its Applications in Body Motion Sensing. *Small* **12,** 3827–3836 (2016).

6. Zang, Y. *et al.* Flexible suspended gate organic thin-film transistors for ultra-sensitive pressure detection. *Nat. Commun.* **6,** 6269 (2015).

7. Luo, N. *et al.* Flexible Piezoresistive Sensor Patch Enabling Ultralow Power Cuffless Blood Pressure Measurement. *Adv. Funct. Mater.* **26,** 1178–1187 (2016).

8. Pang, Y. *et al.* Flexible, Highly Sensitive, and Wearable Pressure and Strain Sensors with Graphene Porous Network Structure. *ACS Appl. Mater. Interfaces* **8,** 26458–26462 (2016).

9. Li, R., Nie, B., Digiglio, P. & Pan, T. Microflotronics: A flexible, transparent, pressure-sensitive microfluidic film. *Adv. Funct. Mater.* **24,** 6195–6203 (2014).

10. Park, S.-J., Kim, J., Chu, M. & Khine, M. Flexible Piezoresistive Pressure Sensor Using

Wrinkled Carbon Nanotube Thin Films for Human Physiological Signals. *Adv. Mater. Technol.* **3,** 1700158 (2018).

11. Nelson, M. R. *et al.* Noninvasive Measurement of Central Vascular Pressures With Arterial Tonometry: Clinical Revival of the Pulse Pressure Waveform? *Mayo Clin. Proc.* **85,** 460–72 (2010).

12. Chung, E., Chen, G., Alexander, B. & Cannesson, M. Non-invasive continuous blood pressure monitoring: a review of current applications. *Front. Med.* **7,** 91–101 (2013).

13. Crilly, M., Coch, C., Clark, H., Bruce, M. & Williams, D. Repeatability of the measurement of augmentation index in the clinical assessment of arterial stiffness using radial applanation tonometry. *Scand. J. Clin. Lab. Invest.* **67,** 413–422 (2007).

14. Crilly, M., Coch, C., Bruce, M., Clark, H. & Williams, D. Repeatability of central aortic blood pressures measured non-invasively using radial artery applanation tonometry and peripheral pulse wave analysis. *Blood Press.* **16,** 262–269 (2007).

15. Melenovsky, V. *et al.* Estimation of central pressure augmentation using automated radial artery tonometry. *J. Hypertens.* **25,** 1403–1409 (2007).

16. Nix, W. D. Mechanical properties of thin films. *Metall. Trans. A* **20,** 2217–2245 (1989).

17. Saha, R. & Nix, W. D. Effects of the substrate on the determination of thin film mechanical properties by nanoindentation. *Acta Mater.* **50,** 23–38 (2002).

18. Hoffman, R. W. Stress distributions and thin film mechanical properties. *Surf. Interface Anal.* **3,** 62–66 (1981).

19. Chason, E., Sheldon, B. W., Freund, L. B., Floro, J. A. & Hearne, S. J. Origin of

Compressive Residual Stress in Polycrystalline Thin Films. *Phys. Rev. Lett.* **88,** 4 (2002).

20. Guduru, P. R., Chason, E. & Freund, L. B. Mechanics of compressive stress evolution during thin film growth. in *Journal of the Mechanics and Physics of Solids* **51,** 2127–2148 (Pergamon, 2003).

21. Thompson, C. V. & Carel, R. Stress and grain growth in thin films. *J. Mech. Phys. Solids* **44,** 657–673 (1996).

22. Gleskova, H., Wagner, S. & Suo, Z. a-Si:H thin film transistors after very high strain. *J. Non. Cryst. Solids* **266–269,** 1320–1324 (2000).

23. Park, S.-I. *et al.* Theoretical and Experimental Studies of Bending of Inorganic Electronic Materials on Plastic Substrates. *Adv. Funct. Mater.* 2673–2684 (2008). doi:10.1002/adfm.200800306

24. Lipomi, D. J. *et al.* Skin-like pressure and strain sensors based on transparent elastic films of carbon nanotubes. *Nat. Nanotechnol.* **6,** 788–792 (2011).

25. Cai, L. *et al.* Super-stretchable, transparent carbon nanotube-based capacitive strain sensors for human motion detection. *Sci. Rep.* **3,** 3048 (2013).

26. Lambot, S., Slob, E. C., Van Bosch, I. Den, Stockbroeckx, B. & Vanclooster, M. Modeling of ground-penetrating radar for accurate characterization of subsurface electric properties. *IEEE Trans. Geosci. Remote Sens.* **42,** 2555–2568 (2004).

27. Zhang, Y. *et al.* Polymer-Embedded Carbon Nanotube Ribbons for Stretchable Conductors. *Adv. Mater.* **22,** 3027–3031 (2010).

28. Wang, J. *et al.* A highly sensitive and flexible pressure sensor with electrodes and

elastomeric interlayer containing silver nanowires. *Nanoscale* **7,** 2926–2932 (2015).

29. Shuai, X. *et al.* Highly Sensitive Flexible Pressure Sensor Based on Silver Nanowires-Embedded Polydimethylsiloxane Electrode with Microarray Structure. *ACS Appl. Mater. Interfaces* **9,** 26314–26324 (2017).

30. Ouyang, G., Wang, K. & Chen, X. Y. TiO 2 nanoparticles modified polydimethylsiloxane with fast response time and increased dielectric constant. *J. Micromechanics Microengineering* **22,** 74002 (2012).

31. Sekitani, T. *et al.* Stretchable active-matrix organic light-emitting diode display using printable elastic conductors. *Nat. Mater.* **8,** 494–499 (2009).

32. Park, S.-J., Kim, J., Chu, M. & Khine, M. Highly Flexible Wrinkled Carbon Nanotube Thin Film Strain Sensor to Monitor Human Movement. *Adv. Mater. Technol.* **1,** 1600053 (2016).

33. Catenacci, M. J., Reyes, C., Cruz, M. A. & Wiley, B. J. Stretchable Conductive Composites from Cu–Ag Nanowire Felt. *ACS Nano* **12,** 3689–3698 (2018).

34. Park, H., Seo, K. & Crozier, K. B. Adding colors to polydimethylsiloxane by embedding vertical silicon nanowires. *Appl. Phys. Lett.* **101,** 193107 (2012).

35. Coleman, J. N., Khan, U., Blau, W. J. & Gun'ko, Y. K. Small but strong: A review of the mechanical properties of carbon nanotube-polymer composites. *Carbon* **44,** 1624–1652 (2006).

36. Hussain, M., Choa, Y.-H. & Niihara, K. Conductive rubber materials for pressure sensors. *J. Mater. Sci. Lett.* **20,** 525–527 (2001).

37. Sandler, J. K. W., Kirk, J. E., Kinloch, I. A., Shaffer, M. S. P. & Windle, A. H. Ultra-low electrical percolation threshold in carbon-nanotube-epoxy composites. *Polymer (Guildf).* **44,** 5893–5899 (2003).

38. Celzard, A. *et al. Critical concentration in percolating systems containing a high-aspect-ratio filler*. (1996).

39. Munson-Mcgee, S. H. *Estimation of the critical concentration in an anisotropic percolation network*. *PHYSICAL REVIEW B* **43,** (1991).

40. Kilbride, B. E. *et al.* Experimental observation of scaling laws for alternating current and direct current conductivity in polymer-carbon nanotube composite thin films. *Cit. J. Appl. Phys.* **92,** 4024 (2002).

41. Dickey, M. D. *et al.* Eutectic gallium-indium (EGaIn): A liquid metal alloy for the formation of stable structures in microchannels at room temperature. *Adv. Funct. Mater.* **18,** 1097–1104 (2008).

42. Tabatabai, A., Fassler, A., Usiak, C. & Majidi, C. Liquid-phase gallium-indium alloy electronics with microcontact printing. *Langmuir* **29,** 6194–6200 (2013).

43. Mineart, K. P. *et al.* Ultrastretchable, cyclable and recyclable 1- and 2-dimensional conductors based on physically cross-linked thermoplastic elastomer gels. *Soft Matter* **9,** 7695 (2013).

44. Dickey, M. D. Stretchable and Soft Electronics using Liquid Metals. *Adv. Mater.* **29,** 1606425 (2017).

45. Lacour, S. P., Jones, J., Wagner, S., Li, T. & Suo, Z. Stretchable Interconnects for Elastic

Electronic Surfaces. *Proc. IEEE* **93,** 1459–1466 (2005).

46. Li, T. *et al.* Delocalizing strain in a thin metal film on a polymer substrate. *Mech. Mater.* **37,** 261–273 (2005).

47. Byun, I., Coleman, A. W. & Kim, B. Transfer of thin Au films to polydimethylsiloxane (PDMS) with reliable bonding using (3-mercaptopropyl)trimethoxysilane (MPTMS) as a molecular adhesive. *J. Micromechanics Microengineering* **23,** 085016 (2013).

48. Lu, N., Lu, C., Yang, S. & Rogers, J. Highly sensitive skin-mountable strain gauges based entirely on elastomers. *Adv. Funct. Mater.* **22,** 4044–4050 (2012).

49. Lu, N., Wang, X., Suo, Z. & Vlassak, J. Metal films on polymer substrates stretched beyond 50%. *Appl. Phys. Lett.* **91,** 2–4 (2007).

50. Li, T., Huang, Z., Suo, Z., Lacour, S. P. & Wagner, S. Stretchability of thin metal films on elastomer substrates. *Appl. Phys. Lett.* **85,** 3435–3437 (2004).

51. Li, T. & Suo, Z. Ductility of thin metal films on polymer substrates modulated by interfacial adhesion. *Int. J. Solids Struct.* **44,** 1696–1705 (2007).

52. Cordill, M. J., Glushko, O., Kreith, J., Marx, V. M. & Kirchlechner, C. Measuring electro-mechanical properties of thin films on polymer substrates. *Microelectron. Eng.* **137,** 96–100 (2015).

53. Lu, N., Wang, X., Suo, Z. & Vlassak, J. Metal films on polymer substrates stretched beyond 50%. *Appl. Phys. Lett.* **91,** 221909 (2007).

54. Rogers, J. a, Someya, T. & Huang, Y. Materials and mechanics for stretchable electronics. *Science* **327,** 1603–1607 (2010).

55. Wang, Y. *et al.* Super-elastic graphene ripples for flexible strain sensors. *ACS Nano* **5,** 3645–3650 (2011).

56. Kaltenbrunner, M. *et al.* An ultra-lightweight design for imperceptible plastic electronics. *Nature* **499,** 458–63 (2013).

57. Putz, B., Schoeppner, R. L., Glushko, O., Bahr, D. F. & Cordill, M. J. Improved electro-mechanical performance of gold films on polyimide without adhesion layers. *Scr. Mater.* **102,** 23–26 (2015).

58. Schwartz, G. *et al.* Flexible polymer transistors with high pressure sensitivity for application in electronic skin and health monitoring. *Nat. Commun.* **4,** 1859 (2013).

59. Vohra, A., Carmichael, R. S. & Carmichael, T. B. Developing the Surface Chemistry of Transparent Butyl Rubber for Impermeable Stretchable Electronics. *Langmuir* **32,** 10206–10212 (2016).

60. Guo, C. F., Chen, Y., Tang, L., Wang, F. & Ren, Z. Enhancing the Scratch Resistance by Introducing Chemical Bonding in Highly Stretchable and Transparent Electrodes. *Nano Lett.* **16,** 594–600 (2016).

61. Kim, J. *et al.* Highly stretchable wrinkled gold thin film wires. *Appl. Phys. Lett.* **108,** 061901 (2016).

62. Xu, S. *et al.* Stretchable batteries with self-similar serpentine interconnects and integrated wireless recharging systems. *Nat. Commun.* **4,** 1543 (2013).

63. Zhao, X., Hua, Q., Yu, R., Zhang, Y. & Pan, C. Flexible, Stretchable and Wearable Multifunctional Sensor Array as Artificial Electronic Skin for Static and Dynamic Strain

Mapping. *Adv. Electron. Mater.* **1,** 1–7 (2015).

64. Kim, D.-H. *et al.* Optimized Structural Designs for Stretchable Silicon Integrated Circuits. doi:10.1002/smll.200900853

65. Ahn, J.-H. & Je, J. H. Stretchable electronics: materials, architectures and integrations. *J. Phys. D. Appl. Phys.* **45,** 103001 (2012).

66. Gutruf, P., Walia, S., Nur Ali, M., Sriram, S. & Bhaskaran, M. Strain response of stretchable micro-electrodes: Controlling sensitivity with serpentine designs and encapsulation. *Appl. Phys. Lett.* **104,** (2014).

67. Xu, F., Wang, X., Zhu, Y. & Zhu, Y. Wavy Ribbons of Carbon Nanotubes for Stretchable Conductors. *Adv. Funct. Mater.* **22,** 1279–1283 (2012).

68. Sun, Y., Choi, W. M., Jiang, H., Huang, Y. Y. & Rogers, J. a. Controlled buckling of semiconductor nanoribbons for stretchable electronics. *Nat. Nanotechnol.* **1,** 201–7 (2006).

69. Chortos, A. & Bao, Z. Skin-inspired electronic devices. *Mater. Today* **17,** 321–331 (2014).

70. Pailler-Mattei, C., Bec, S. & Zahouani, H. In vivo measurements of the elastic mechanical properties of human skin by indentation tests. *Med. Eng. Phys.* **30,** 599–606 (2008).

71. Xing Liang & Boppart, S. A. Biomechanical Properties of In Vivo Human Skin From Dynamic Optical Coherence Elastography. *IEEE Trans. Biomed. Eng.* **57,** 953–959 (2010).

72. Kuwazuru, O., Saothong, J. & Yoshikawa, N. Mechanical approach to aging and wrinkling of human facial skin based on the multistage buckling theory. *Med. Eng. Phys.*

30, 516–522 (2008).

73. Kim, D.-H. *et al.* Epidermal electronics. *Science* **333,** 838–43 (2011).

74. Escoffier, C. *et al.* Age-Related Mechanical Properties of Human Skin: An In Vivo Study. *J. Invest. Dermatol.* **93,** 353–357 (1989).

75. Agache, P. G., Monneur, C., Leveque, J. L. & De Rigal, J. Mechanical properties and Young's modulus of human skin in vivo. *Arch. Dermatol. Res.* **269,** 221–232 (1980).

76. Annaidh, A. N., Ere, K., Destrade, M., Gilchrist, M. D. & Otténio, M. Characterising the Anisotropic Mechanical Properties of Excised Human Skin. (2013).

77. Silver, F. H., Freeman, J. W. & Devore, D. Viscoelastic properties of human skin and processed dermis. *Ski. Res. Technol.* **7,** 18–23 (2001).

78. Jemec, G. B. E. & Serup, J. Epidermal hydration and skin mechanics. The relationship between electrical capacitance and the mechanical properties of human skin in vivo. *Acta Derm. Venereol.* **70,** 245–247 (1990).

79. Jemec, G. B. E., Jemec, B., Jemec, B. I. E. & Serup, J. The effect of superficial hydration on the mechanical properties of human skin in vivo: Implications for plastic surgery. *Plast. Reconstr. Surg.* **85,** 100–103 (1990).

80. Christensen, M. S., Hargens, C. W., Nacht, S. & Gans, E. H. Viscoelastic properties of intact human skin: instrumentation, hydration effects, and the contribution of the stratum corneum. *J. Invest. Dermatol.* **69,** 282–286 (1977).

81. A, K. & A, L. Mechanical Behaviour of Skin: A Review. *J. Mater. Sci. Eng.* **5,** 4 (2016).

82. Holzapfel, G. A. *Biomechanics of Soft Tissue*. (2000).

83. Yongping Zheng & Mak, A. F. T. Effective elastic properties for lower limb soft tissues from manual indentation experiment. *IEEE Trans. Rehabil. Eng.* **7,** 257–267 (1999).

84. Boyer, G., Zahouani, H., Le Bot, A. & Laquieze, L. In vivo characterization of viscoelastic properties of human skin using dynamic micro-indentation. in *2007 29th Annual International Conference of the IEEE Engineering in Medicine and Biology Society* **2007,** 4584–4587 (IEEE, 2007).

85. Boyer, G., Laquièze, L., Le Bot, A., Laquièze, S. & Zahouani, H. Dynamic indentation on human skin in vivo: ageing effects. *Ski. Res. Technol.* **15,** 55–67 (2009).

86. Boyer, G. *et al.* Non contact method for in vivo assessment of skin mechanical properties for assessing effect of ageing. *Med. Eng. Phys.* **34,** 172–178 (2012).

87. Khaothong, K. in 1467–1470 (Springer, Berlin, Heidelberg, 2010). doi:10.1007/978-3-642-14515-5_374

88. Andersson, L. H. U., Johander, P. & Hjertberg, T. *Silicone Elastomers for Electronic Applications. II. Effects of Noncrosslinked Materials*. (2003).

89. Johnston, I. D., McCluskey, D. K., Tan, C. K. L. & Tracey, M. C. Mechanical characterization of bulk Sylgard 184 for microfluidics and microengineering. *J. Micromechanics Microengineering* **24,** 035017 (2014).

90. Kang, D. *et al.* Ultrasensitive mechanical crack-based sensor inspired by the spider sensory system. *Nature* **516,** 222–226 (2014).

91. Amjadi, M., Turan, M., Clementson, C. P. & Sitti, M. Parallel Microcracks-based Ultrasensitive and Highly Stretchable Strain Sensors. *ACS Appl. Mater. Interfaces* **8,**

5618–5626 (2016).

92. Amjadi, M., Pichitpajongkit, A., Lee, S., Ryu, S. & Park, I. Highly Stretchable and Sensitive Strain Sensor Based on Silver NanowireÀElastomer Nanocomposite. **8,** 5154–5163 (2014).

93. Kim, D.-H. *et al.* Epidermal electronics. *Science* **333,** 838–843 (2011).

94. Choong, C. L. *et al.* Highly stretchable resistive pressure sensors using a conductive elastomeric composite on a micropyramid array. *Adv. Mater.* **26,** 3451–3458 (2014).

95. Mannsfeld, S. C. B. *et al.* Highly sensitive flexible pressure sensors with microstructured rubber dielectric layers. *Nat. Mater.* **9,** 859–64 (2010).

96. Cohen, D. J., Mitra, D., Peterson, K. & Maharbiz, M. M. A highly elastic, capacitive strain gauge based on percolating nanotube networks. *Nano Lett.* **12,** 1821–1825 (2012).

97. Amjadi, M., Kyung, K.-U., Park, I. & Sitti, M. Stretchable, Skin-Mountable, and Wearable Strain Sensors and Their Potential Applications: A Review. *Adv. Funct. Mater.* **26,** 1678–1698 (2016).

98. Jiang, H. *et al.* Finite deformation mechanics in buckled thin films on compliant supports. *Proc. Natl. Acad. Sci. U. S. A.* **104,** 15607–15612 (2007).

99. Chi-Cheng Fu, B. *et al.* Tunable Nanowrinkles on Shape Memory Polymer Sheets. *Adv. Mater* **21,** 1–5 (2009).

100. Gabardo, C. M., Zhu, Y., Soleymani, L. & Moran-Mirabal, J. M. Bench-top fabrication of hierarchically structured high-surface-area electrodes. *Adv. Funct. Mater.* **23,** 3030–3039 (2013).

101. Bowden, N., Brittain, S., Evans, A. G., Hutchinson, J. W. & Whitesides, G. M. Spontaneous formation of ordered structures in thin films of metals supported on an elastomeric polymer. *Nature* **393,** 146–149 (1998).

102. Ramadan, A. A., Gould, R. D. & Ashour, A. *On the Van der Pauw method of resistivity measurements*. **239,** (1994).

103. Tenent, R. C. *et al.* Ultrasmooth, Large-Area, High-Uniformity, Conductive Transparent Single-Walled-Carbon-Nanotube Films for Photovoltaics Produced by Ultrasonic Spraying. *Adv. Mater.* **21,** 3210–3216 (2009).

104. Abdelhalim, A., Abdellah, A., Scarpa, G. & Lugli, P. Fabrication of carbon nanotube thin films on flexible substrates by spray deposition and transfer printing. *Carbon N. Y.* **61,** 72–79 (2013).

105. Webb, R. C. *et al.* Ultrathin conformal devices for precise and continuous thermal characterization of human skin. *Nat. Mater.* **12,** 938–44 (2013).

106. Tee, B. C. *et al.* Tunable Flexible Pressure Sensors using Microstructured Elastomer Geometries for Intuitive Electronics. 5427–5434 (2014). doi:10.1002/adfm.201400712

107. Pegan, J. D. *et al.* Skin-mountable stretch sensor for wearable health monitoring. *Nanoscale* **8,** 17295–17303 (2016).

108. Lee, J. *et al.* Conductive Fiber-Based Ultrasensitive Textile Pressure Sensor for Wearable Electronics. *Adv. Mater.* **27,** 2433–2439 (2015).

109. Zang, Y., Zhang, F., Di, C. & Zhu, D. Advances of flexible pressure sensors toward artificial intelligence and health care applications. *Mater. Horiz.* **2,** 140–156 (2015).

110. Chen, X. *et al.* Self-powered flexible pressure sensors with vertically well-aligned piezoelectric nanowire arrays for monitoring vital signs. *J. Mater. Chem. C* **3,** 11806–11814 (2015).

111. Wang, Z. *et al.* High Sensitivity, Wearable, Piezoresistive Pressure Sensors Based on Irregular Microhump Structures and Its Applications in Body Motion Sensing. *Small* 3827–3836 (2016). doi:10.1002/smll.201601419

112. Yang, T. *et al.* A wearable and highly sensitive graphene strain sensor for precise home-based pulse wave monitoring. *ACS Sensors* **2,** 967–974 (2017).

113. Kohara, K. *et al.* Radial augmentation index: A useful and easily obtainable parameter for vascular aging. *Am. J. Hypertens.* **18,** 14–17 (2005).

114. Chirinos, J. A. *et al.* Ethnic differences in arterial wave reflections and normative equations for augmentation index. *Hypertension* **57,** 1108–1116 (2011).

115. O'Rourke, M. F. & Safar, M. E. Relationship between aortic stiffening and microvascular disease in brain and kidney: Cause and logic of therapy. *Hypertension* **46,** 200–204 (2005).

116. McEniery, C. M., Cockcroft, J. R., Roman, M. J., Franklin, S. S. & Wilkinson, I. B. Central blood pressure: Current evidence and clinical importance. *Eur. Heart J.* **35,** 1719–1725 (2014).

117. Lee, K. *et al.* Rough-Surface-Enabled Capacitive Pressure Sensors with 3D Touch Capability. *Small* **13,** 1700368 (2017).

118. Tee, B. C.-K. K. *et al.* Tunable flexible pressure sensors using microstructured elastomer

geometries for intuitive electronics. *Adv. Funct. Mater.* **24,** 5427–5434 (2014).

119. Li, T. *et al.* Flexible Capacitive Tactile Sensor Based on Micropatterned Dielectric Layer. *Small* **12,** 5042–5048 (2016).

120. Chen, C.-S. *et al.* Shrinky-Dink microfluidics: 3D polystyrene chips. (2008). doi:10.1039/b719029h

121. Martin Bland, J. & Altman, D. STATISTICAL METHODS FOR ASSESSING AGREEMENT BETWEEN TWO METHODS OF CLINICAL MEASUREMENT. *Lancet* **327,** 307–310 (1986).

122. Anastasios Kollias, Styliani Lagou, Maria Elena Zeniodi, Nadia Boubouchairopoulou, G. S. S. Association of Central Versus Brachial Blood Pressure With Target-Organ Damage Systematic Review and Meta-Analysis. *Hypertension* **67,** 183–190 (2016).

123. NADEL, J. A. & WIDDICOMBE, J. G. Reflex effects of upper airway irritation on total lung resistance and blood pressure. *J. Appl. Physiol.* **17,** 861–5 (1962).

124. Grossman, E., Grossman, A., Schein, M., Zimlichman, R. & Gavish, B. Breathing-control lowers blood pressure. *J. Hum. Hypertens.* **15,** 263–269 (2001).

125. Zintzaras, E. & Kaditis, A. G. Sleep-disordered breathing and blood pressure in children: A meta-analysis. *Archives of Pediatrics and Adolescent Medicine* **161,** 172–178 (2007).

126. Barnes, V. A., Pendergrast, R. A., Harshfield, G. A. & Treiber, F. A. Impact of breathing awareness meditation on ambulatory blood pressure and sodium handling in prehypertensive African American adolescents. *Ethn. Dis.* **18,** 1–5 (2008).

127. Mukkamala, R. *et al.* Toward Ubiquitous Blood Pressure Monitoring via Pulse Transit

Time: Theory and Practice. *IEEE Trans. Biomed. Eng.* **62,** 1879–1901 (2015).

128. Poon, C. C. Y. & Zhang, Y. T. Cuff-less and Noninvasive Measurements of Arterial Blood Pressure by Pulse Transit Time. in *2005 IEEE Engineering in Medicine and Biology 27th Annual Conference* 5877–5880 (IEEE, 2005). doi:10.1109/IEMBS.2005.1615827

129. Obrist, P. A., Light, K. C., McCubbin, J. A., Hutcheson, J. S. & Hoffer, J. L. Pulse Transit Time: Relationship to Blood Pressure and Myocardial Performance. *Psychophysiology* **16,** 292–301 (1979).

130. Geddes, L. A., Voelz, M. H., Babbs, C. F., Bourland, J. D. & Tacker, W. A. Pulse Transit Time as an Indicator of Arterial Blood Pressure. *Psychophysiology* **18,** 71–74 (1981).

131. van Ravenswaaij-Arts, C. M. A., Kollee, L. A. A., Hopman, J. C. W., Stoelinga, G. B. A. & Geijn, H. P. van. Heart Rate Variability. *Ann. Intern. Med.* **118,** 436 (1993).

132. Acharya, U. R., Joseph, K. P., Kannathal, N., Min, L. C. & Suri, J. S. in *Advances in Cardiac Signal Processing* 121–165 (Springer Berlin Heidelberg, 2007). doi:10.1007/978-3-540-36675-1_5

133. Malik, M. & Camm, A. J. Heart rate variability. *Clin. Cardiol.* **13,** 570–576 (1990).